INTERFACIAL INTERACTIONS BETWEEN IMPLANT ELECTRODE AND

BIOLOGICAL ENVIRONMENT

A Dissertation

by

CHENG-WEI CHIU

Submitted to the Office of Graduate Studies of
Texas A&M University
in partial fulfillment of the requirements for the degree of

DOCTOR OF PHILOSOPHY

Approved by:

Chair of Committee,	Hong Liang
Committee Members,	Mark Harlow
	Aaron Ames
	Won-jong Kim
Head of Department,	Jerry Caton

December 2012

Major Subject: Mechanical Engineering

ABSTRACT

Electrodes implanted into neural systems are known to degrade due to encapsulation by surrounding tissues. The mechanisms of electrode-tissue interactions and prediction of the behavior of electrode are yet to be achieved.

This research will aim at establishing the fundamental knowledge of interfacial interactions between the host biological environment and an implanted electrode. We will identify the dynamic mechanisms of such interfacial interactions. Quantitative analysis of the electrical properties of interface will be conducted using Electrochemical Impedance Spectroscopy (EIS). Results will be used to develop a general model to interpret electrical circuitry of the interface. This is expected to expand our understanding in the effects of interfacial interactions to the charge transport.

The interfacial interactions of an implanted electrode with neural system will be studied in two types of electrodes: silver and graphene coated. The interfacial impedance of both samples will be studied using EIS. The development of the cellular interaction will be investigated using histological procedure. X-ray photoemission spectroscopy (XPS) will be employed to study the chemical effects on the silver electrodes. Atomic force microscopy and Raman spectroscopy will be used for material characterization of graphene-coated electrodes.

In the study of silver electrode, two mechanisms affecting the interfacial impedance are proposed. First is the formation of silver oxide. The other is the immuno-response of tissue encapsulation. Histological results suggest that higher cell density

cause higher impedance magnitude at the interface. It is also found that the cellular encapsulation dominates the increase in impedance for longer implanted time.

In the study of graphene-coated electrode, it is found that the graphene can strongly prevent the metal substrate from being oxidized. It not only provides good electrical conductivity for signal transport, but also reduces the speed of the accumulation of tissue around the electrode. Such characteristics of graphene have great potential in the application of neural implant.

Finally, the dynamic mechanisms of biological interaction are proposed. A model is also developed to represent the general circuitry of the interface between an implanted electrode and the neural system. The model has three major components, which are interfacial double layer, cellular encapsulation, and the substrate. The model presented in this study can compensate for selection and prediction of materials and their behaviors.

DEDICATION

To my wife and my son for supporting my dream. To my parents for making me
persistent. To my advisor for making me creative. To all those friends I have met along
the way for making me proud

ACKNOWLEDGEMENTS

TABLE OF CONTENTS

LIST OF FIGURES

Page

ix

xi

LIST OF TABLES

CHAPTER I

INTRODUCTION

This chapter provides information necessary to understand the thesis research as well as background and state-of-the-art biosensor. It includes the description of sensing mechanisms , materials and the causes of sensor failure. The capabilities of biosensor for bio-environmental monitoring have enormous influences on medical, pharmaceutical, biodefense, and environmental application. Among all different biosensors, neural implant is used for measuring the electrical signal of neural cells. The investigation of interaction between bio-environment and the neural implant determines the design, function, and application for chronic neural implants.

Biosensors

In order to provide the reader with basic concepts and the functional mechanisms of biosensors, thorough review of biosensor is addressed in this chapter. A biosensor is a device for transforming biological signals into analytical ones. It is a combination of a bio-component with a physical element mainly used for converting the complex biologically derived message to quantitative information. A biosensing device has a wide range of application in the fields of medicine and environment, as well as drug development and biomolecular interactions. The representation of a biosensor consists of three major components: a sensitive bio-element, a detecting element, and a signal processing element. The bio-element can be enzymes, living cells, or microorganisms, etc.[1-3]. which recognize the target analyte. The detecting element can be used to

monitor the variation of electric current and potential [4-7], impedance [8-11], optical

intensity [12-15], electromagnetic radiation [16, 17], among others. The bio-element

directly interfaces to a signal transducer (detecting element), which together relate the

variation of the analyte to a measurable response. Different constitutions ofa bio-element

coupled to a detecting element lead to a variety of applications. Figure 1 is the schematic

diagram which represents the concept of a biosensor.
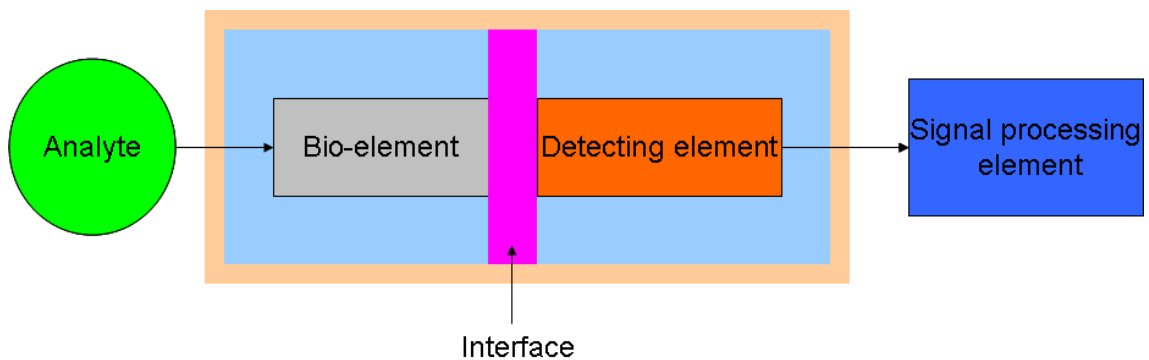
Figure 1. Schematic representation of basic concept of biosensor.

Types of biosensors

Due to the different signal detecting mechanisms, biosensors can be categorized

into various types including resonant, photometric, thermal detection, ion-sensitive

Field-Effect Transistor (ISFETs), and electrochemical sensors. In the following sections,

types used for biosensors and the sensing mechanisms will be discussed.

Resonant biosensors

The surface acoustic wave (SAW) sensor is generally used to detect bio-relevant molecules in aqueous media. This sensing focuses on change of mass, viscosity and conductivity of the substrate surface. The prototype of a SAW sensor was established based on a strongly confined acoustic energy detected by interdigited transducers [4, 18, 19]. The characteristic of a SAW sensor generally has one piezoelectric material positioned in between two transducers. An input transducer electrically excites acoustic waves of the piezoelectric material, in which the acoustic wave is received at the output transducer. The wave energy radiates into the aqueous bulk due to the perpendicular displacement of the wave propagation in aqueous environment. This causes high immense attenuation of the received signal, which hinders the application transferred into a biosensor [4, 20, 21]. The shear-horizontal (SH) surface wave, generally referred to as a Love wave, is generated using a deposited elastic layer to guide the direction of the acoustic resonance. The elastic material significantly reduces the spreading loss of acoustic energy [22-24]. Now the operation of a SAW-based biosensor is driven by the coupled wave transducer and antibody on a piezoelectric substrate. The antibody used as a bio-element is immobilized on the device that catches analyte from the aqueous medium. The bonded analytes will change the velocity of the SAW, which alters the output signal generated by the integrated electronics. The variation of the output signal can be used to evaluate the concentration of the analytes. The schematic setup of SAW-based biosensor is presented in fig. 2 [25].

3
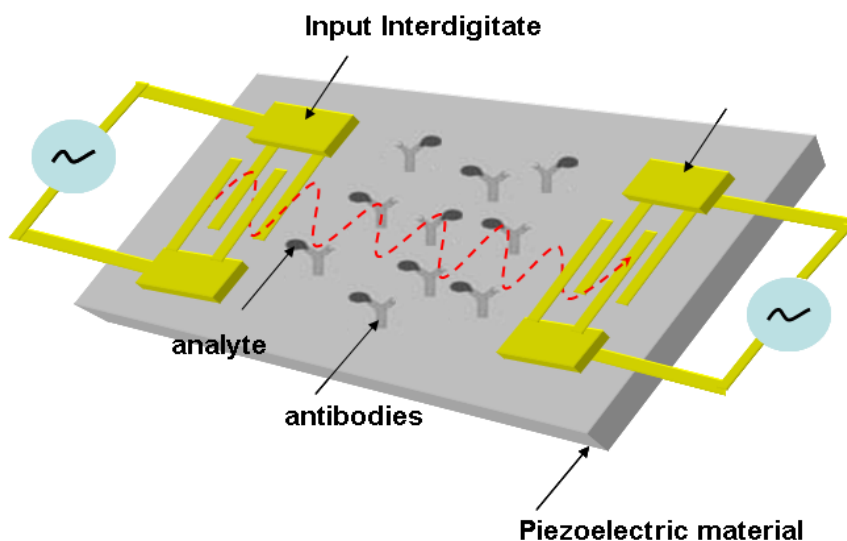
Figure 2. Schematic representation of SAW-based biosensor [25]. The arrows represent the flow of aqueous medium. (1) The aqueous environment where the sensor is immersed in solution (2) Piezoelectric material. (3) Interdigital transducer. (4) The surface acoustic wave. (5) Immobilized antibodies. (6) The analyte molecules. (7) The driving electronics. (8)The output signal generated by the operation of biosensor as the analyte binds to the sensor.

Thermal detection biosensors

Surprisingly, even with the poor reputation of weak sensitivity and non-specific heating effects, the application of thermal biosensor is still increasing. A thermal biosensor is a promising analytical tool due to the following advantages:

   - No chemical contact between transducer and sample, increasing its long-term

      stability.

   - Economical bulk products and quick response.

   - Measurements are not interfered by sample characteristics.

Novel thermal biosensors based on enzymatic conversion have been developed for monitoring the enzyme reactions. It is mainly because that the exothermic character is

involved with most of the biochemical reactions. The principle of thermal biosensor

measurement is based on the first law of thermodynamics.

$$Q = -n_p \Sigma \Delta H \tag{1}$$

$$Q = Cp \, \Delta T \tag{2}$$

where Q is the total energy of heat, H is the enthalpy, and Cp is the heat capacity. The

measureable local temperature shift (ΔT) generated by the heat production is dependent

on the heat capacity of the system [26].

$$\Delta T = -\Delta H n_p / Cp \tag{3}$$

Generally, the Cp of most organic media is much lower than that of aqueous solvent [27],

The sensitivities and detection limit of the sensor are determined by the organic solvents.

Figure 3 is the schematic diagram of the principle set-up for an enzyme thermistor (ET).

The thermostated box controls the physiological temperature. Samples and the buffer are

injected to the ET where the aluminum thermostates the buffer stream. The heat

generated by the enzymatic conversion reduces thermistor resistance, and the bridge

amplifier registers the signal.
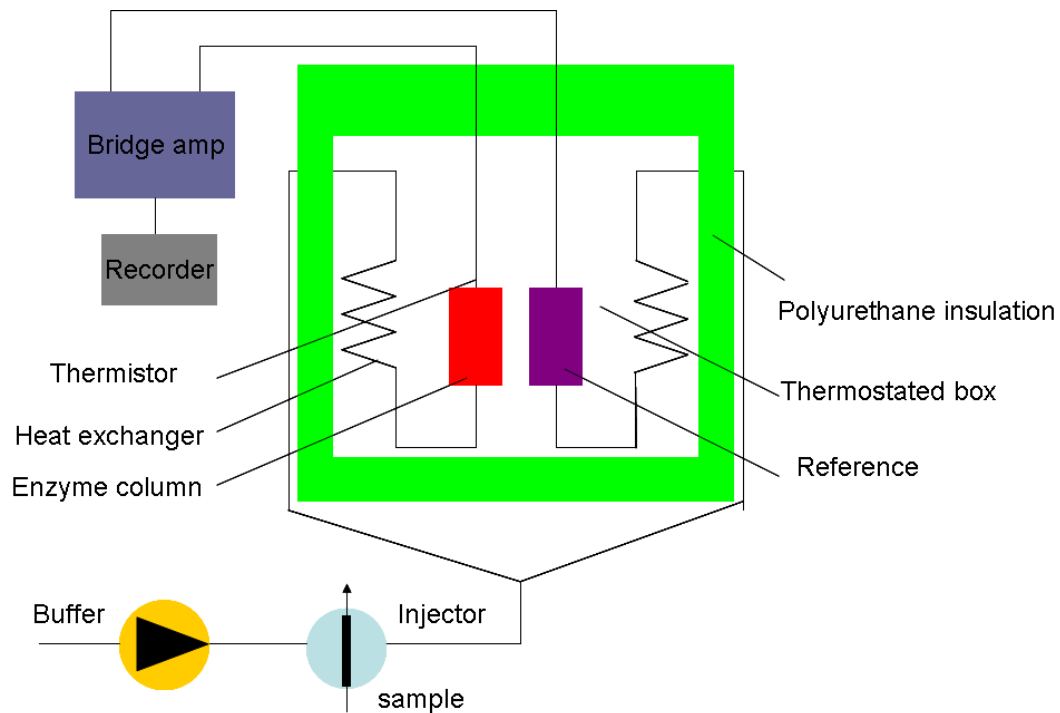
Figure 3. Schematic representation of thermal biosensor.

Photometric biosensors

In this type of biosensors, the measured output transduced signal is the light intensity. More than 75% of the research papers for optical biosensor focus on using the Surface Plasmon Resonance (SPR) [28]. The Surface Plasmon Resonance essentially is diffraction anomaly due to the surface excited plasma [29]. The electrons resonate when the wavelength of oscillating mobile electrons (plasma) matches the wave vector of incident light. The resonating plasma is associated with the electromagnetic waves propagating in a direction parallel to the interface of two media and decaying evanescently, i.e. evanescent wave. Due to the limited propagating length of the surface plasma wave (SPW), the detection of SPR sensor is conducted at which the SPW is

6

excited by the incident light source. A SPR sensor is constituted by an incident light, a transducer with a gold side contacted with the detection apparatus and the other side contacted with microfludic system (flow side), and an electronic system for processing the output signal. Fixed wavelength is shot to the gold side and be reflected, which induces an evanescent wave penetrating into the flow side. During the measurement, the analyte is introduced through the microfludic channel and bound with the sensors that change the dielectric constant of the medium. This will lead to the changes of refractive index near the surface hence affecting the refracting SPR angle (fig.4)[30-32].
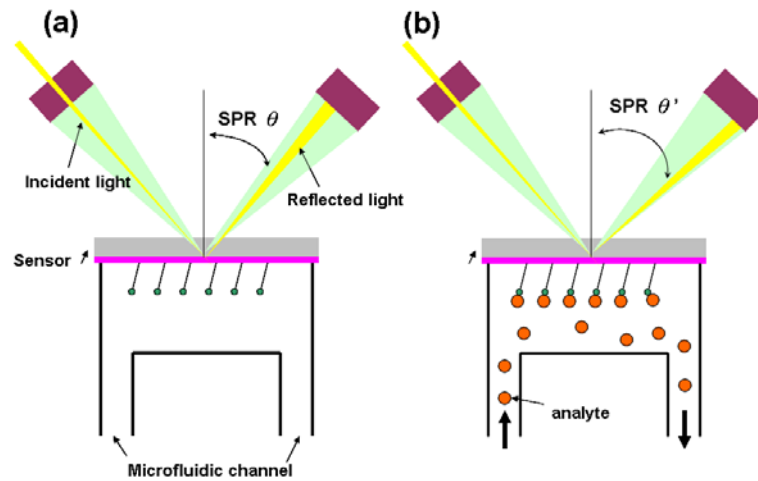
Figure 4. Schematic representation of photometric biosensor.

Ion-sensitive FETs biosensors

The development of ion-sensitive field effect transistors (ISFETs) started in the 1970s, usually used for PH and ion concentration measurement [33-35]. To integrate the sensing circuit, most of the ISFETs were produced majorly through MEMs fabrication based on silicon substrate. This also makes ISFETs as a perfect transducing element for

7

biosensing. The reactive silanol (SiOH) groups on the SiO_2 surface provide a stem for covalent attachment of bio-molecules by using H^+ and OH^+ as binding site.

SiOH ----------- SiO^- + H^+

SiOH +H^+---------$SiOH^{2+}$
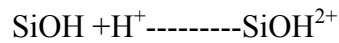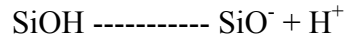
Through silicon surface modification, the bio- analytes can be successfully immobilized onto the gate surface [36-40]. Figure.5 outlines the schematic configuration of the ISFETs.
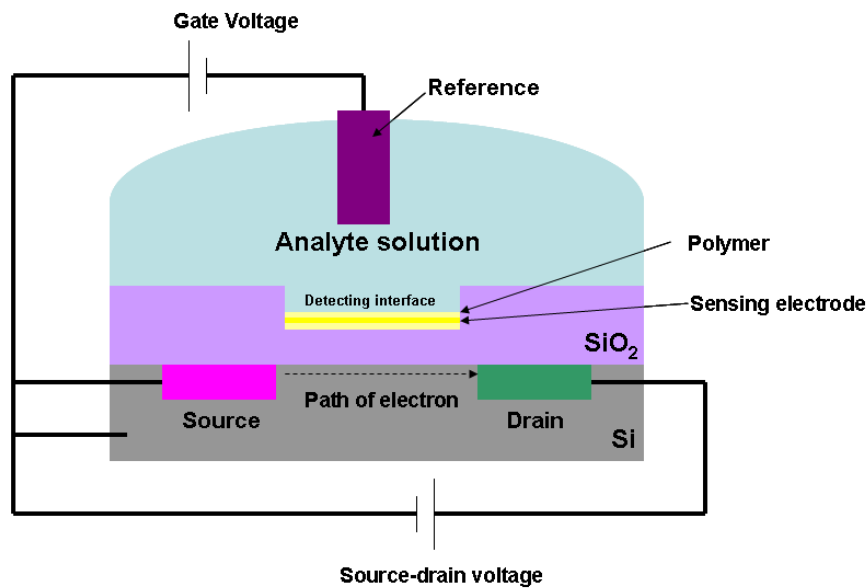
Figure 5. Schematic configuration of ISFETs biosensor.

ISFET consists of sensing electrode coated with a polymer selectively permeable to analyte ions, and a field effect transistor structure. The current flow in the gate voltage is regulated by the potential difference between source and drain. When the analyte ions diffuse through the ion-sensitive polymer, the charged biomolecules cause the depletion or accumulation of charge carriers. This will lead to the potential difference at the

8

detecting interface. This interfacial potential difference is regulated by the ions concentration in the solution; therefore, the change of the current in the transistor is a measure of analyte concentration.

Electrochemical biosensors

The constitutional concept of electrochemical biosensor is based on a matrix bound bioactive material coupled with an electrochemical transducer. Essentially, it's a surface modified electrical conductor for different electrochemical functions. This type of sensors targets those biological reactions which derive ions production and consumption. This will cause the charge transfer across the double layer of the physico-chemical transducer which generates the measureable signal [41-43]. Based on the measured signal characterizations, the electrochemical biosensor has three main classification of silicon based chip. Figure 6 is the illustration of electrochemical biosensor.
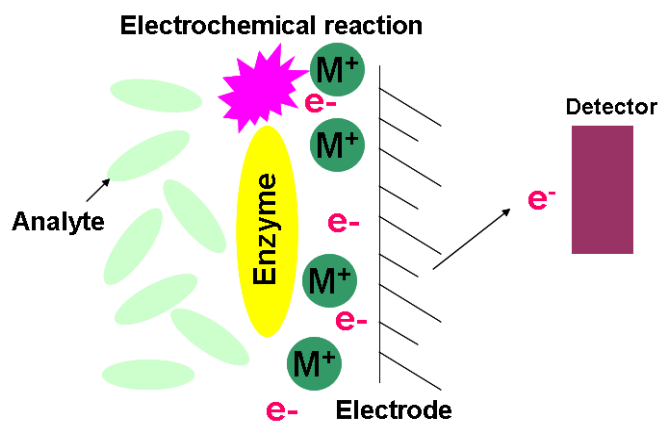
Figure 6. Schematic configuration of Electrochemical biosensor.

1. Potentiometric

   The principle of potentiometric biosensor is based on Ion-Sensitive Field-effect Transister, in which the output signal is oxidation/reduction potential. The electrochemical reaction generated ions is accumulated at the ion-sensitive membrane of ISFET interface. When this potential is applied to the electrode, it modulates the current flow through the FET leading to a measurable potential of the detector.

2. Amperometric:

   The high sensitivity of amperometric sensor provides the sensing ability to detect electroactive substance in biological samples. By applying a constant potential between the sensing and auxiliary electrode, the conversion of electroactive species take places at the electrode. This will result in electrons transfer, and the current is directly correlated to the bulk concentration of tested electroctive species [41, 42].

3. Impedimetric:

The chemical reaction resulting in either ion production or consumption will change the conductivity of the solution. The measure of solution's impedance (Z) change is introduced for this type of sensor. The sensitivity of impedimetricis relatively low since the measure of conductance is essentially non-specific. This drawback can be overcome by targeting the specific defined geometry of enzymatic reaction on a microelectronic cell [41].

The type of biosensors, sensing mechanisms, and the applications are summarized in the table 1 to help the reader have clear view of the biosensor.

Table 1. Summary of biosensors.

Type	Sensing mechanism	Transducer	Measured property	Ref
Resonant	The change of the viscosity, mass leads to the change of resonant frequency of the acoustic wave	Mass sensitive	Resonant frequency	[18]-[25]
Thermal detection	Bio-reaction results in exothermic character	Thermal	Heat of reaction or adsoprtion	[27]
Photometric	The change of refractive index of the solution lead to the change of refractive angle of the incident light	Optical	Surface Plasmon resonance angle	[29-32]
Ion-sensitive FETs	The ionic analyte diffuses into the membrane hence change the potential difference at the detecting interface	Ion-selective membrane	Surface potential	[33-40]
Electrochemical	Bio-reaction resulting in ions production or consumption will create the charge transfer across the double layer of the transducer.	Electrochemical	Potentiometric Amperometric Impedimetric	[41-43]

Materials used in biosensors

Materials for biosensors need to be able to detect small variation of biomolecular concentration. Such materials should provide with several characteristics, which include fast signal response, and stability in bio-environment. Except for metal or metal alloys, other materials including nanomaterials, ceramics, semiconductors, etc., are also

recommended to be used in biosensor since they are usually thermodynamically stable[44]. This section will provide a brief introduction of several materials which have attracted significant attentions for their potentials for application in biosensors.

Conductive polymer

Conductive electroactive polymers (CEPs) are widely used in biosensor s due to their sensitivity, selectivity, and the ability of integration for low cost microfabrication [45, 46]. The porous structures of polymers can be used as bio-analyte immobilization matrix coupled with electronic conduit. The most common technique for conductive polymer film fabrication is electrochemical polymerization where the process is carried out in a monomer and bio-active species solution. The negatively charged bio-active species is entrapped in the polymer during the electrochemical oxidation [46]. CEPs can be used in electrochemical biosensors, ex. glucose biosensor. The enzyme, which serves as glucose oxidize, immobilized in the polymer matrix triggers the redox reaction of glucose. The electronic signals generated by the glucose oxidation/reduction can be relayed back to the detector through conductive matrix.

So-gel-derived silicate glasses

Most of the electrochemical biosensors require enzymes or other proteins to trigger the electrochemical reactions of the analytes. Effective enzyme and protein immobilization seem to be a problematic aspect for electrochemical biosensors. Common protocols of immobilization include physical entrapment, covalent binding,

surface adsorption, and cross-linking the target to the matrix. However, some of the

protocols alter the functional characteristic of the protein, which fail to preserve its

stabilities and reactivites.

Recent evidences have proven that sol-gel derived glassy silicates have several

advantages for bio-molecular immobilization [47, 48]. The structure of silicate matrix is

formed via precursors undergoing hydrolysis and polymerization reaction. This will

form a bridged SiO_2 network [48]. The porous structure of glassy silicate provides host

matrix for bio-molecular entrapment. A Silicate also provides a thermally and

chemically stable matrix. The sol-gel method does not require additional reactive agents

to bind the target to the matrix of the silicate. The biomolecules immobilized by sol-gel

method thus can preserve their native characteristics[47]. Furthermore, the spectroscopic

properties of immobilized biomolecules can also be monitored due to the transparency of

sol-gel-derived silicates [49].

Nanomaterials

The conductive nanomaterials have been attracted high attention for

electrochemical biosensor application since their structures provide high

electrochemically accessible surface area. One of the most attracting materials is the

carbon nanotubes (CNT). The single-walled carbon nanotubes can be metal or

semiconductor based on different structural assembly [50]. Through surface

modification, the carboxylate moieties of CNT can be coupled to variety of biomolecules

13

including DNA, enzymes and proteins [50-52]. As well as other characteristics, biochemically inert also makes CNT suitable for biosensor.

Different from the bulk materials, nanoparticles possess exclusive physical, chemical, and electronic properties. Those properties have found interest in biosensor applications. One of the applications is the use as catalysts since metal nanoparticles are stable and can fully recover during bio-redox [53]. Metal nanoparticles can be used as a tracer in an electrochemical DNA hybridization sensor where the nanoparticles are captured by the hybridized target (DNA) [54, 55]. Qantum dots (ZnS, CdS, PbS) tracer have also been employed in multiple DNA detections based on the different redox potentials for different particle tags [56]. Metal oxide nanomaterials including TiO2, ZnO, RuO2, IrO2 have been found to exhibit biosensing properties with proper surface modification. Due to the control difficulty of the material particles agglomeration, polymerization is the most common strategy to overcome this issue. The nanostructured composites of metal oxide embedded into the polymer matrix nowadays have been widely utilized in biosensors.

Neural implant

Through the development of the biosensors, lot of biological behaviors and interactions have been studied including blood glucose, protein interaction, DNA, cytosolic concentration and antibody-antigen interaction, etc. Neural transmission is a fundamental biological phenomenon dominating the control and communication of body. The sensora required to study such behavior is usually referred to as the neural implant.

14

The studies of neural system started with elucidating the function of individual neurons at the cellular and molecular level [57-59]. For signal interpretation, several methodologies have also been established for signal detection, modeling and processing [60, 61]. Neural Stimulators have later been implanted into organism for understanding the neural network and behavior control [62-64].

In modern culture and medical technology, it has always been a desire to use a computer to read or control minds, or to use the same to help people who have vision, hearing, or other neural related disease. Central neural system (CNS) is the commanding center which integrates and coordinates all the body activities. Through recording or manipulating the CNS signals by artificial implantations to control the body movement has been the scientific myth for neural engineering. With the highly developed interdisplinary researches involving neural technologies and the exquisite fabrication process of artificial devices, this scientific fiction gradually breaks the dark and sees through the dawn. The Military agent (DARPA) and the National Science Foundation (NSF) have been funding researches of CNS stimulation since early 2000. The goal of the brain machine interface is to develop ultimate mine control machine, which gains the control of artificial entities thousand miles away by uplinking commanding signals of brain through the internet or satellite.

Brain machine interface

The ultimate application for the neural implant development is to study the human brain. The concept of Brain machine interface is to create a communication

pathway between the human thought and external device by transforming biological signals recorded from neural tissue into electrical signal [65]. By the needs of disable people, this technology has become highly interesting for the past 20 years. Numbers of people around the world are suffered from neural malfunction. This malfunction disturbs the connection between the commanding center and the muscle neural cells [66-69]. The options for restoring function fall into three categories. Increasing the functional capabilities of the impaired pathway is the first options [70-72]. The second is to reroute the communication path which control muscles [73-75]. The final option is to create an artificial interface which allows the brain to regain the ability of controlling the non-muscular entities.

To establish the connection between the brain and the prosthesis or other devices, high efficient and stable electrode interface is required. Therefore, studying the interaction of electrode interface in biological system seems to be the key factor for the development of neutrally controlled prostheses. The ultimate applications of CNS controlled device may include RF wireless signal controller, artificial prosthesis and neurally controlled neuro-robots. The technology for integrating the biological information into external devices requires profound knowledge of neural activities and interaction of implantation to bio-system.

Neural transmission-fundamental theory

The structure of a neural cell is comprised by dendrite (cell body), axon, and synapse. The electrochemical signal is originated at the dendrite and passed along the

axon to the synapses. The basic concept of the signal transfer lies in the sodium and potassium ion channels of neuron membrane. The pump modulates the ions transport in and out of the cell in a ratio of 3 sodium and 2 potassium which create a potential difference across the membrane. When the neural cell is encountered external stimuli (chemical, electrical), the potential drop would trigger more ion channels to open until the membrane depolarize. Since the sodium channels are more sensitive to the potential change than potassium channels. During the depolarization process, the sodium ion will rush into the axon a lot faster than the potassium ion rushing out. A ~30 millivolt potential difference resulted from this sudden depolarization is usually called action potential. Figure 7 illustrates the ion exchange on the membrane and the propagation of action potential
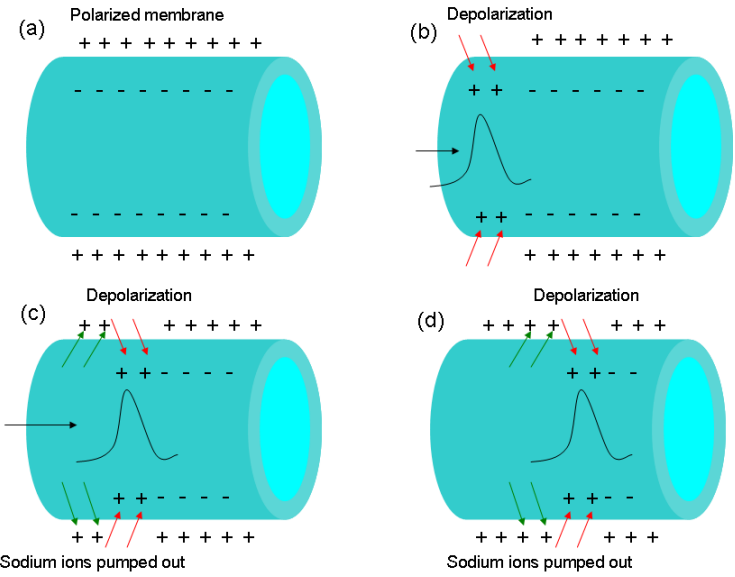
Figure 7. Illustration of ion exchange and the action potential propagation. (a) Depolarized membrane. (b) sodium ions flow in cause the depolarization generating a sudden potential difference (c), (d) Signal continuously transport through the axon.

The action potential propagates down the axon toward the synapse that causes the calcium ions rush into the presynaptic terminal. The vesicles will then fuse with the presynaptic membrane hence release the neurotransmitter in between the presynaptic and postsynaptic membrane. The information transferred by this mechanism is called neural transmission.

Implant device

Studying the electrical activity of the neural cell, i.e. action potential, is the key for decoding neural representation. A neural implant consists of single or multiple long protruding structures which has a connection between the biological neural tissue with external device or electronic system. Different from the other biosensors, it direct measures the electrical signals of neural intracellularly or extracellularly by contacting sensing element. As simple as it is, the use of bio-recognition element is not necessary for neural implant. The inserted electrodes for detecting neural signal can be classified into two categories: 1. Electrophysiological recording 2.Microelectro arrays implant.

Electrophysiological recording

Traditional electrophysiological recording can choose indirect and direct recording method to record extracellular or intracellular neural activity. The structure of this type of method consists of a metal conductor inside of a hollow tube (glass pipette) filled with electrolyte which is used to create the continuous path for ion transfer.

Positioning the tip of the pipette against the cell membrane is usually achieved by micro-manipulator. The tip of pipette is pressed against the cell membrane to capture the target cell by either applying negative pressure or electrical current [76, 77]. The cell membrane invaginates into the pipette, and the edges of the tip seal off the membrane surface (fig.8). The electrical signal will transport through the path created by the electrolyte to be detected by the conductor.
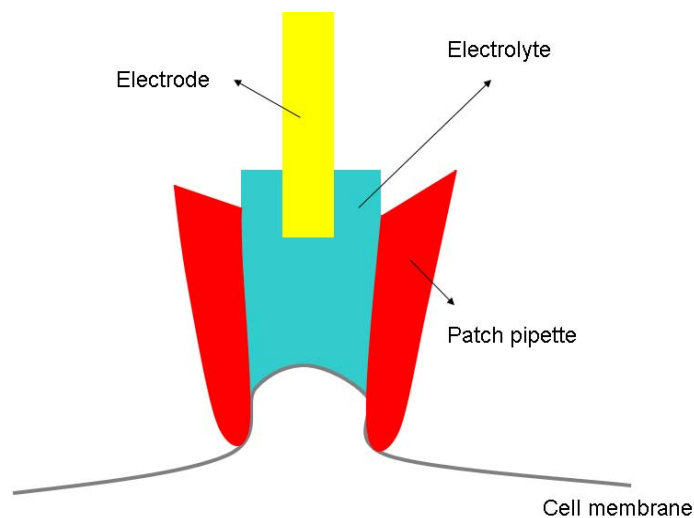
Figure 8. Illustration of ion exchange and the action potential
propagation. (a) Depolarized membrane. (b) sodium ions flow in cause
the depolarization generating a sudden potential difference (c), (d)
Signal continuously transport through the axon.

The development of drug delivery opens new horizon in studying the neural electrophysiology since the dispensed drug can suppress the tissue interaction, stimulating neural synapse [78, 79]. Drug delivery system (microfluidic channel) as well as the neural implant nowadays can be manufactured through microfabrication process.

19

The integrated hybrid device of microfluidic system and neural probe realizes this multifunctional purpose of sensing the neural activity corresponding to the effect of the drug [80-82]. For chronicle implantation, flexible parylene is introduced to the hybrid system [83, 84].

Microelectrode arrays implants

This type of implant is constructed by a penetration probe with metal coating as a conducting site. The device can either have multiple recording sites on single probe or multiple probes through different microfabrication process

Device fabrication focuses on miniaturizing the thickness of the probes to reduce damages to the tissue as well as wide shaft to hold as many recoding site as possible [85-87]. Sufficient mechanical strength is also crucial for device to survive the mechanical stress during insertion or retraction phases. Polymer has been implenented in microfabrication process to form the shaft of backbone structure of 2D, and 3D neural implant [63, 64, 88-90]. It provides the implant flexible substrate suitable for chronic neural recording (fig.9).
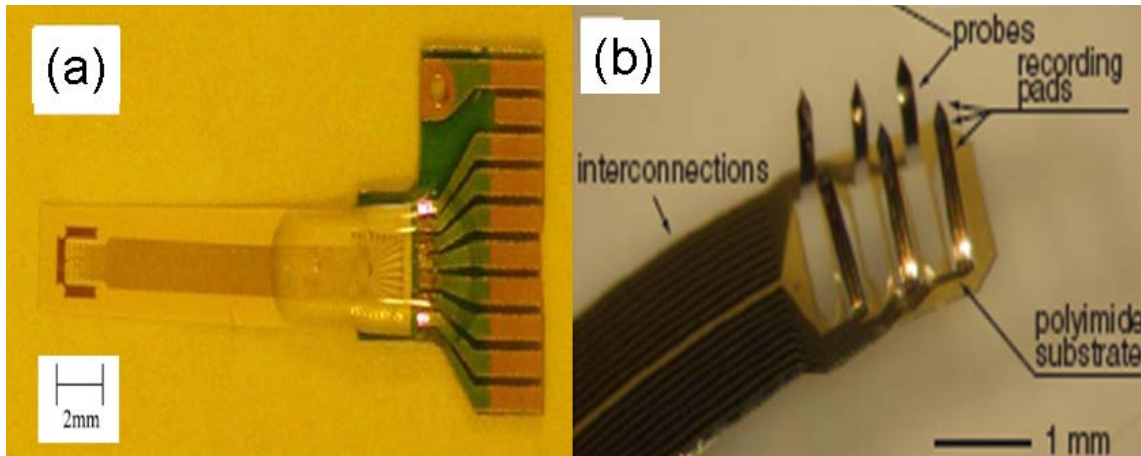
Figure 9.Polymer based flexible neural implant. (a) 2D structure
implant [63].(b)3D structure implant [90]

The emerging of 3 dimensional microelectrode array improves the instrumental

technology for studying central nervous system (CNS). The 2D neural probe can realize

the single or multiple neural recording. However, it can only obtain the information of

interest on the selected recording site. For studying the neural network of CNS, 3D

microelectrode array provides better access to the neural activities in the targeted volume

tissue [91-93]. Table 2 summarized the materials used for the structure and the sensing

pad of neural implant.

Table 2. Summary of neural implant

Type	Materials (Shaft)	Material (Pad)
Electrophysiological recording	Glass pipette [75],[76] Parylene [82], [83]	AgCl Gold Platium
Microelectrode arrays implant	Silicon [84]-[86] Benzocyclobutene (BCB) [63], [87] Liquid crystal polymer [62] Polyimide [89],[90] Metal thin film [90]	Gold Platium Tungsten Iridium oxide

Biosensor degradation and fouling

The most challenging issue in the development of in vivo monitoring of biosensor is its functional longevity. The major hurdle for chronic and therapeutic use of biosensor is the sensor degradation or fouling that causes sensor failure. Due to the direct contact of the sensor with the target fluid, the interfacial phenomenon (fouling) would cost the functional degradation of the sensor. Figure 10 is the illustration the reasons why biosensor fails.
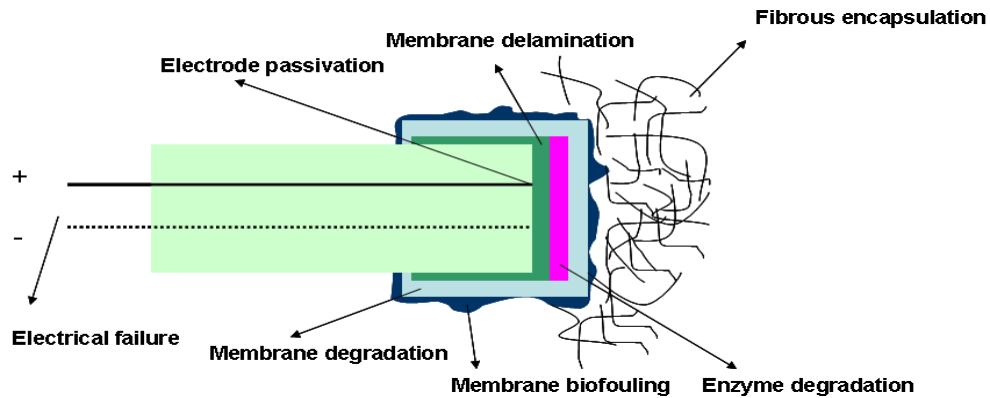
Figure 10. Illustration of a needle type glucose sensor and each of the
potential failure components [94].

Based on the cause of degradation, the functional breakdown of biosensor has
two main categories: Failures of sensor components. Failures of sensorcompatibility
(biocompatibility).

Failures of sensor components

Noise is the major problem for long term monitoring the signal in components
degradation. The electrode noise is the intrinsic noise within electrode contact interface.
Electromagnetic interference causes the electrical circuit disturbance by the emitted
radiation, hence degrading the circuit performance [95]. Electrochemical noise as well
as Flicker noise would cause the signal drifting. This usually happens while sensing low
concentration molecules by sensor without electrochemical amplify [96]. Frequently
calibration for constantly drifted electrode is not approval for real-time monitoring and
long term implantation. Other factors include electrical short circuit, lead detachment
and membrane delamination [94, 97].

Failures of sensorcompatibility

Membrane biofouling

      The cause of membrane fouling is the adhesion of protein or other substances onto the membrane interface due to the heterogeneous chemistry. This adhesion layer hinders the target analyte diffusion through the membrane [98, 99]. This adhesion phenomenon can be divided to initial, intermediate, and late event [98]. The initial event starts with a single layer of protein adsorbed to the membrane interface. Inflammatory response in the intermediate event due to the healing response followed by releasing reactive oxygen and proteolytic enzymes would decrease the pH value [100]. The encapsulation layer is formed around the sensor in the late events because of the tissue repairing and healing. Figure 11 presents the temporal modulation of the cellularity in different stages of the wound healing.
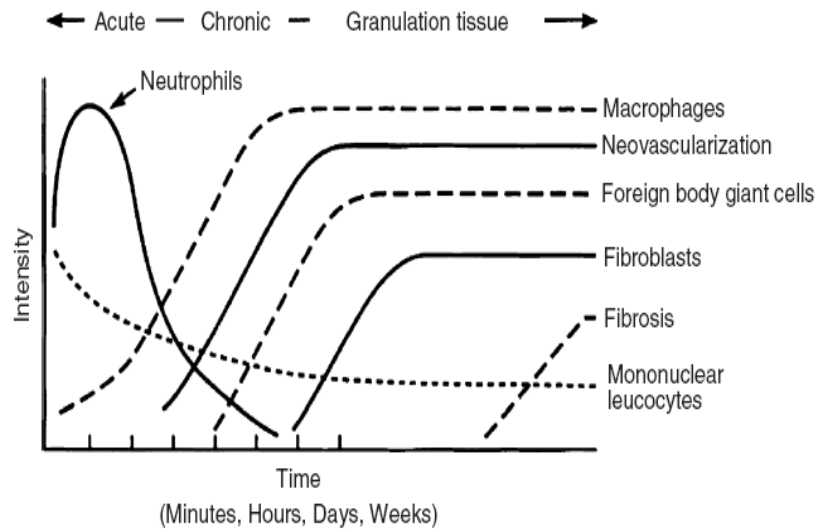
Figure 11. Temporal modulation of the cellular response in different
states healing response [101].

In the glucose sensor, this encapsulation is considered as a diffusion barrier
which reduces the sensor sensitivity or even impairs its functional [102, 103]. Reducing
the membrane fouling lately can be achieved by tailoring the biocompatibility including
membrane modification, biocompatible coating material, Local drug delivery, and
flowing fluid system.

Enzyme and membrane degradation

Most of the biosensor design consists of enzyme as biorecognition and
membrane structure for permeability control, especially in glucose biosensor.
Theoretically, enzyme is only used for catalyzing rather than being consumed in the
reaction. Practically, immobilized enzymes in the biosensor will gradually loss the
activity due to the denaturization and leach out through the outer membrane. Study has

found out the denaturing of glucose oxidase enzyme in the glucose biosensor [104]. Increasing or maintaining the enzyme loaded inside the sensing element therefore determines the longevity of the glucose biosensor. However, increasing the enzyme layer using chemical cross-linking agent not only delay the sensor response, but also lead to the crack of outer membrane [105]. Novel design of dual enzyme or [106-108] and Coil-type [105] electrode has proven capability for enzyme loading increase without damaging the outer membrane.

To keep the glucose sensor linearly transduce glucose concentration, outer membrane is used to restrain and control the flux of glucose. Membrane degradation has been found where the membrane integrity is damaged [109, 110]. The environmental stress and the interaction would result in the membrane cracking for longer term implantation. This membrane degradation would loss the permeability control and would cause the leakage of the immobilized enzyme. Different polymer materials or coatings have been studied for the lifetime improvement of the biosensor including.

Electrode fouling

Electrode fouling is the electrode passivation where the electrode surface interacts with the electrochemically active species or adsorbs non-electroactive substance. The substances change the electrode surface when they are able to penetrate the outer membranes and make the contact to the electrode. The electrode fouling would cause positive and negative error. In an amperometric glucose biosensor, the interaction interferes with the signal by generating unwanted current[111]. It's also found that low

26

weight molecular may impair the detecting ability of platinum electrode for sensing H_2O_2 [112]. To overcome the interference, an inner selectively permeable membrane in between the enzyme layer and the electrode is introduced into the biosensor design. This inner membrane allows the H_2O_2 to be detected but prevents the electrode from incurring interference. Till now, solvent-cast membranes, electropolymerised film, and polytetrafluoroethylene have proven effect of protecting the electrode from fouling [99, 113, 114].

Neural implant failure

To study the electrical properties of the neural system, reliable input or output signal determines the success of implementation in neural implant. Similar to the membrane biofouling, the chronic neural implant failure suffers from the biological interaction around the implant site. The interfacial interactions between implanted electrode and the host neural system have enormous influences in signal reliability. The cause of implant failure is mostly due to the interaction with the host immune system. One such response is the encapsulation of the implant [115-117]. During the insertion process, the vascular damages trigger the response to injury which leads to the development of a compact sheath around the implant (figure 12).
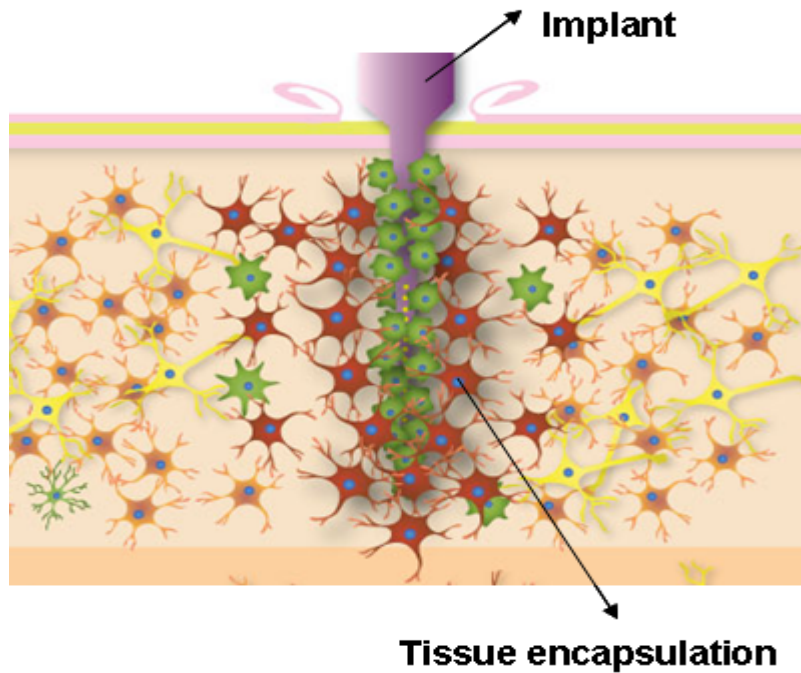
Figure 12. Illustration of tissue response to the artificial imitation[118].

This injury response involves several cells participation including glial cells and immune cells. The formation of compact sheath is believed to have different electrical properties than normal tissue [119, 120]. In addition, the encapsulation finally results in the electrode isolation from the brain. Both factors have huge impact on the chronic neural recording or stimulation. Figure 13 shows the images of immuno response around the implant site under confocal microscope.
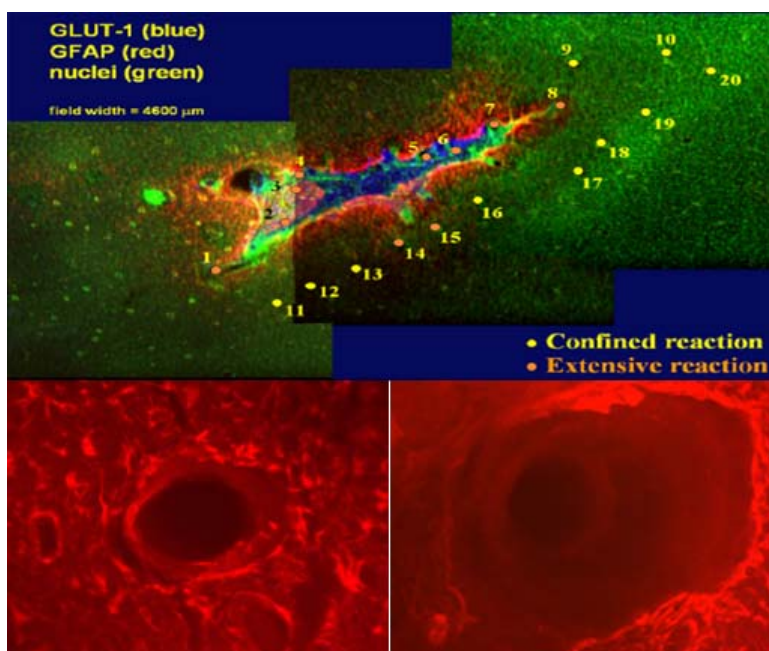
Figure 13. Immuno response around the implant site [121]. Upper confocal image shows the responding sites for 20 microelectrodes under antibiotic staining. The bottom two figures show the implantation trace after the explant with shorter implant time (left) and longer implant time (right)

This cellular event of encapsulation seems to be inevitable. Therefore, reducing the tissue response is the key for extending the life span of neural implant. Different methods have been proposed to hinder the immno reaction for neural implantation, which include electrode design optimization [122], insertion optimization [123], biocompatible enhancement by electrode surface coating [78], anti-inflammatory drug delivery [124], and electrical treatment by applying electrical current through iridium microelectrode for rejuvenation [125, 126].

Summary

A conceptual interpretation of biosensor is described. Different types of biosensors, sensing (transducing) mechanisms, and the use of material and its benefit were presented and summarized. Major problems, cause of failure, and the solution corresponding to the potential degradation components in chronic implantable biosensor application have also been described.

In this chapter, basic understanding of the bio-interaction and its effect to the sensor degradation were presented. For neural signal sensing, theories of bio-restriction and solutions have been proposed. However, the kinetic and dynamic mechanisms affecting the implant interface have not been well studied. Measurable prediction of the electrical properties of the interface is necessary for future design of brain machine interface.

CHAPTER II

MOTIVATION AND OBJECTIVES

As mentioned in previous chapter, extensive efforts have been made in understanding the tissue encapsulation of the neural implants. The distinguishable cellular events have been discovered. However, lack of knowledge regarding the change of the electrical properties on the interface still hinders the application of a neural probe. In addition, there is no sufficient information of kinetic and dynamic interaction affecting the electrical properties of the electrode interface.

Objectives

This research has the following four objects

1. Develop a methodology that can effectively analyze the interfacial interactions.

2. Being able to quantitatively characterize of the changes in electrical properties of an electrode.

3. Being able to predict the behavior of an electrode in various biological environments.

4. Being able to identify new materials to improve the lifespan of an implanting electrode.

Approaches

1. For establishing fundamental knowledge, the abundance and accessibility of an American cockroach makes it the perfect candidate for this study.

2. Silver is chosen as the material for implant electrodes in this study since it provides good electrical conductivity. It is relatively chemically active that not only reduces the monitoring time but also provides information of potential chemical reaction due to the interaction.

3. Graphene-coated electrodes will be used as implant. The effect of such material to the interfacial interactions between the electrode and the neural system will be analyzed.

4. Electrochemical Impedance spectroscopy is used for monitoring the electrical behavior while implanted.

5. A general model will be established to predict the effect of interfacial interactions.

These objectives listed above will be accomplished by studying the electrode interface implanted in American cockroach by using EIS analysis. Electrochemical characterization of electrode/bio-system interface will be performed on an implanted silver electrode. Through the EIS analysis, the interfacial impedance variation will be monitored which shall give an analytical and predictable electrical behavior.

Outcomes

      The analysis will establish relationships between impedance and the electrode/bio system. We will propose a model for determining the components participating in affecting the electrical properties. Through the equilibrium circuit model, contribution of each interfacial component will be delineated in quantitative manner. Kinetic and dynamic process of the interaction will be confirmed, that can incorporate for tailoring future circuitry design of neural implant.

Dissertation structure

      This dissertation presents the phenomenon of electrode-bio interaction of implantable biosensor and its effect to the sensor failure in chapter I. The motivation and the objective were presented in Chapter II. Electrochemical evaluation method and the spectral analysis conducted to study the interfacial interaction will be presented in chapter III. Results and discussions of bio/electrode interfacial interaction will be discussed in chapter IV, V. The models used to represent the interface will be discussed in VI followed by conclusions and future work in chapter VII.

CHAPTER III

MATERIALS AND METHODS*

This chapter introduces materials and procedures utilized in current research. It discusses information of sample preparation procedure, evaluation methods (EIS) and characterization techniques (XPS, Raman). This research focuses on investigating the interaction between implanted metal materials to the host biological environment. The interaction focuses on silver and graphene-coated-silver electrode interface. Description for sample preparation will be addressed in two parts; silver electrode and graphene-coated-silver electrode. The theories of the evaluation (EIS), and characterization methods (XPS, Raman Spectroscopy) will be briefly introduced in later sections.

Neural implantation preparation

As discussed in motivation and objective chapter, the establishment of fundamental knowledge of the electrode/bio interface necessitates further statistic analysis. The American cockroaches (*Periplaneta Americana*) live as adult for about one year. They are one of the few insects that can be commonly found throughout the world's populated regions. They are easy to rear and to handle. Therefore, this insect was chosen as the implanted object in this study. In this section, the insect and electrode

---

* Part of this chapter is reprinted with permission from "Electrode-immune system interface monitor through neural stimulation in American cockroach (*Periplaneta americana*) by Cheng-Wei Chiu, Jorge M. Gonzalez, Mark Harlow, S. Bradleigh Vinson, Hong Liang, Electrochimica Acta, 68, 81-87, Copyright (2012) by Elsevier.

preparation will be discussed in the first two subsections. The surgical procedure and Electroscopy impedance protocol will also be described in the last two subsections.

Insect preparation

In this experiment, laboratory reared adult American cockroach (*Periplaneta Americana*) were used. Colonies were fed and kept in plastic containers provided with water and food (Puppy Chow, Inc). Approximately 50 roaches with mixed gender and ages were kept in each box maintaining sufficient space to prevent from the healthy population from overcrowding. The containers were filled with wood chips to filter excrement and control the humidity. Room temperature was kept at 80°F with ~75% relative humidity level, and alternating light-dark cycle for 12 hours each. The controlled environment provides ideal living condition and duplicates diurnal habits of the insect. In addition, to maintain the healthy condition of insect, dead insects were removed immediately in daily checkup to keep the potential diseases from spreading to the population.

Electrode preparation

The electrodes preparation was divided into two part; silver electrode and grapheme coated electrode.

Silver electrode preparation

With good electrical conductivity and relatively high chemical activity, the silver is chosen as the implanted material in this study. In addition, silver is not toxic to the

biological environment compared with copper. Table 3 summarized some electronic
properties of silver and copper.

Table 3. Summary of Ag, and Copper

Material	Electron configuration	Electronegativity	Electrical resistivity
Silver	$4d^{10}\ 5s^1$	1.93 (Pauling scale)	15.87 nΩm (20 °C)
Copper	$3d^{10}4s^1$	1.90 (Pauling scale)	16.78 nΩm (20 °C)

.Regular magnetic copper wires (Ø 100 μ m) were used as the substrate for silver
deposition. Copper wires of two centimeters long were used in which the insulation layer
of the tip was trimmed off to expose 1mm bear metal. Silver electrode is prepared using
the electroplating setup (fig. 14) on the magnetic copper wire substrate (Ø 150μm).
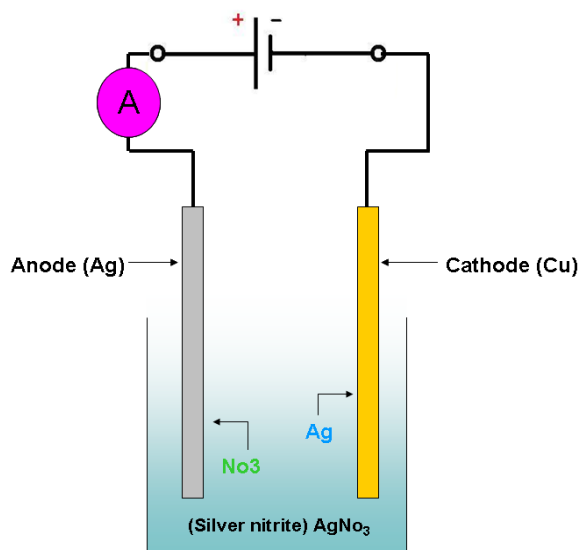
Figure 14. Illustration of silver electroplating galvanic cell. Silver rod is
used as anode and the copper wire is used as cathode. 1 wt% of silver
nitrate ($AgNO_3$) is dissolved in the DI water.

Silver electrodeposition was performed analogous to a galvanic cell acting in reverse. The oxidation reaction at the anode allows silver ions dissolve into the silver nitrate solution. Silver ions then transfer to the cathode forming the silver coating. Figure 15 is the SEM images of as received silver coating. The typical dendrite structure of silver is obtained. Close-paired silver electrode will be used for later implantation for electrical stimulation purpose. One of the wires will be connected to the V^+ while the other connected to the ground (V^0).
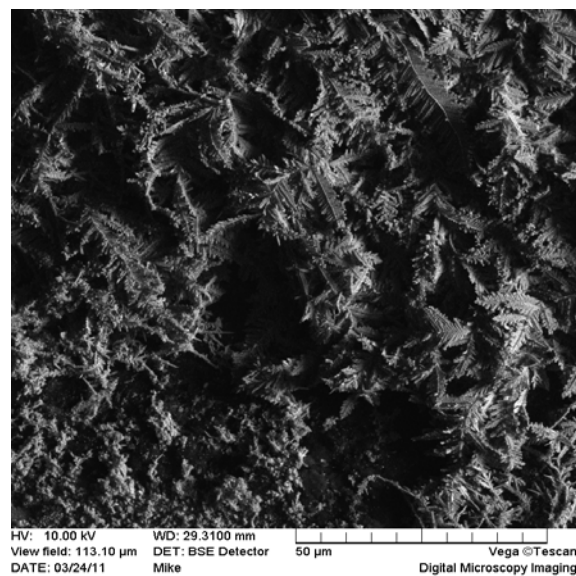
Figure 15. SEM images of silver coating through electrodeposition process. Silver dendrite structure is observed in the image.

Preparation of graphene-coated electrode

Graphene, the thinnest material ever discovered in the world, is an allotrope of carbon [127]. The lattice structure of graphene is bonded by the sp^2 carbon atoms which

form a 2 dimensional plane. Several proven characteristics of graphene make this material potentially applicable in many research areas. The material properties of graphene include high electron mobility, quantum hall effect in magnetic fields, thermal conductivity, and strong mechanical properties. Since graphene is carbon based material, this potential biocompatible material has also been studied related to bioelectronic applications. Due to the wide electrochemical potential exhibition [128], graphene or its composite has been used in biosensors[129-131]. In the study, we attempt to apply graphene coating to the neural implant to explore the capability of the same for reducing the bio-interaction as the result of tissue encapsulation.

In 2004, the research team in University of Manchester firstly developed mechanical exfoliation method to obtain graphene [132]. In the current study, the same approach was used to acquire pristine graphene layer by repeatedly peeling the graphite on the scotch-tape. The graphene will be later transferred on to the polished silicon substrate (fig.16).
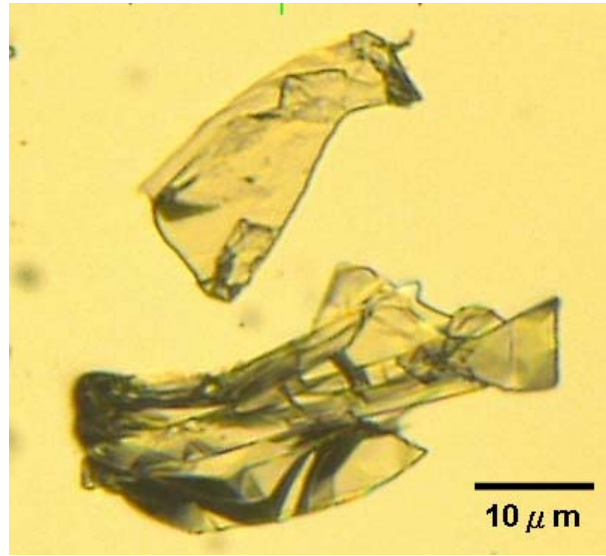
Figure 16. Single and multiple graphene layers on silicon substrate by
exfoliation method.

For graphene coated silver electrode preparation, 30 Gauge (Ø 300 μ m)
acupuncture needle (stainless steel) with 4 centimeter long was used as substrate. High
purity silver paint (SPI-paint UN#1123) was applied on the acupuncture needles, which
provides adhesive properties for further transfer of graphene layers. The silver-coated
electrode was mounted onto a micro-manipulator for position adjustment. The transfer
process was operated under optical microscope. By slight tapping the tip of the silver
coated electrode against the silicon substrate, the grapheh layer(s) can be transferred
onto the silver surface. The graphene-coated silver electrode is placed in a Petri-dish for
7 days prior to the implantation and the EIS analysis. This empirical step is to make sure
that applied silver paste completely dries out and provides more reliable impedance
result.

Neural anatomy of American cockroach

The central nervous system (CNS) of the cockroach is morphologically and physiologically complicated due to its capacity to fulfill separate functions. The CNS is responsible for receiving internal and external signal, signals integration, and deriving responsive adaption [133]. In surviving to various environmental cues, the reaction of cockroach's nervous system is pervasive. Generally, the CNS of American cockroach is symmetrical. The neural bundle in the central nervous system referred as ganglion, which is connected by bilateral interneuron connectives throughout the body. Among total 11 paired-ganglia (including the head), three of them locate in the thorax and the rest six are in the abdomen. The brief schematic diagram of CNS anatomical features is shown in the figure 17b.
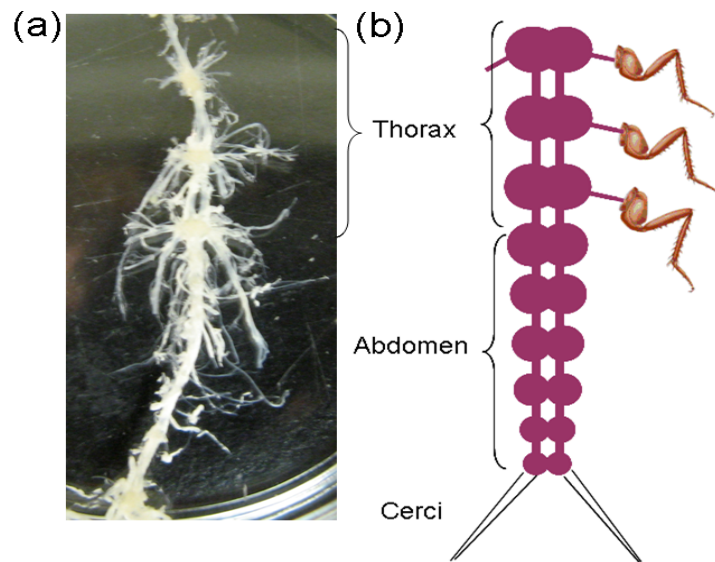
Figure 17. Nine paired of ganglion reside across the cockroach's body.
(a) Dissected CNS of American cockroach. Three thoracic ganglia are directly connected to the legs which are bigger than the abdominal ganglion. (b) The illustration of CNS in American cockroach.

The cerci are the protruding structures coming out of the end of abdomen (fig.18). Hair sensilla on the surface of cerci function as receptor which responsible for sensing the air perturbation. This sensory organ is mainly responsible for the evasion behavior of cockroach to the predator. It was reported that the cercal stimulation leads to the ascending electrical impulses to the thoracic ganglia [134]. Evidences also support that the tactile and wing stimulus of receptor can triggered oriented escape motor output generated by the thoracic ganglia [135, 136]. Differently from the human, the escape initiation of American cockroach doesn't necessarily require commanding signals from the supraesophageal ganglion (brain). The thoracic ganglia integrate the ascending information and coordinate motor neuron to produce the locomotive behavior. Hence the study will focus on the interaction between the implant electrode and the thoracic ganglia.

Figure 18. Cerci of American cockroach

Surgical preparation

The position of the thoracic ganglia locates in the abdominal area of the thorax.

The area is covered with the protective exocuticle (fig.19).
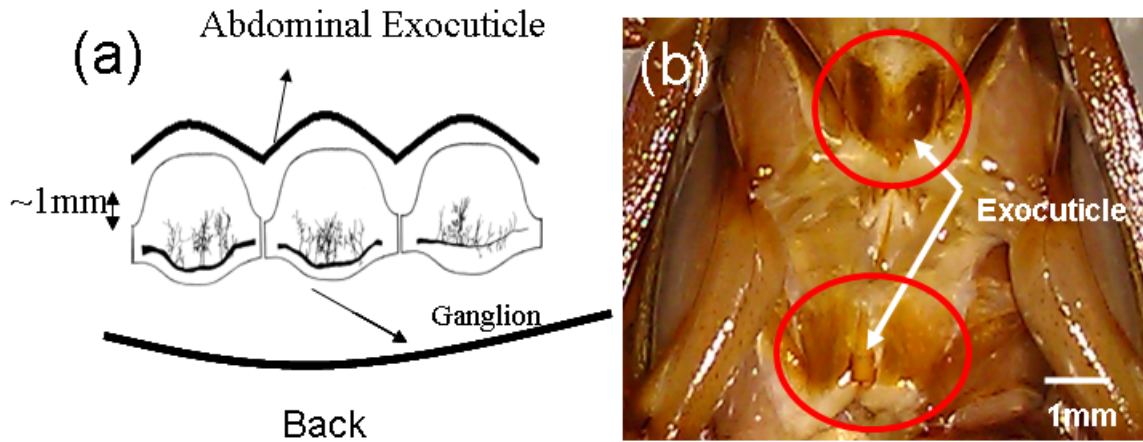
Figure 19. American Cockroach abdominal area. (a) Illustration of the
location of ganglia which locates around 1mm beneath the abdominal
exocuticle. (b) OM images of abdominal area.

Prior to the implantation, the American cockroach (*Periplaneta Americana*) was
anesthetized using carbon dioxide. Six legs and the pronotum were pinned to a Petri-dish
filled with wax in order to reveal the abdominal area. The ventral thoracic exouticle was
gently removed by the scissor to expose the ganglia. The tip of the electrode with
approximately 1mm long will then penetrate the membrane to reach the neural bundle of
ganglia. The process of insertion is controlled using micro-manipulator. The images of
exposed ganglion after the surgery and the ganglion with implanted electrodes are
presented in figure 20.
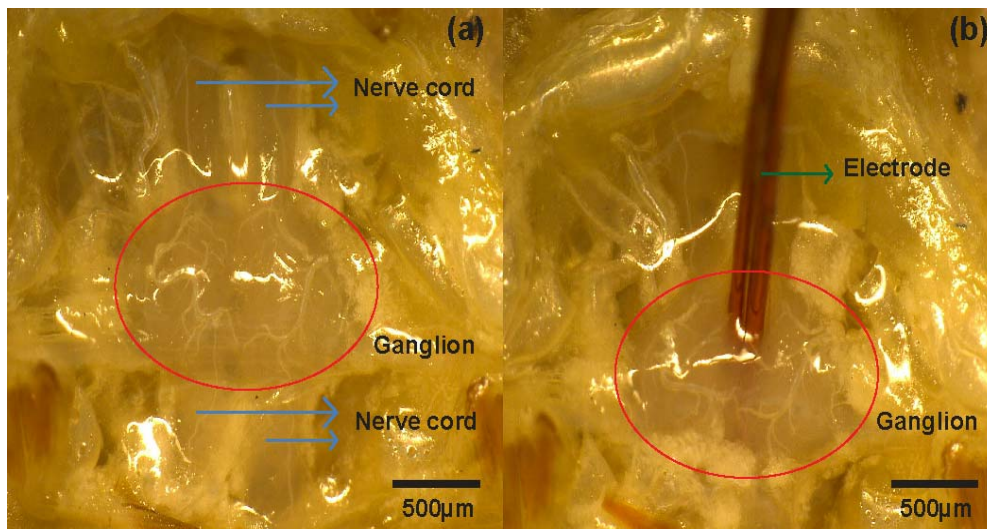
Figure 20. The optical image of ganglion after the sample preparation.
(20a) The exposed ganglion before the implantation. The circle
indicates the location of the ganglion which is connected with pair of
ascending and descending nerve cord. (20b) The exposed ganglion after
implanted with the close-paired electrode.

American cockroaches (as all the insects) are poikilotherm, which can survive a long period of time if they do not completely lose their hemolymph. The surgical wound done to the subject was minimal, which do not allow hemolymph to loose. All the tested subjects were alive and retuned to the rearing cultures. They behaved normal as the ones that have not been tested yet. The hemolymph of cockroach contains different type of ionic contents, majorly Na^+ and Cl^-. The ionic concentration of Na^+ in the hemolymph of adult cockroach falls in the range from 132~185 mM/kg [137-139]. Table 4 presents a list of ionic concentration of American cockroach hemolymph from different study [133]. To prevent the internal system of cockroach from dehydration since the thoracic ganglion was exposed in the air, 1 μl saline solution was applied to the surgical wound

43

during the stimulation process every 30 mins. The saline solution used in this study is

~0.9 wt% NaCl which is equivalent to 161mM/kg of Na^+.

Table 4. Ionic concentration of American cockroach (*P. Americana*).
The unit of hemolymph concentration is mM/kg

Stage	Na^+	K^+	Ca^{2+}	Mg^{2+}	Cl^-	PO_4^{3-}	reference
Nymphal	114.8	61.8	4.3	--	--	--	[140]
Adult	132	8.7	3.7	4.7	107	1.04	[138]
	185	16	--	--	--	--	[139]
	179	--	--	--	--	--	[137]
	161	--	--	5.6	--	--	[141]
Adult females	--	--	-	-	112	--	[142]

Electrical stimulation protocol

The electrical potential for the stimulation was applied via a Labview program

conncected with a USB high-performance data acquisition device (National Instrument,

USB-6229 DAQ). A rectangular wave with 2 μs pulse duration was used as the stimulus.

The input electrical potential was preset as 1V where the input frequency was preset as

1Hz. The illustration diagram of the connection for electrical stimulation is presented in

figure 21.
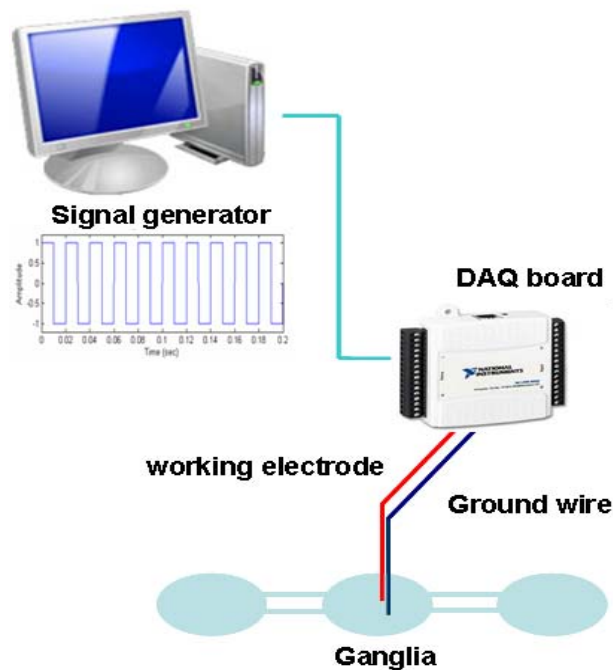
Figure 21. Illustration of electrical stimulation setup.

For silver electrodes, 24 electrodes were implanted and tested with 10 electrodes reserved for electrical control (EIS tests only without pulsing stimulation), 2 reserved for material characteristic study and 2 reserved for histological analysis. The process was monitored from 10 minutes to 48 hours in order to investigate the change of electrode-bio system interface versus time. For graphene coated silver electrode, there's no electrical stimulation participating during the implantation. The 10 implanted electrodes were analyzed for each implanted time. The process was monitored from 1hour to 48 hours. Table 5 summarized the parameters of implantation performed in this study.

Table 5. Implantation condition

Materials	Electrical stimulation	Implantation time
Silver electrode	1V, 1Hz	10min, 1hr, 4hr, 16hr, 24hr, 36hr, 48hr
Silver electrode	N/A	
Graphene coated electrode	N/A	1hr, 6hr, 12hr, 24hr,48hr

Electrochemical impedance spectroscopy

Background

Electrochemical Impedance Spectroscopy (EIS) is an evaluation method used for characterization of material interface. The high sensitivity of the double layer capacitance variation of EIS makes it a powerful tool to analysis the complex interfaces of an electrode [143]. The concept of Impedance is similar to the resistance. It's a measure of how much the circuit or material impedes the flow of current. The EIS measures the response of a system to a periodic and oscillating signal with small amplitude at given frequencies. During the measurement, the system sends a small amount of sinusoidal potential to the target in order to obtain pseudo-linear response of the cell. The target material impedes the input signal in a response to phase, capacitance, resistance changes to the given frequencies based on material electrical property.

Impedance (Z) can be mathematically expressed in following notation (eq.4). It has the real and imaginary part which represents the system resistance, and reactance, respectively. The effects of imaginary components of the impedance vary with the current frequency. This is the reason why Impedance measurement is complicated.

$$Z\,(j\omega) = R + jX = R + \frac{1}{j\omega C} = R\ -\ j\frac{1}{\omega C} \tag{4}$$

In pseudo-linear system, the responding current to a sinusoidal potential will exhibit the same waveform geometry with a phase shift (fig.22).
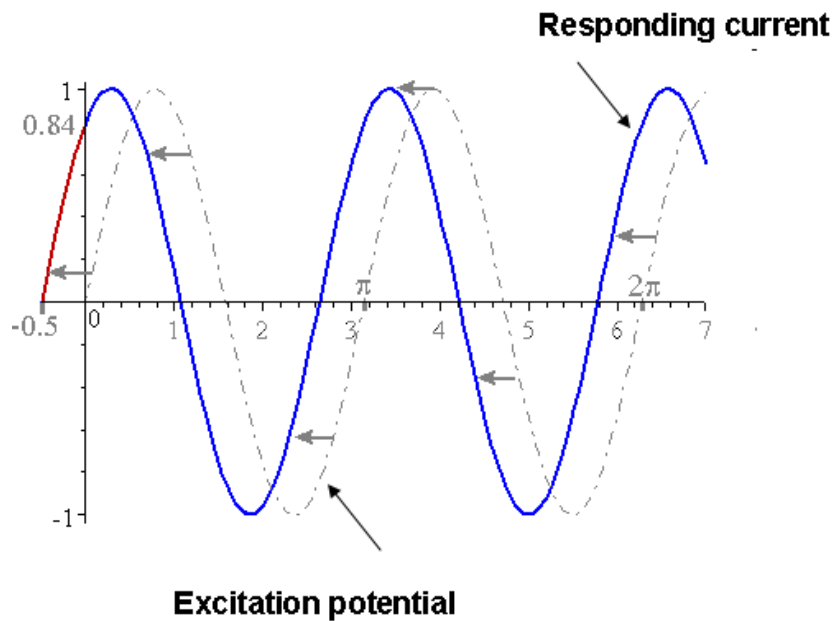
Figure 22. Sinusiodal current response in a pseudo-linear system

The excitation potential can be mathematically expressed as a function of time where E_0 represents the signal amplitude, and ω $(2\pi f)$ represents the radial frequency (eq5).

$$E_t = E_0 \sin (\omega t) \tag{5}$$

The responding current in such system can be expressed as equation (6).

$$I_t = I_0 \sin (\omega t + \varphi) \tag{6}$$

According to the Euler's equation : $\exp(j\phi) = \cos\phi + j\sin(\phi)$, E_t and I_t can be expressed as equation (7) and (8), respectively.

$$E_t = E_0 \exp(j\omega t) \tag{7}$$

$$I_t = I_0 \exp(j\omega t - \phi) \tag{8}$$

Therefore the Z can be derived as equation (9) based on the Ohm's Law where Z_0 or $|Z|$ is the magnitude of impedance

$$Z(\omega) = \frac{E}{I} = Z_0 \exp(j\phi) = Z_0 (\cos\phi + j\sin\phi) \tag{9}$$

Comparing the equations (4) and (9), the impedance Z can also be expressed in polar coordination (figure 23) where $R = Z_0 \cos\phi$, and $X = Z_0 \sin\phi$
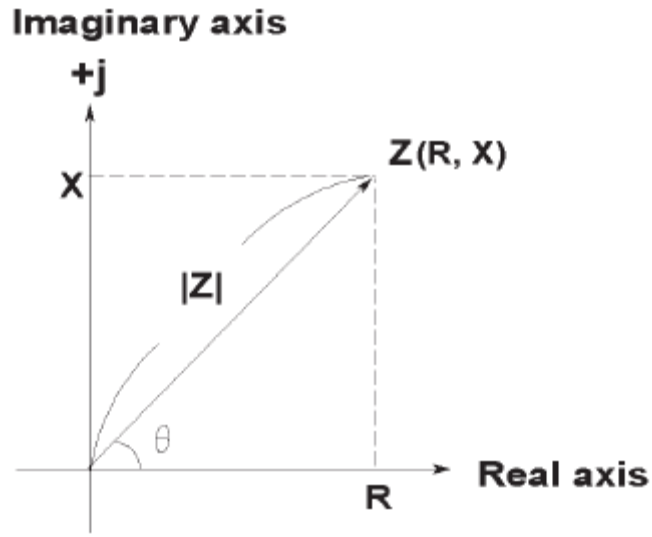
Figure 23. Mathematical expression of Impedance Z in the polar form
as magnitude and phase angle. The phase shift is expressed as

$$\phi = \tan^{-1} \frac{X}{R}$$

Data analysis

EIS measurements monitor the electrical properties corresponding to the change of electrode surface. In the electrode-cell system, single electrons cannot exit in solution, nor ions flow through the metals. This incompatibility is resolved at the metal-electrode interface, where charge is transferred or rearranged to allow current to effectively flow from metal to tissue. In addition, the junction between metal and electrolyte (or any two materials (phases)) will create an area with potential difference [144]. This area is usually termed as electrochemical (or interfacial) double layer. Detail of the double layer will be addressed in later chapter (Ch6).

During the implantation, bio-material interaction through chemical reactions

alters the surface characteristics such as chemistry, surface morphology, roughness, and

thickness of interface. The electrode surface undergoing such interaction (reaction) will

lead to the alteration of charge transport pathway in the double layer, and the essential

electrical properties. The EIS measures the dielectric properties of the material interface

and the electrode impedance as a function of frequency and delivers the analytical

spectrum. In EIS test, two type of graphical data set are obtained, which are Bode plot

and Nyquist plot.

The graphical bode blot represents the gain of the system. It gives the magnitude

of impedance ($|Z| = \sqrt{(\text{Re}(Z))^2 + (\text{Im}(Z))^2}$) and the phase change as a function of

frequency. Figure 24 shows a typical bode plot. The magnitude of Z and the frequency is

usually presented in logarithmic scale. The phase shift is usually presented in between -

180° to +180°.

The graphical Nyquist plot represents the real versus imaginary components of

the impedance under the given frequency. It displays both amplitude and phase and uses

frequency as an independent parameter. For each data point (dot) shown in the nyquist

plot, it provides the corresponding relationship between R and X components at each

particular frequency. Phase shift can also be obtained by the vector of length Z (fig.25).
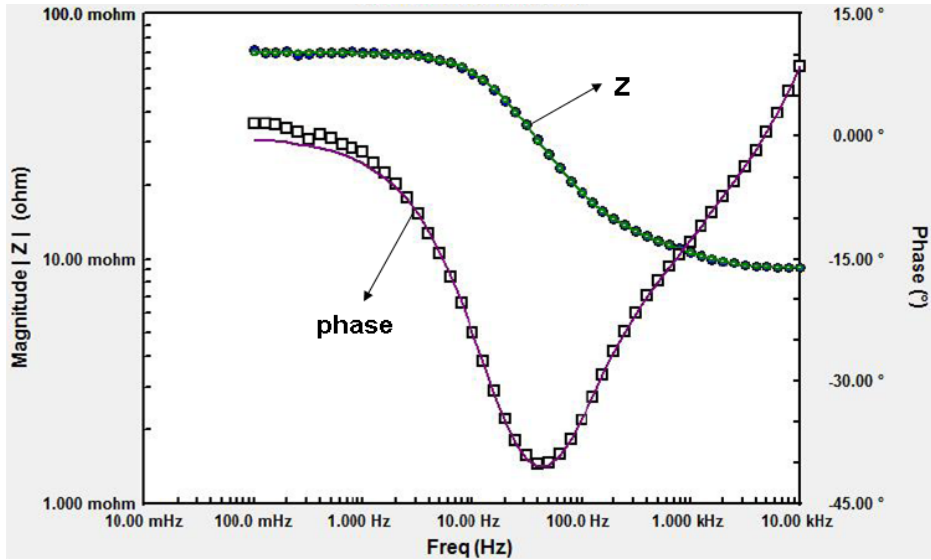
Figure 24. Bode plot of Impedance test. X-axis represents the frequency of ac potential. Left Y-axis represents the Z magnitude and Right Y-axis represents the phase shift.
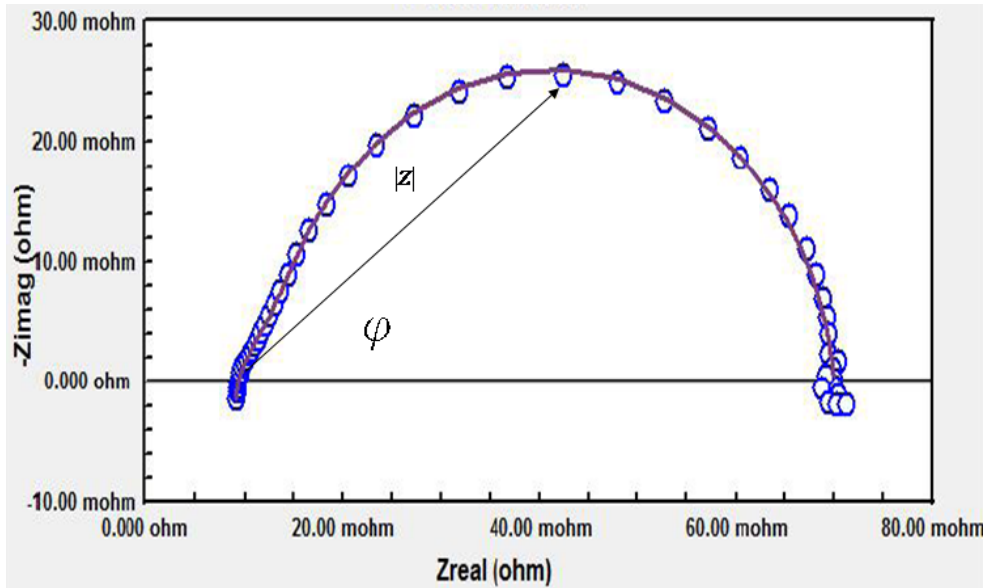
Figure 25. Nyquist plot of Impedance test. X-axis represents the real component of Z. Y-axis represents the imaginary component of Z. The angle between the vector Z and the X-axis is the phase shift.

Based on the information provided from Bode plot and Nyquist plot, we will be able to calculate the system resistance and the capacitance. Equilibrium circuit model can also be established in order to obtain to pin point electrical components affecting properties of electrodes.

EIS testing

In this study, 3 point evaluation method was used (fig.26). EIS300^{Tm} Electrochemical Impedance Spectroscopy was used for impedance spectra measurement. The three-electrode measuring cell is constituted by a working electrode which is the retrieved implanted electrode from the insect, a platinum counter electrode, and a SCE reference electrode (potassium chloride) for experimental investigations. Measurement was conducted in 0.9 wt% NaCl solution.
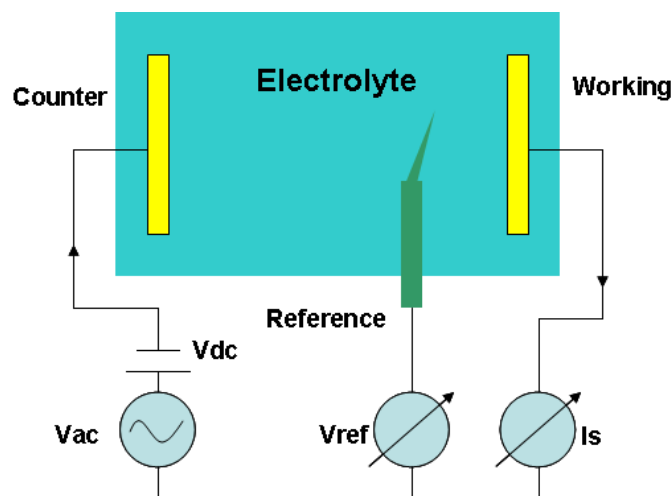
Figure 26. Representation of EIS measuring cell. Current meter(IS) measures the responding current and Vref measures the potential. Vac delivers the perturbation voltage.

To avoid misinterpreting the variation of electrode properties since the electrode potential is constantly changing [120, 121], constant potential method was applied while measuring the impedance properties. The potentiostatic EIS mode was selected to acquire an impedance spectrum using 5mv sinusoidal perturbation ac waveform over a range of frequency from 1 Hz~100 KHz. Complex impedance data was collected by means of EIS300 software and were in the form of Bode and Nyquist plots. Circuit modeling was also performed to analyze the impedance spectra to understand the formation of an electrode-immune system interface.

Histological analysis

Background

Histology is a microscopic study of biological tissue or cell. It studies their anatomy via light or electronic microscope. It provides the ability to visualize or differentially identifying microscopic structure of the examined samples. The process of histological study usually contains fixing, processing, and sectioning and staining. The purpose of fixing process is to preserve tissue from degradation and maintain the structure of cellular components. The process is usually done by chemical or frozen section fixation. In chemical fixation, the additive will create the cross-link amino groups in the proteins through the formation of methylene linkage (fig.27).

Figure 27. Chemical fixation process. The cross-link between the
protein will be created by the formation of CH$_2$ bond. This process will
maintain the tissue structure.

The next important process is the staining. Biological tissue usually exhibit little
inherent contrast under either light or electron microscope. The staining process is
employed to give contrast to the tissue as well as highlighting the particular cytological
feature of interest. Vital dye is commonly used for staining process since the chemical
composition of the stain does not kill the living cell. Table 6 lists of common vital stains,
their fluorescent colors, and the common staining subjects.

Table 6. List of common vital dye

Type	Fluorescent	Staining subject	annotation
Eosin	red	Cytoplasm, collagen, muscle fibers	Dye exclusion
Propidium iodide	Dark red	DNA, fluorescein-labeled antibodies	Differentiate necrotic, and apoptotic
Trypan Blue	blue	Dead cell membrane, tissue	Living-cell exclusion
Erythrosine	Red(cherry-pink)`	Food coloring	Exclusion dye

The internal organs of an American cockroach are surrounded by hemolymph in an open circulatory. It's inevitable that the electrode to be introduced into the roach's body will encounter the hemolymph. The major component of hemolymph is the hemocytes (blood cells). It protects the internal system from the bacteria and foreign substances by biological "immune-type" reactions in terms of phagocytosis, and encapsulation [145]. We hypothesize that the interface properties are dominated by the interactions between the electrode and the hemolymph. The Propidium iodide was chosen as the stain since it has the ability for revealing the DNA of the cell.

Histological procedure

The electrodes were first preserved in the Kahle's fixator for 24 hours for cell and tissue fixation after being retrieved from the insect's body. The Kahle's solution used in this study was ethanol (28%), formaldehyde (11%), glacial acetic acid (4%), and water (57%) mixture. Propidium iodide (100 μ g/ml) was used for nuclei staining of hemocyte. The reserved electrodes were placed in the diluted propidium iodide (1:500 of Phosphate buffered saline) for 10 min and rinsed in buffered saline for 10 seconds. Samples were later imaged with filters for red fluorescence under OLYMPUS FV1000 confocal microscope in Micro Imaging Center of TAMU.

X-ray photoemission spectroscopy

Background

  X-ray photoemission spectroscopy (XPS) is a surface analytical tool which is used to detect the chemical composition of a substance[146]. The measurement provides quantitative analysis of the electron shell, chemical state and electronic state of an atom [147]. Each element or atom has its particular electronic binding energy, which can be determined by the XPS measurement.

  The sample analysis is usually performed under the high vacuum around 10^{-10} torr. During the measurement, the sample is irradiated with the incident x-ray where the photons bombard the sample surface (few nanometers in depth). The bombarded electrons will be excited and shift from the equilibrium state to the subshell. With the sufficient photon energy, it provokes the photoelectric effect where the excited electrons will be emitted into the vacuum [148]. The energy of emitted electrons is associated with incident and binding energy (fig 28). Each electron shell has unique binding energy; therefore, the electron kinetic energy of electrons from each shell is unique as well.
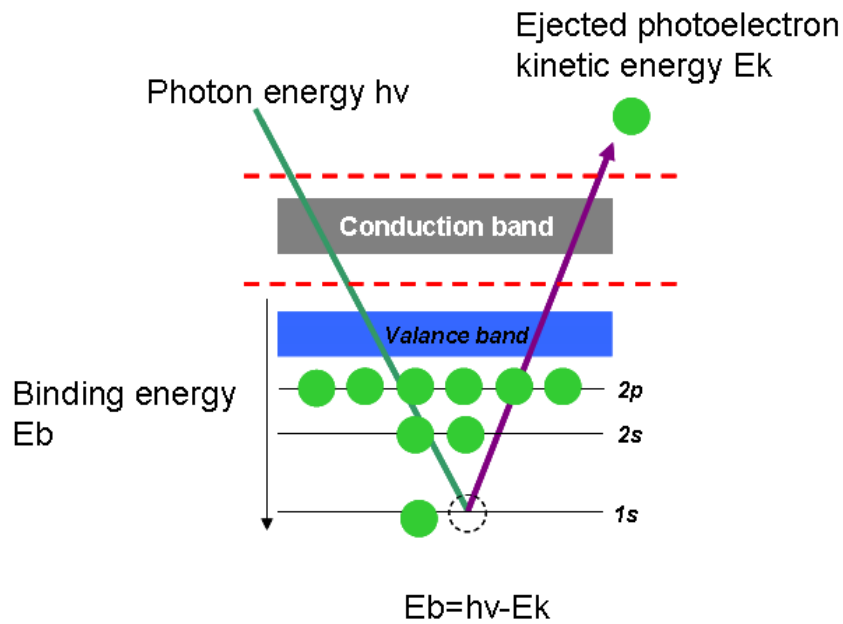
Figure 28. Photoelectric effect. The excited electron emits out of the material. The kinetic energy of the emitted electron (Ek) = Photon energy (hv) – Binding energy (Eb) or $Eb = hv - Ek$

The emitted photoelectrons are admitted through a hemispherical analyzer with uniform magnetic field (fig.29). Due to the unique characteristic kinetic energy of each electron, the interaction to the magnetic field results in the different bended trajectory. Each electron will hit the different position at the detector. The position of the photoelectron will lead to the characteristic kinetic energy after evaluating the effect of electron impact and the magnetic field.
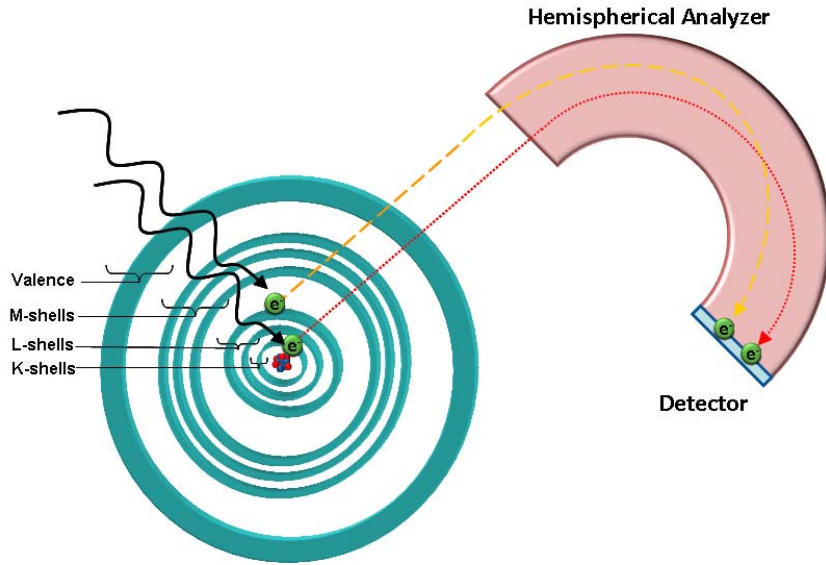
Figure 29. Principles of XPS operation. Sufficient energy of photons
will cause the photoemission. Different chemical and electron state of
the atom will be captured in different position of the Detector.

In a typical XPS spectrum, the binding energy is used as X-axis where the peak

intensity is used as Y-axis (fig.30a). The X-axis typically shows the decrease of binding

energy. The signal intensity should consider the incident X-ray flux, refracting

coefficient, and X-ray attenuation length. The electrons emitted out of the material

vertically to the sample surface (fig.30b). For a volume component of the sample with

thickness dz at the distance Z beneath the sample surface, the signal intensity of x-ray at

depth Z can be calculated by the equation 10. The γ is incident x-ray flux. r is coefficient

of reflection.

$$\gamma(1-r)\frac{\sin\phi}{\sin\phi^{\mathrm{l}}}\,e^{\frac{-z}{\lambda_{hv}\sin\phi^{\mathrm{l}}}}$$

(10)

λ_{hv} is the x-ray attenuation length. φ is the incident angle and φ^1 is the refraction angle. In most cases, the x-ray influx is unknown. Comparing the peak ratio to calculate the atom percentage of the sample component turns out to be the most common method.
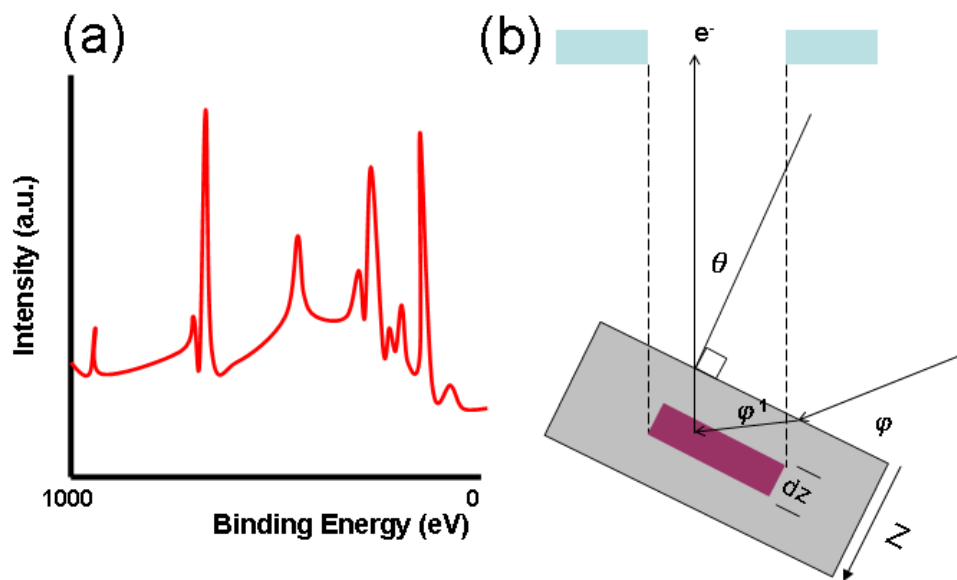
Figure 30. Representation XPS spectrum. (a) Illustrated full scan of XPS spectrum. The position of the peak is corresponding to the binding energy of excited element. (b) The intensity gain theory of XPS measurement.

Spectroscopic data analysis

Spectrum deconvolution is commonly used for analyzing spectrum data. It provides the qualitative and quantitative analysis by extracting the raw XPS data. As it is shown in figure 30a, each signature peak represents an excited electron at particular electron orbit. In many cases, the outermost orbit has much environmental interaction than the inner orbits. Therefore, the outermost shell has significant interest for studying

the chemical or electronic state of an atom. Environmental interaction usually creates the different neighboring atoms in the surrounding matrix in the outermost shell which forms smaller peaks. This new forming peaks convolute into a large peak which has the peak shifting (chemical shift), or (and) dissymmetry compared to the signal of original orbit. Spectrum deconvolution can obtained the useful information of each peak to determine the surface composition and reaction mechanism.

In this study, the XPS measurement was performed at SSRL (Standford Synchrotron Radiation Light source) beamline 8.0 using a cylindrical mirror analyzer (CMA). Spectrum deconvolution was conducted using XPSpeak software with Shirley background removal method and Lorentizian-Gaussian modeling curve.

Raman spectroscopy

Background

Raman spectroscopy is the method used to study the vibration mode by assessing molecular motion of the material surface. Raman spectrum can be used to determine the material composition, stress/strain state, crystal symmetry and orientation [149-151], among others. The principle theory of this spectroscopic technology is based on the inelastic scattering of a photon. According to the classic electromagnetic theory, the scattered monochromatic irradiation changes the molecular vibration by inducing electrical dipole momentum. This molecular vibration is determined by the interaction of electrical field and molecular polarizability.

In quantum theory aspect, the interaction between the photons and molecules triggers the elastic and inelastic collisions. The excited molecules shift from ground state to virtual energy state. In Rayleigh Effect (elastic), the molecule returns to the original state when the light is scattered. In Raman Effect, the molecule returns to a different rotational state and emits a photon during molecule relaxation. Under such circumstance, two different scattering can happen: Stokes and Anti-Stokes Raman scattering. When the molecule returns to the higher rotational energy state, part of energy will be given to the vibrating molecules. Such process is referred as Stoke scattering. On the contrary, the emitted photon receives energy from the vibrating molecule when it returns to the lower rotational energy state. This is referred as Anti-Stoke scattering. Raman spectroscopy measures this energy differences between the incident source and the scatted photon, which leads to the frequency shift from the excitation wavelength. Figure 31 presents the energy states in Raman signal.
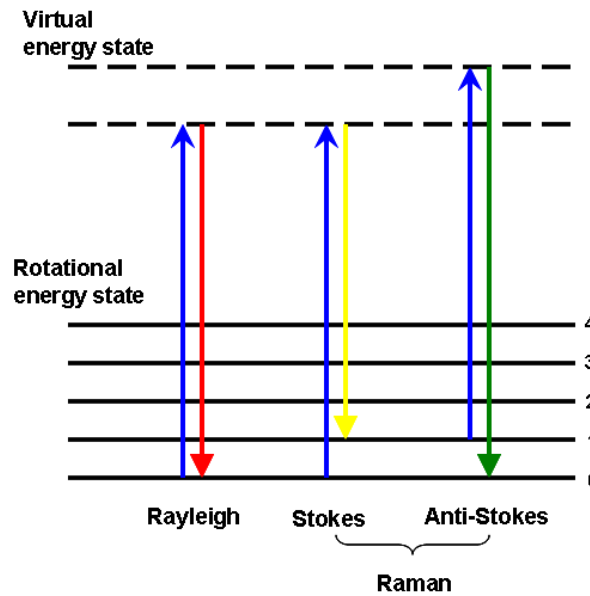
Figure 31. Illustration of energy States for different scatterings in
Raman signal.

Typical Raman spectroscopy uses laser or UV source for object illumination. The

intensity of Rayleigh scattering is usually several magnitudes higher than the Raman

scattering. The key for spectroscopic setup is the separation of Raman scattering from

Rayleigh scattering. The use of Rayleigh filter in instrumental setup can efficiently

resolve Raman scattering. In addition, multiple dispersion stage is also employed for

detecting the smaller wavelength. Figure 32 presents the conceptual instrumental setup
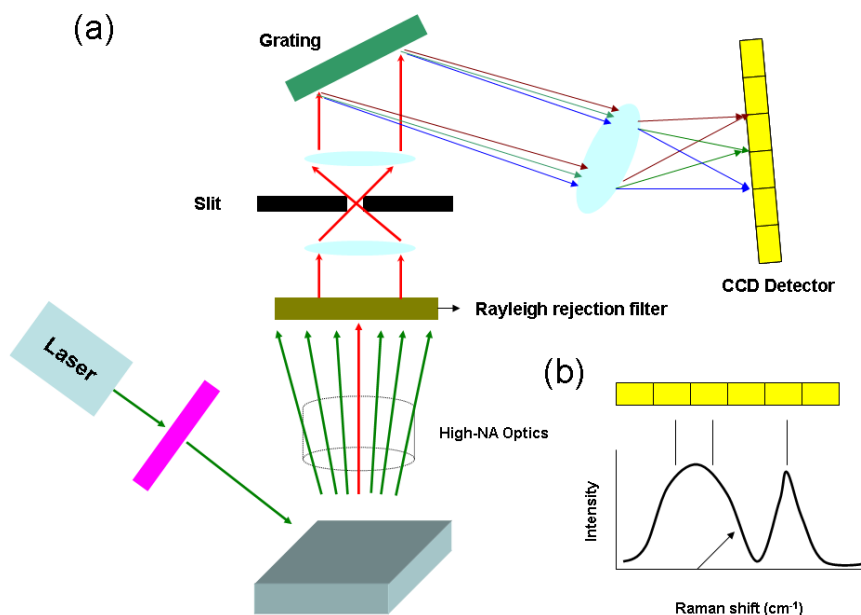
Figure 32. Conceptual Raman Spectroscopic operation (a) Instrumental
setup. (b) Spectrometer resolution

Spectroscopic data analysis

As it's shown in figure 32, the scattered photon will be guided to the CCD

detector. The spectral resolution is determined by the convolution of the entrance slit

with the CCD pixel. Raman spectrum (fig. 32b) provides information of intensity of

scattered photons (Y-axis) versus the Raman shift (X-axis). Since each material has

particular inelastic scattering, the signature Raman shift shown in the spectrum is

generally used for structural determination.

In this study, HORIBA Jobin-Yvon LabRam system of Raman Spectroscopy was

used for confirming the graphene structure. The G band (1582/cm) and G' band

(2700/cm c) are the most prominent peaks for monolayer graphene in Raman spectrum

[152]. The 2D band (1350 cm^{-1}) can also be observed in graphene sample whose frequency is about half of G' band. Typical monolayer graphene feature exhibits intensity ratio of G/2D ~0.5, and symmetric 2D peak [153]. Those signatures of Raman shifts were employed for structural analysis.

Atomic force microscopy

Background

Atomic force microscopy (AFM) is a high resolution microscopy. It is constructed by a scanning probe mounted on a cantilever where the position of the probe is controlled by a piezoelectric element. This setup facilitates the precise movement of the probe using electrical potential to control the displacement in X,Y and Z direction of the piezoelectric material. Figure 33 shows the schematic diagram of the AFM. The probe is brought to the sample surface. Due to the force generated between the AFM probe and the measured sample, the deflection of the cantilever is generated. Such deflection can be detected by the incident laser, in which the reflected laser is monitored by the array of photodiode.
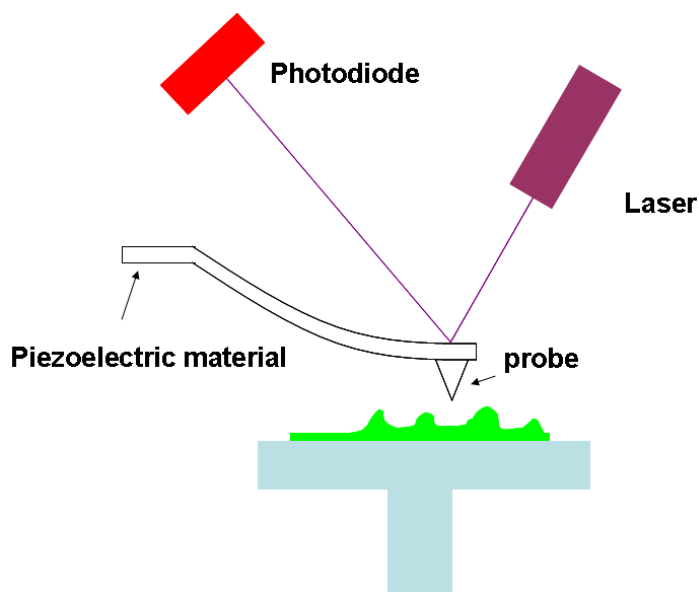
Figure 33. Schematic diagram of AFM

Electrical response of graphene

In this study, Nano-R AFM (Pacific Nanotechnology, Inc) was used to measure the current responds of graphene. The contact mode was selected for scanning operation. The graphene was firstly transferred to the copper wafer using the same method described previously (graphite exfoliation). The copper wafer was connected to a Pico-meter which was used to detect the current output. During the scanning, a DC potential was constantly applied to the probe and the responding signal was measured. Figure 34a shows the schematic diagram of AFM operation.

The applied potential was preset at 0mV and gradually increased to 400 mV in 100mV increment every 15 seconds (fig.34b), where the measured current was exported in excel file. In this experiment, the electrical potential was applied to the graphene

surface and the copper in close vicinity of graphene (less than 20μm). The experiments were conducted from 0 hr, 1hr, 4hr, and 8hr to monitor the electrical responds of graphene over time. Fig. 34c shows the illustration of the responding current. Data was continuously recorded every 1msec, which is equivalent to 150 data points for each applied potential. The mean value and standard deviation of the recorded data will be presented as electrical response and will be discussed in chapter 5.
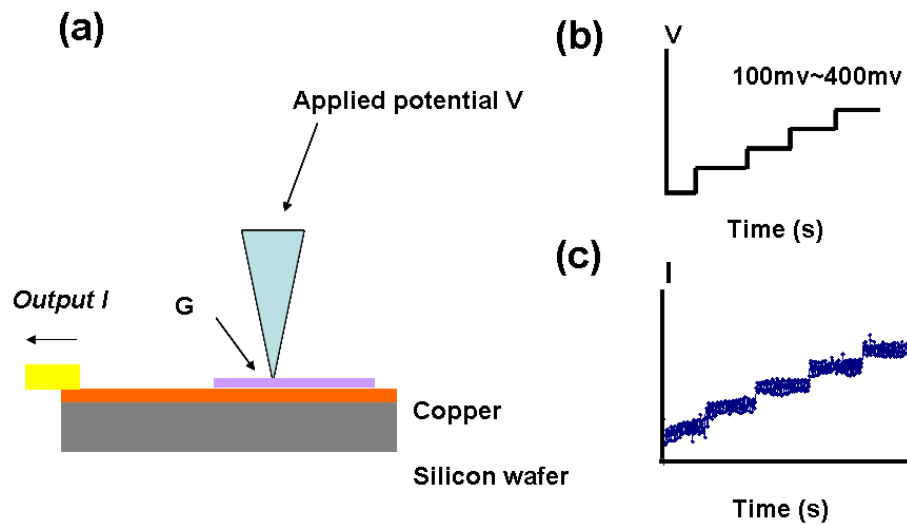
Figure 34. Schematic diagram of AFM. (a) The DC potential was applied at the scanning probe, where the current output was measured by a Pico-meter. (b) Illustration of applied potential. The signal was applied from 0~400 mV in 100 mV increment. (c) Illustration of responding current.

CHAPTER IV

ELECTRODE-IMMUNO INTERFACE[*]

In this chapter, the variation of electrical properties due to the interaction between electrode and insect's neural system will be firstly discussed on investigation using the Electrochemical Impedance Spectroscopy (EIS). The degradation of electrode and the alteration of charge transfer at interface will be discussed using EIS data. Spectroscopic and histological analysis to the retrieved electrodes will be employed to evaluate the chemical and bio-chemical effects on electrode.

Electrical degradation of electrodes

For all impedance experiments, characteristic impedance for each electrode was measured prior to the implantation in order to create a baseline. All experiments were done in 0.9 wt% sodium chloride solution. As it was mentioned in chapter 3, silver electrodes were implemented as neural implant. The impedance magnitude ($|Z|$) across the given frequency range was shown in Bode plots. Variations of real and imaginary pairs of impedance were described in Nyquist plots. Below are some detailed discussions.

---

[*] Part of this chapter is reprinted with permission from "Electrode-immune system interface monitor through neural stimulation in American cockroach (*Periplaneta americana*) by Cheng-Wei Chiu, Jorge M. Gonzalez, Mark Harlow, S. Bradleigh Vinson, Hong Liang, Electrochimica Acta, 68, 81-87, Copyright (2012) by Elsevier.

Frequency domain analysis

Figure 35 shows the impedance magnitude with various implanted times under 1V-1Hz stimulation parameter. Each spectrum represents the mean value over 10 experimental results, where the error bar represents the standard deviation. Impedance magnitude in each spectrum exhibits a decreasing trend in value against the increase in frequency, which is the typical electrical behavior for metal. Noticeable increasing trend of the impedance magnitude is also observed with the increase of time.
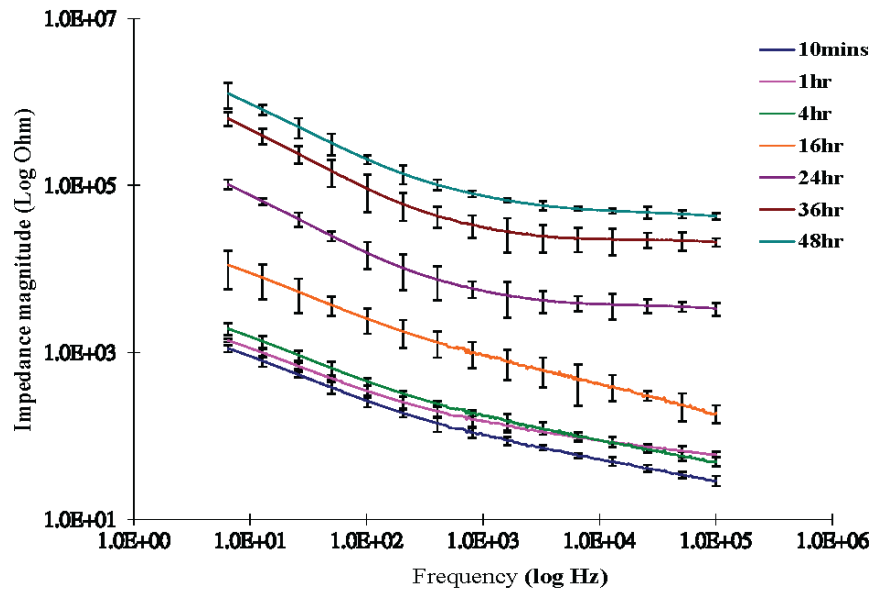
Figure 35. Bode plot of impedance spectra with 1V-1Hz electrical
stimulation results with different implanted time.

In order to study electrode patency in neurophysiologic experiment $|Z|$ is usually measured at 1 KHz. This particular frequency was selected because its similarity to the pulse frequency of action potential in extracellular neural recording [121]. The

impedance magnitude at such frequency is associate with the interfacial response of the implanted electrode to the action potential. The impedance magnitudes at 1 KHz over 48 hours implanted time were plotted in figure 36.

As mentioned in Ch3, two experimental conditions of implanted electrodes were taken into measurement. First is the implanted electrode with applied electrical stimulation, and the other is the control group. In figure 36, the blue line and the red dash-line represent the stimulated group and the control group, respectively. Each data shown in this figure is the mean value of impedance magnitude which was derived from 10 experiments. The error bar shown in the figure is the standard deviation. The average impedance magnitude increases for both experimental conditions. A significant increase in impedance magnitude after 24 hours implanted time was observed in both groups. The impedance average in the stimulated group is slightly higher than that of the control group at the first 16 hours implanted time (fig. 36a). Such differences and the trend in increase diverge after 24 hours implanted time (fig. 36b). The average impedance value of the examed group becomes several magnitudes higher than that of the control group. The corresponding increment of the impedance magnitude in entire duration suggests the degradation of the electrode.
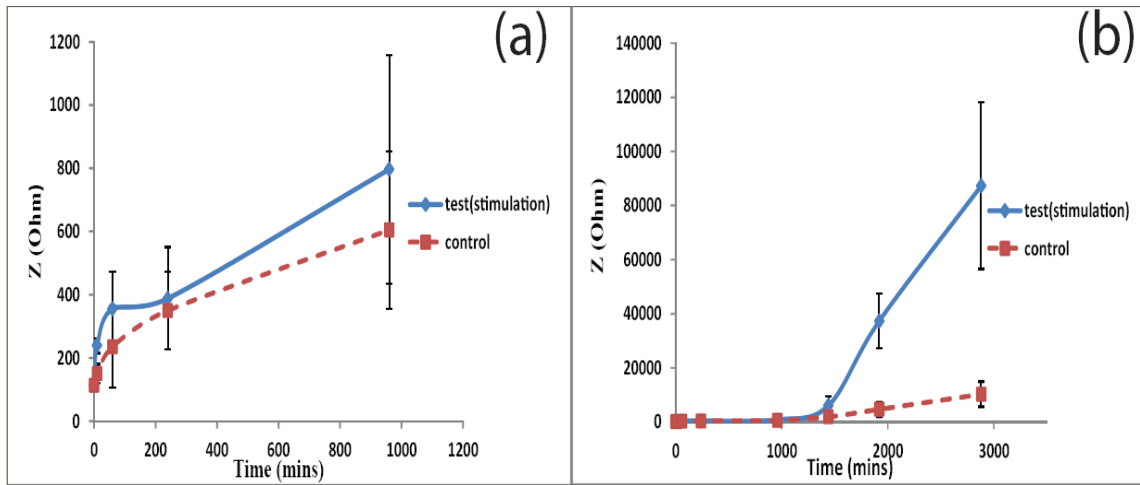
Figure 36. Impedance magnitude measured at 1KHz. (a) First 16 hours implanted time. (b) Implanted time from 10 mins ~48 hours. The solid line (blue) represents the measured results with electrical stimulation. The dash-line (red) represents the control group.

Alteration of charge transfer

To evaluate the change of the interface in electrode-bio system, the information provided by Bode plot was not sufficient. The Nyquist impedance loci of stimulated group, which is shown in figure 37, exhibits the variability in the real and imaginary components for the first 16 hours implanted time. Each color of impedance loci represents the results at different implanted time . Both real and imaginary components monotonically increase and the spectra exhibit linear R-X relationship. As the impedance magnitude increases over time (fig 36), the variability in the real and imaginary components at the given frequency increases as well. The impedance loci in figure 37 therefore show corresponding increase across the electrodes on subsequent implanted time.
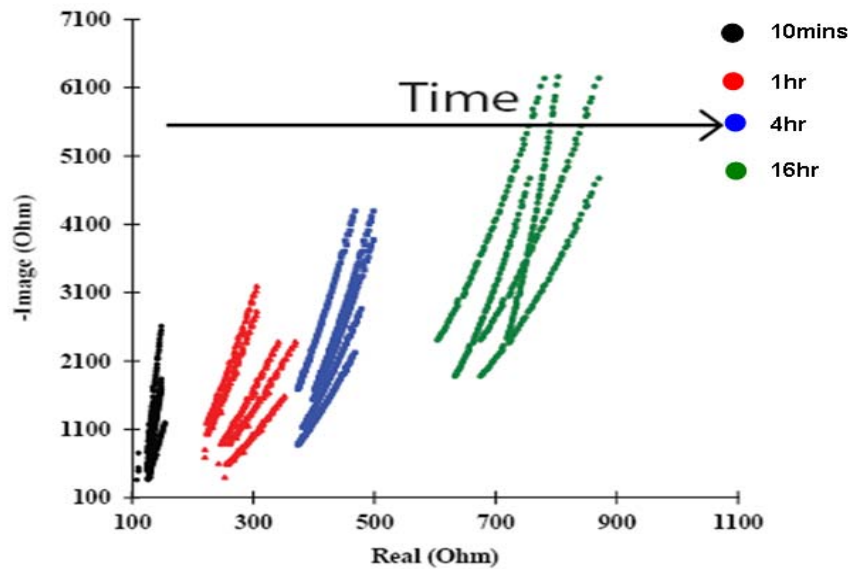
Figure 37. Nyquist plot of Impedance spectra for the first 16 hrs
implanted time.

The Nyquist impedance loci of stimulated group across 48 hours implanted time were plotted in figure 38. The R-X relationship starts to exhibit non-linear behavior at 24 hours (fig.38a). The real component of impedance exhibits large variability in each locus after 24 hours implanted time. After 48 hours implanted time, the impedance loci in high frequency range exhibits a form of semi-circle arc (fig. 38b). This indicates the presence of a parallel RC component in the system where R is the charge transfer and C is the capacitance. Independence of frequency in the impedance loci suggests the changing composition of the charge carrier on the electrode surface. The detail of this R-C effect will be discussed later.
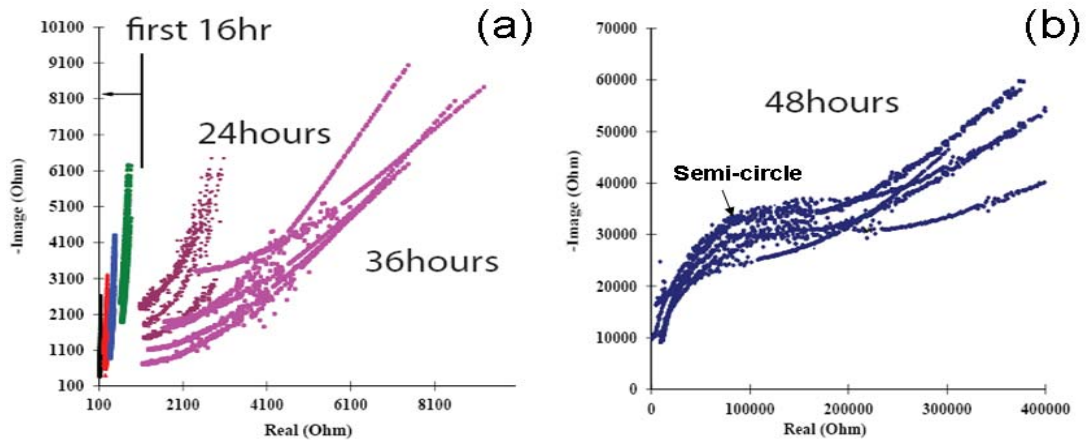
Figure 38. Nyquist plot of Impedance spectra across 48 hours implantation. (a) The first 36 hours implanted time. (b) 48 hours implanted time. The form of semi circle arc refers to the presence of parallel RC circuit.

Chemical interaction

To identify the chemical interaction between the silver electrode and host neural system, the chemical state of the electrode surface was investigated using X-ray photoemission spectroscopy (XPS). The scans were operated in survey mode where the sweeping energy range covers Silver-3d, Carbon-1s, and Oxygen-1s peaks. Carbon-1s peak is commonly used as a reference because carbon element is thermally and chemically inert. The scanned spectra were adjusted to match the C-1s peak in order to compensate the instrumental deviation..

Double peak structures with binding energy at 368.24 eV and 374.25 eV are the strongest spectral signals of silver in XPS. These two peaks represent the photons

emitted from the Ag3d core region which are Ad 3d $_{5/2}$ and Ag 3d $_{3/2}$ region, respectively [154]. Table 7 summarizes the characteristic of silver peaks in XPS spectrum.

Table 7. Binding energy and peak widths of Silver as measure with monochromatized Cu $K\alpha$

Signal	B.E (eV)	FWHM (eV)	G: L Ratio (%)
Ag 3d 5/2	368.24	0.49	60
Ag 3d 3/2	374.25	0.49	40

The XPS spectra shown in figure 39 are the normalized XPS spectra of the silver and 24 hours implanted silver electrode. The spectrum of 24 hours implanted electrode exhibits asymmetrical peak, which indicates the peak might be the convolution of several small peaks. The spectrum of 24 hours implanted electrode shifts toward lower binding energy position about 0.6 eV for both sub-regions of Ad 3d core region. In addition, the peak width (FWHM) also increases. Those evidences are associated with the existence of silver oxide on the electrode [155, 156].

The negative shift of binding energy shown in figure 39 is different from other oxidation states of metals, which is usually positive shift. Generally, lower electron density of cation in the valence region of the metal oxide causes the positive shift of binding energy in XPS spectrum [155, 157]. The negative shift in binding energy at Ag 3d region is the characteristic of silver oxide. This characterization could be governed by lattice potential effect and extra-atomic relaxation energy [158].
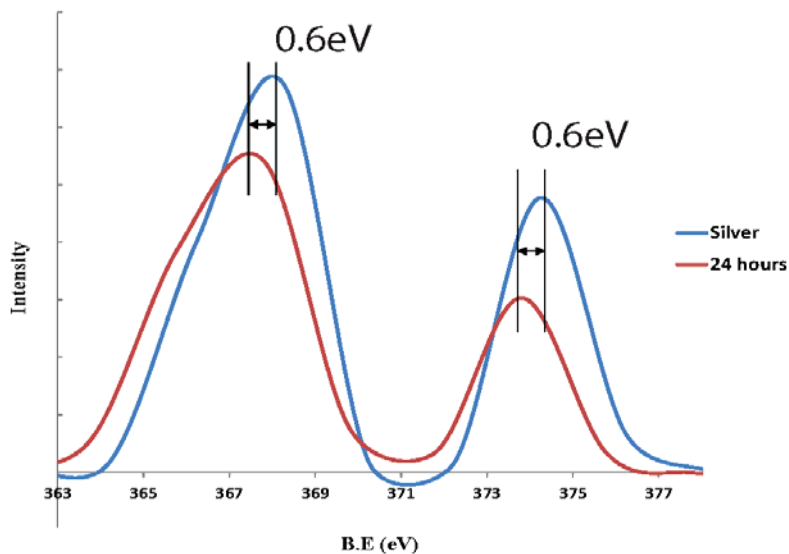
Figure 39. XPS spectra of silver and 24 hours implanted silver
electrode.

As mentioned in Ch3, several small speaks would convolute into a large peak in XPS spectrum. To further investigate the presence of any silver oxide, the spectrum of Ag 3d core level regions for 24 hours implanted electrode must undergo a deconvolution process. The peak identification of XPS deconvolution was referenced from the handbook of Monochomatic XPS spectra [154].

Deconvoluted data demonstrates the presence of multiple states of oxygen in Ag3d core level region (fig. 40). Two spin orbit signals exist in each oxidation state. The components with binding energy at 367.08 eV and 373.08 eV indicate the presence of AgO. The binding energy at 367.67 eV and 373.62 eV indicate the presence of Ag_2O. The spectral characteristics for each oxidation state of silver are summarized in Table 8.

74

Table 8. Binding energy of Oxidation state in Ag 3d core region.

Element	Position (eV)	Area	FWHM (eV)	%GL (%)
Ag in AgO $3d_{5/2}$	367.080	0.552	0.80	84
Ag in AgO $3d_{3/2}$	373.080	0.277	0.81	81
Ag in Ag_2O $3d_{5/2}$	367.670	0.432	0.80	80
Ag in Ag_2O $3d_{3/2}$	373.620	0.317	0.80	80
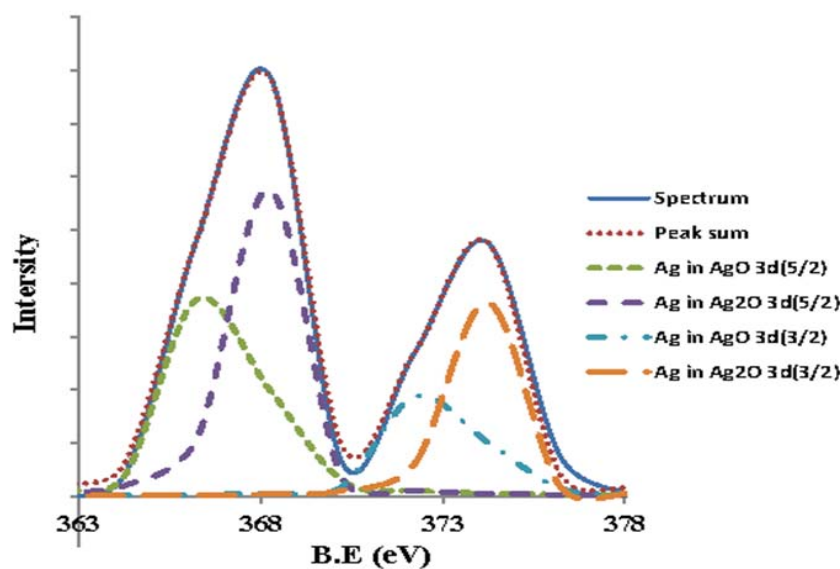
Figure 40. Deconvolution of XPS spectrum at Ag3d core region.

Figure 41 shows the deconvoluted spectrum in Os1 core region. The same oxygen states are observed as well as those found in Ag3d core region. The peak representing the oxygen in Ag_2O locates at a B.E of 528.62 eV, and the peak representing the oxygen in AgO locates at a B.E of 530.1 eV. Other peaks found in this core region were ascribed to the carbonates and the adsorbed water [159, 160]. The

spectral characteristics of the deconvoluted results in Os1 core region are summarized in

Table 9.
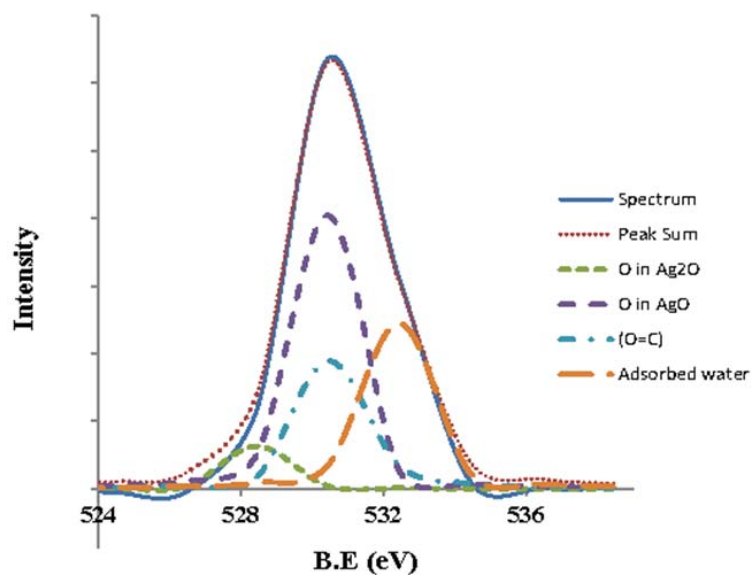
Figure 41. Deconvolution of XPS spectrum at Os1 core region.

Table 9. Binding energy of Oxidation state in Os1 core region.

Element	Position (eV)	Area	FWHM (eV)	%GL (%)
O in Ag2O	528.620	0.590	0.970	80
O in AgO	530.100	0.944	1.200	80
(O=C)	530.820	0.511	1.400	90
Adsorbed water	532.210	0.100	1.430	90

Hemolymph of the insect contains various dissolved organic substances

including free amino acids, proteins, and sugars, etc. American Cockroach (as all insects)

uses hemolymph as a medium to transport metabolic compounds which is synthesized in fat body cells [161]. The constituents of hemolymph contain large amount of oxygen bonds or the functional groups. As the electrode implanted in the neural system, this oxygen-rich environment directly interacted with the surface of electrode which resulted in silver oxidation. The results of spectroscopic analysis confirm the presence of multiple oxidation states of silver. However, at this stage it is not clear which oxidant participated in the formation of the oxide.

The influence of silver oxide to the electrical properties of the electrode depends on the growth of oxide layer. In addition, the electrical property of oxide layer is majorly determined by its thickness. According to the Fickian transport mechanism, the diffusion rate of molecules is inversely proportional to the thickness of that layer (eq. 11). In this equation, y is the thickness of oxide film, K is the parabolic rate (diffusion rate), and t is the time

$$\frac{dy}{dt} = \frac{K}{y} \rightarrow y^2 = K.t \tag{11}$$

The growth rate of the silver oxide, which relies on diffusion, represents a parabolic trend and has the tendency to reach an asymptotic value [162, 163]. The relationship between the thickness versus time of several naturally grown metal oxides are presented in figure 42 [162]. Due to the diffusional limitation, the thickness of silver oxide is confined as well as its influence to the interfacial electrical properties of the electrode. However, the EIS result shows continuous increase of the impedance

77

magnitude (fig 36). In this study, it is believed that other factors should be taken into account in order to investigate the interface of electrode-bio system.
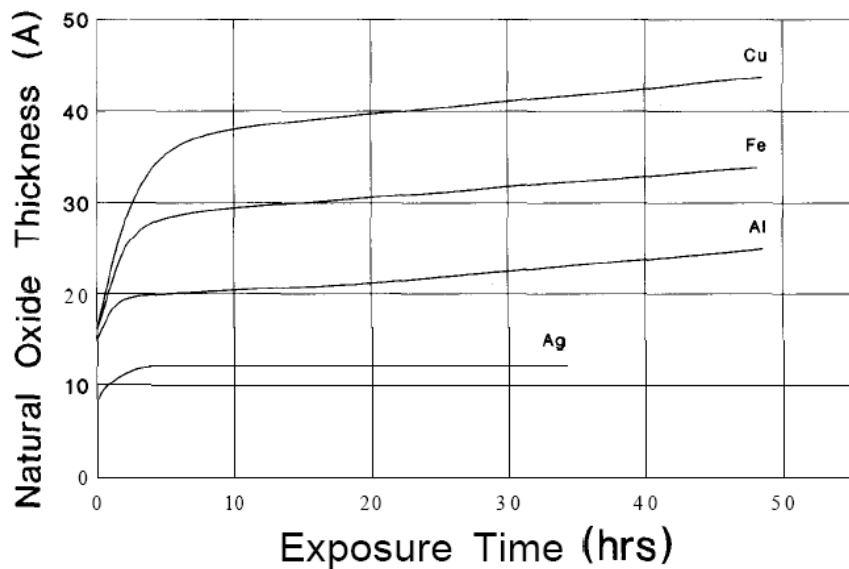
Figure 42. Thickness of oxide formed on different metals at room temperature [163].

Bio-interaction

As mentioned in the previous section, the chemical compound of silver oxide is not the only components of the interfacial constitution. Hence the bio-substances formed due to the biological interaction between electrode and host neural system should also be considered.

The histological analysis was conducted to identify the biological features. This approach determines the biological element on the electrode surface, which also caused

the electrical degradation of electrode. Figure 43 shows the brightfield image taken by

confocal microscope of 48 hours implanted sample. The surface of the implanted close-

paired electrodes was covered with nearly transparent object. The sub-figure is the

epifluorescence image of the marked area. The red dots indicate the nuclei of the cells

stained by Propidium iodide. The result suggests that the bio-element which interacted

with the implanted electrode was the blood cell, hemocyte. This interaction led to the

formation of a coating layer on the surface.
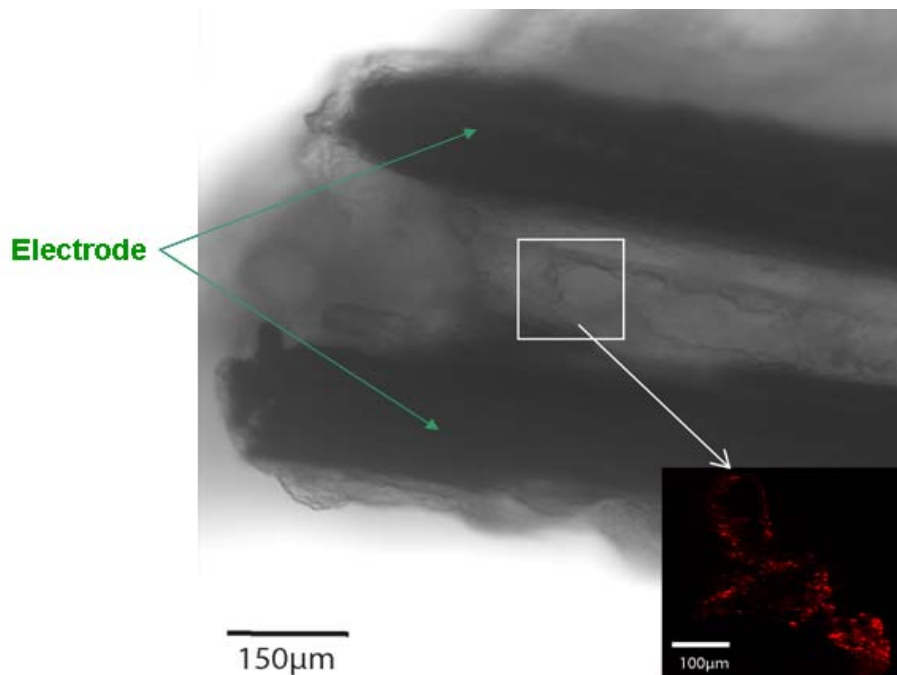
Figure 43. Confocal image of 48 hours implanted electrode. The sub-
image is the epifluorescence image of the marked area

To further investigate this cellular interaction, the histological images of the

implanted electrode with different experimental conditions were taken to provide more

information. Histological images were taken using Olympus FV1000 confocal microscope under Z series mode. The Z series is a vertical sequence of optical section by step-by-step fine-tuned focal depth of the lens for image acquisition. Image sets were collected at different depths of the tissue sample and were reconstructed to form a three dimensional image.

Figure 44 represents the epifluorescence images of 48 hours (fig 44a) and 24 hours (44b) implanted electrodes with electrical stimulation. The images were selected at Z=10 μm beneath the scanned surface from the pile of reconstructed files. It's noted that the cell density on the electrode surface for 48 hours implanted time is much higher than that for 24 hours implanted time.
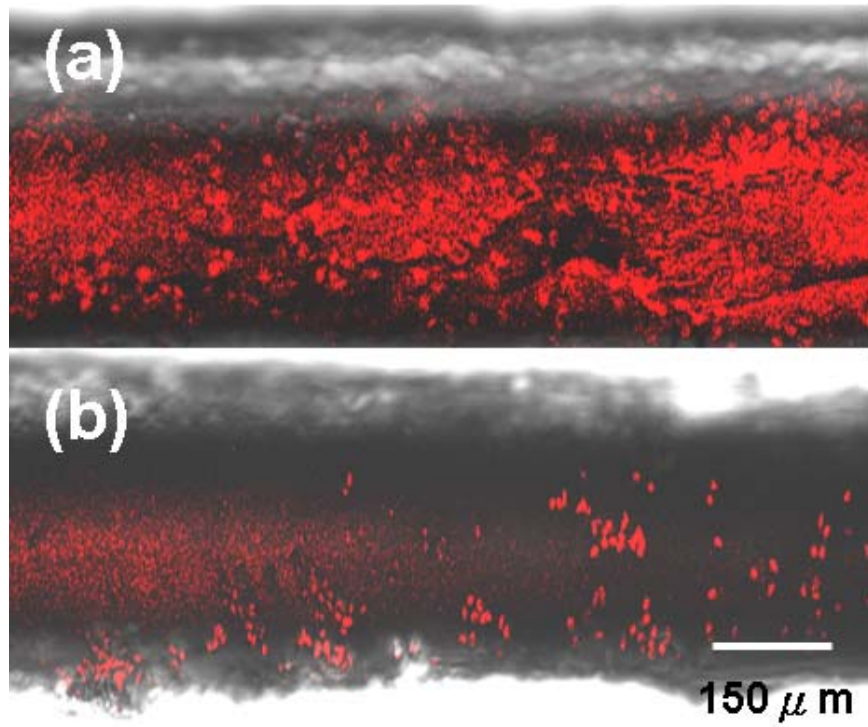
Figure 44. Confocal images of electrode undergone applied electrical
stimulus. (a) 48 hours implanted time. (b) 24 hours implanted time

Figure 45 represents the epifluorescence images of 24 hours implanted electrode

for stimulated group (fig 45a) and control group (fig 45b). Images were selected at

Z=8um beneath the scanned surface. The cell density on the electrode, which underwent

electrical stimulation is much high than the control group.
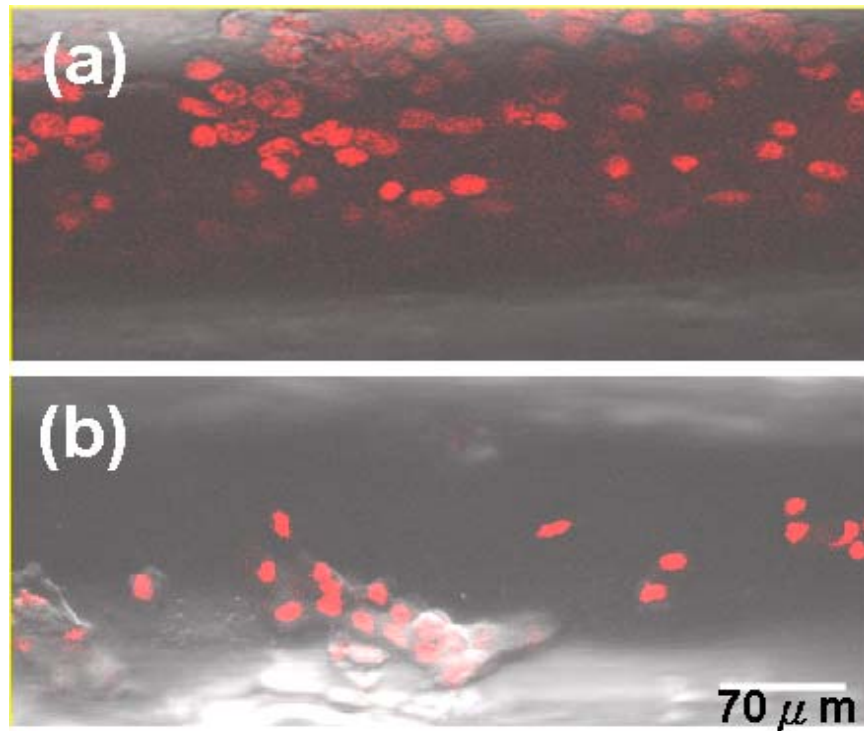
Figure 45. Confocal images of 24 hours implanted electrode. (a) With applied electrical stimulus (test group) (b) Without applied electrical stimulus (control group)

The histological images demonstrate different levels of encapsulating tissue under different experimental conditions. Such results confirm the interaction of electrode-bio system is due to the immuno-type reaction of encapsulating hemocyte. The histological results also correlate to the EIS results. The increase in impedance value and the divergence of increasing trend at different experimental conditions (fig 36) can be explained by different level of encapsulation. Longer implantation leaded to higher density of cell forming on the electrode surface, which caused the increase in impedance magnitude. In addition, electrical stimulation may trigger intense immuno-reaction as the response of higher level of encapsulation. The influence of oxide on system impedance

is limited due to the parabolic growth rate of silver oxide (fig. 42). The effect of encapsulating component seems to dominate the further increase of the system impedance at longer implanted time.

Hemocyte usually plays the role in immunity in arthropods. It participates in coagulation by nodule formation and encapsulation of foreign objects. Recognizable nodule formation can be found 24 hours after the injection of foreign object [164, 165]. Continuous aggregation of hemocytes attached to the inner layer of granular hemocytes to form concentric layers surrounding the object. This multiple layer can also contribute to the alteration of charge transfer in the interface of electrode. The non-linear Nyquist plot shown in fig 38(a) can be explained by such phenomenon. In addition, the melanization of the encapsulation can be found after multiple layers were formed [166]. Such behavior was also found throughout all surfaces of electrodes which had been implanted more than 24 hours. In some cases, hemocytes contain detoxicating enzymes to defend against the invasion [145]. This release of enzymes can also affect the electrical properties of the encapsulation.

During the electrical stimulation, it is possible that the electrophoresis caused the migration of protein and molecules toward the electrodes. Closed-paired of electrodes were used as the implant in this study. If the encapsulation were formed due to the electrophoresis, this behavior should be found remarkably on one end of the electrode due to the polarized membrane of protein. In this study, the encapsulation was found on the surface for both working and the ground wire (fig 43). The cellular event was also

demonstrated on the electrode surface in epifluorescence images. Therefore, the biological interaction is mainly associated with encapsulating hemocyte.

Summary

This chapter investigated the interfacial interaction of electrode-bio system. Electrical Impedance Spectroscopy was conducted to assess the change of electrical property of implanted electrode in the neural system of American cockroaches. Systematic increase in impedance against time was observed. The increasing rate in impedance magnitude at 1 KHz was 2 orders higher after 24 hours than that for the first 16 hours.

Two mechanisms affecting the impedance of the interface were proposed. First is the formation of silver oxide. The other is the immuno-response of tissue encapsulation. XPS results identified the characteristic of silver oxide. The deconvoluted result of XPS spectra showed the presence of multiple oxygen state at the interface.

Histological results suggested that the biological interaction is due to the hemocyte (blood cell) encapsulation. The results also correspond to the measured impedance value in which higher cell density cause higher impedance magnitude. Cellular encapsulation dominates the enormous increase of the impedance value for longer implanted time.

Results in the Nyquist plots suggested the alteration of charge transport pathway. The effect of the increment in encapsulating component shapes the non-linear and the semi-circle arc at high frequencies area in the Nyquist plot.

CHAPTER V

SURFACE MODIFICATION OF ELECTRODE USING GRAPHENE

In order to extend the life spam of neural implant, surface modification of electrodes was investigated. This chapter discusses methods of modification and then confirmation of graphene structure on the electrode. The properties and performance of electrodes were characterized using EIS and AFM techniques. Finally, a modified Randle model was developed in order to understand the effect of current on potential.

Structural identification of graphene

Raman spectroscopy was performed at Material Characterization Facility of Texas A&M University. The graphene layers were made using exfoliating the graphite rod and were transferred to the polished silicon wafer. Raman spectroscopy was performed to measure the rotational mode of flakes found on the silicon wafer after the exfoliating process to identify the structure.

The Raman (HORIBA Jobin-Yvon LabRam system) analysis was conducted with laser excitation wavelength of 632nm. The detecting range for Raman shift is from 100-3000 cm^{-1}. During the measurement, the size of the area where the signal was collected is related to the diameter of the pinhole and the magnification of objective lens. In this study, 50X objective coupled with 200 micron pinhole were used. It provided the projected area 20 micron meters in diameter. In addition, the iris of the pinhole is actually a square; i.e. 20 micron meters in diameter should be adjusted to 20 micron meters in diagonal. Figure 46 shows the image of a graphene flake under the optical

microscope. The red dot is the center of the incident laser. The square with dash line is the area where the signals were collected. Figure 47shows the optical images of another spot where the Raman shift was measured. Similar to figure 46, the red dot in fig. 47 is the center of the incident laser where the square refers to the area of signal collection.
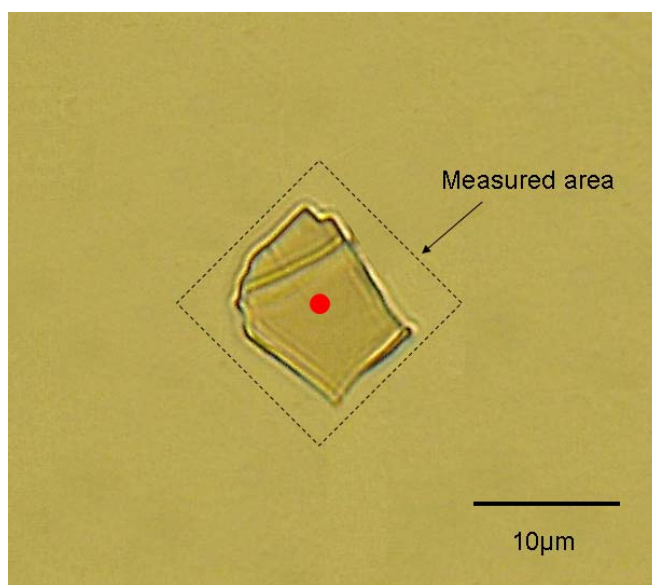
Figure 46. Optical image of a graphene flake. The red dot is the center of incident laser, and the square with dash line is the area where the signals were collected.
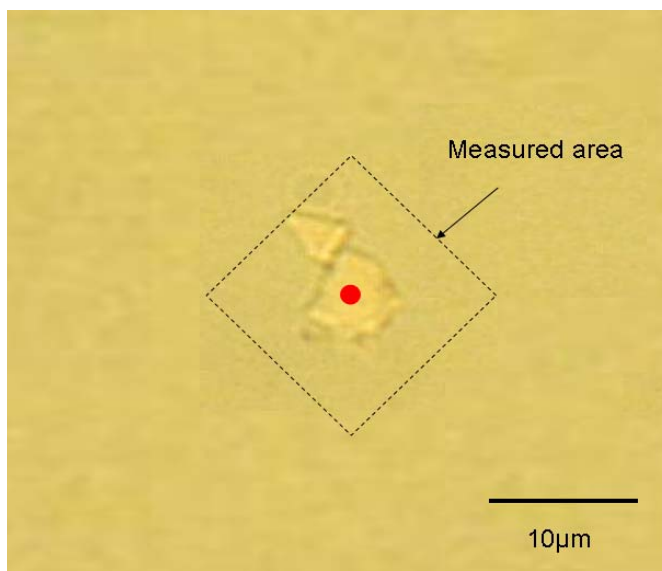
Figure 47. Optical image of graphene flake. The red dot is the center of
incident laser, and the square with dash line indicates the area where
the signal were collected

The full ranged spectroscopic results of Raman shift is shown in figure 48. The strongest signal located at 520 cm^{-1} refers to the silicon where the signals at 1580 cm^{-1} and 2700 cm^{-1} refer to graphene. It is noted that the intensity of peak referred to silicon is much stronger than the rest of the peaks. This is mainly due to the small amount of graphene under the exposure area. To clearly identify the Raman shift of graphene structure, smaller scanning range (1200~3000 cm^{-1}) of measurement was made and the results are shown in figure 49.
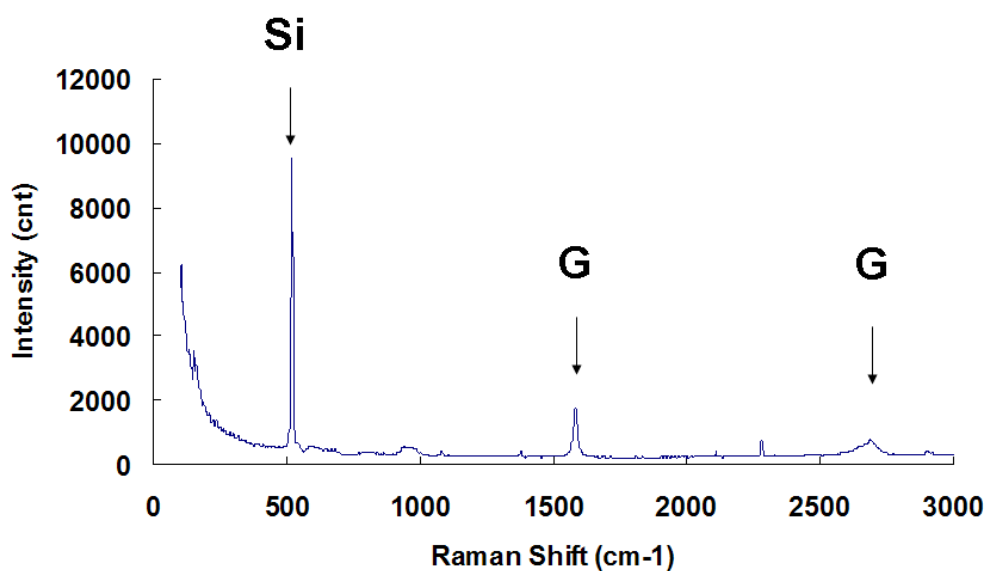
Figure 48. Result of Raman shift of full range scan.

In figure 49, the upper spectrum indicates the results obtained from the graphene flake shown in fig.46, and the middle spectrum was obtained from the graphene flake shown in fig.47. The peak exhibited at ~1580 cm^{-1} is referred to the G band of graphene where the peak exhibited at ~2680 cm^{-1} is referred to the 2D band of graphene. These two are the characteristic peaks for graphene [152, 153]. The G band is the first order optical vibration mode of the carbon atoms in graphene. It related to the doubly degenerate zone center (E_{2g}), in which the motions of the atoms along the Brillouin zone are restricted due to the symmetric structure. The energy difference between two E_{2g} modes is small thus appears as single band [167-169]. The 2D band is the second-order spectrum of graphene, which related to the second order of phonons of Brillouin zone boundary.

For the single layer of graphene, the ratio of peak intensity between G band and 2D band is roughly 1:4 [153, 169]. The relative intensity of 2D band to the G band significantly reduces and the band width of 2D band increases when the number of graphene layers is further increased. [168, 169]. The results shown in fig 49 suggested that the coating materials used in this study were multiple layers of graphene. Notable difference of relative intensity between G band and 2D band in upper spectrum (ML) and the middle spectrum (M'L) shown in fig.49 is also observed. This can refer to the different thickness or number of layers of graphene between two scanned samples.

In fig49a, and fig. 49b , other peaks except G and 2D band were also found. The additional characteristic peaks corresponded to the vibrational mode of silicon. The result of the Raman shift, in which the scan was conducted on the pure silicon substrate, is shown in the fig.49c. Compared with the fig.49a and fig.49c, no other substance or contamination was found on the substrate. These results suggest that only multiple layers of graphene were transferred to the electrode from the silicon substrate.
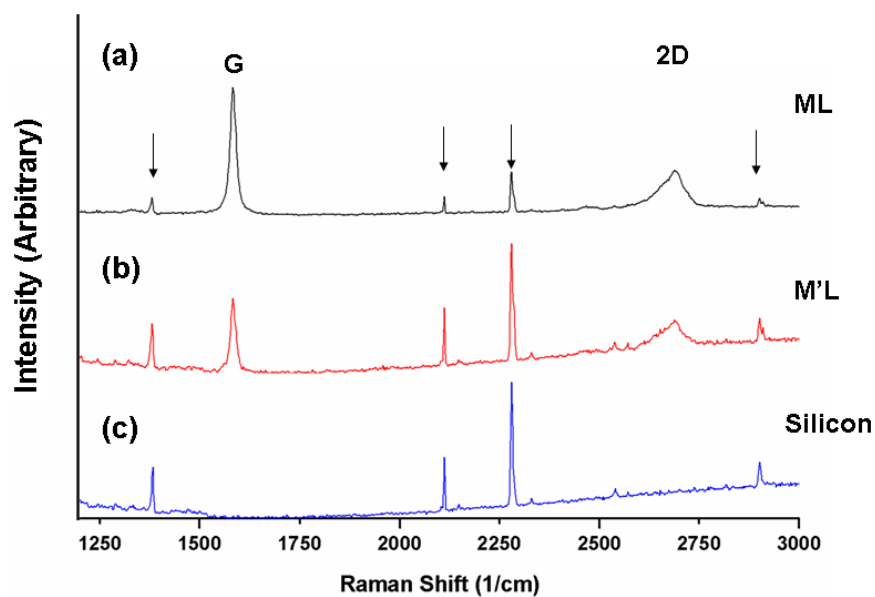
Figure 49. Raman shift of graphene structure. Fig. 49(a) and fig. 49(b) represents the results obtained from the graphene shown in fig.46, and 47, respectively. The spectrum of bottom layer is the scanning result of plane silicon substrate.

Effect of graphene on interface

As described in chapter3, all EIS experiments were conducted in 0.9 wt% of NaCl solution. The measured frequency ranged from 0.1Hz to 100 kHz under a constant voltage mode. The sinusoidal perturbation voltage was preset at 10 mV.

The Bode plots of the impedance measurement are shown in figure 50. It presents the phase change across frequency range at different implanted time for electrodes with no graphene coating. Each data represents the mean value over 10 experiments, where the error bar represents the standard deviation. In figure 50, two relaxation processes are observed. As indicated in the figure, one occurs at around 100 KHz and the other occurs at 10 Hz. The spectrum of 0 hour implanted electrode only

shows one relaxation phenomenon at high frequency. The second relaxation process at

10 Hz thus indicates the presence of another charge transfer process occurring at the

interface. In addition, decrease in phase angle of this peak is also observed.
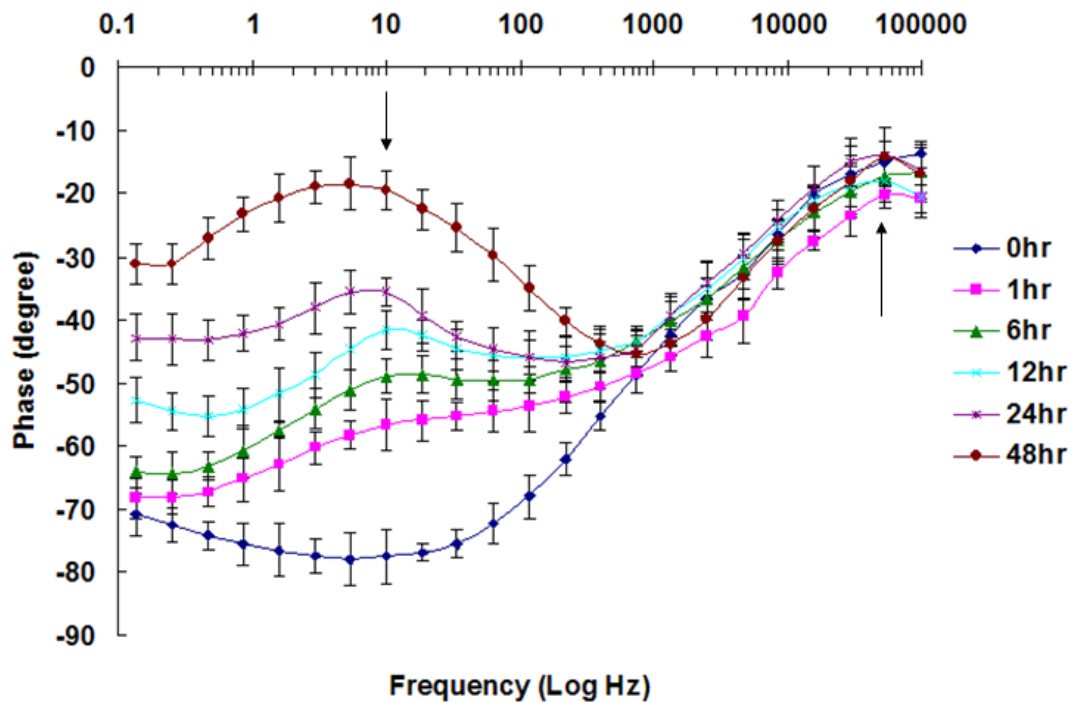
Figure 50. Bode plots of impedance measurement for electrode with no
graphene coating. It presents the phase change across the measured
frequency range against implanted time. The arrows indicate the
relaxation phenomenon.

Figure 51 shows the Bode plots of impedance measurement for electrodes coated

with graphene at different implanted time. Each data points represent the mean value

over 10 experimental results, where the error bar represents the standard deviation.

Similar to the results shown in figure 51, two relaxation phenomena are observed.

However, the relaxation process at 10 Hz does not appear at 1 hour implanted time.

Noticeable relaxation phenomenon at such frequency range exhibits at 6 hours implanted

91

time. In addition, the decrease of the phase angle at this peak in this figure is not as conspicuous as it is shown in figure 50.
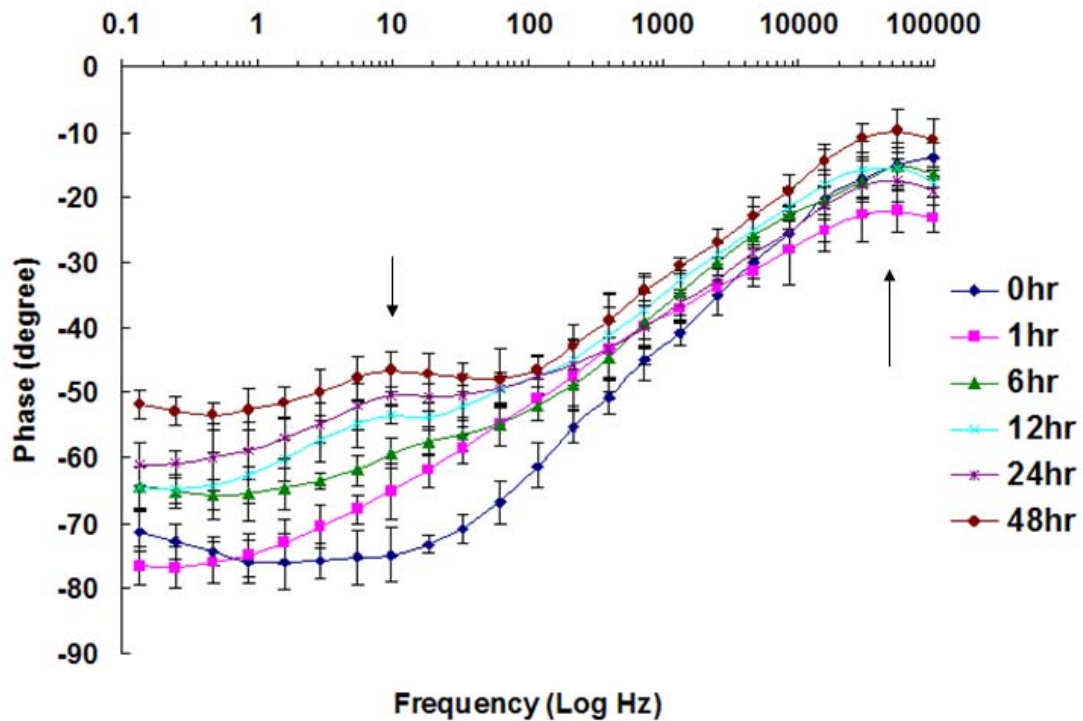
Figure 51. Bode plots of impedance measurement for electrodes coated
with graphene. It shows the phase change across the frequency range
against implanted time. The arrows indicate the relaxation phenomenon.

As mentioned in the chapter 3, the fundamental theory of EIS measurement relies on the response of the system to the perturbation voltage. The excitation signal (eq. 12) passed through the interface, which derived a responding current (eq. 13) with a shift in phase.

$$E_t = E_0 \sin(\omega t) \tag{12}$$

$$I_t = I_0 \sin(\omega t + \phi) \tag{13}$$

The change of dielectric constant at the interface will alter the electrical

properties. Such change leads to the momentary delay of the responding current, which

is referred as interfacial relaxation phenomenon. Relaxation phenomenon usually results

in a peak of phase angle in Bode plot. It has been reported that the relaxation

phenomenon can be used as an indication of the new forming components or charge

transfer at the interface in different materials or coatings [170-173]. In the electrode-bio

system, the encapsulating tissue surrounding the electrode is considered as one

component at interface. The presence of this component alters the charge transfer of

interface in EIS measurement which results in relaxation phenomenon. The peak shown

in figure 50 and 51 at 10 Hz can refer to the existence of the encapsulating tissue.

As discussed in chapter 4 the formation of encapsulating tissue is a dynamic

process. The hemocyte adhered to the electrode surface that gradually decreased the

resistive pathway. It's observed that the phase angle of the peak at 10 Hz shown in figure

51 decreases as the increase in implanted time. Such observation can be used to correlate

with the increase of impedance in the tissue layer. In addition, the maximum phase angle

of the peak shown at 10 Hz in figure 50 is much higher than that shown in figure 51.

This indicates that under the same implanted time, the electrode coated with graphene

exhibits lower impedance in tissue component than that of the electrode without

graphene coating.

Effects of graphene on charge transfer

In the result of Nyquist plot in EIS measurement, it shows the relation between the Real and Imaginary pair of impedance. The shape of the Nquist locus usually can be used to determine the behavior of charge transfer at the interface. Figure 52a shows the impedance spectra of electrodes with no graphene coating at different implanted time. Figure 52b highlights the high frequency range (marked area) of Nyquist loci in fig. 52a. In fig.52a, noticeable non-linear behavior of Nyquist loci which indicates the R-C effect is observed. The variability of real component of impedance spectra gradually increase as increase in implanted time. At 48 hours, the nonlinearity of the impedance spectra manifests itself to show an apparent semi-circle arc followed by a quasi-vertical. Such behavior and the influence of R-C effect have been discussed in previous chapter. The R-C effect can be used to represent the alteration of charge transfer at the interface due to the existence of encapsulating tissue.
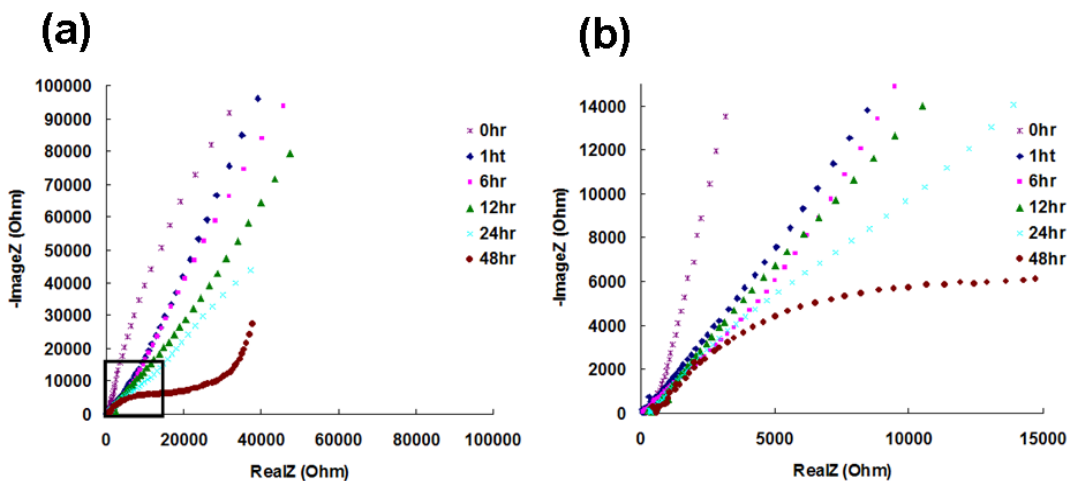
Figure 52. (a) Nyquist plot of electrode without graphene coating at different implanted time. (b) Highlight of high frequency range of Nyquist loci shown in fig. 52a.

Figure 53a shows the impedance spectra of electrodes coated with graphene at different implanted time where figure 53b highlights the marked area of figure 53a. R-C effect can also be found at this condition. However, it seems the variability of R components shown in figure 53 is less significant than that shown in figure 52.
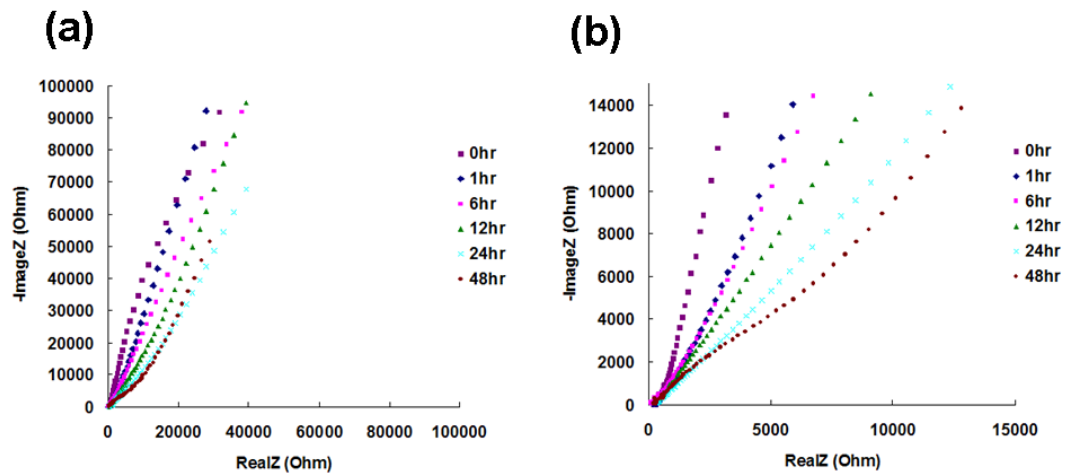
Figure 53. (a) Nyquist plot of electrode coated with graphene at different implanted time. (b) Highlight of high frequency range of Nyquist loci shown in fig. 53a.

To evaluate the influence of graphene to the charge transfer in the electrode-bio interface, here we compare the Nyquist loci of different electrodes at the same implanted time (fig. 54). In this figure (both (a) and (b)), the control group show obvious R-C effect which results in larger R-C arc at higher frequency range than the graphene coated electrode. This suggests that the tissue component forming on the interface in two types of electrode has different electrical characteristics. According to the histological results discussed in previous chapter (ch4), progressive immuno-response results in higher density of encapsulating hemocyte on the surface of electrode. This will change the

dielectric dispersion and the behavior of charge transfer at the interface. In addition, the increase of cell density corresponds to the evolvement of Nyquist loci (R-C behavior) which lead to the increase in impedance. Therefore, the significant R-C arc (marked area) found in the control group shown in figure 54 can refer to the extensive reaction of encapsulation.
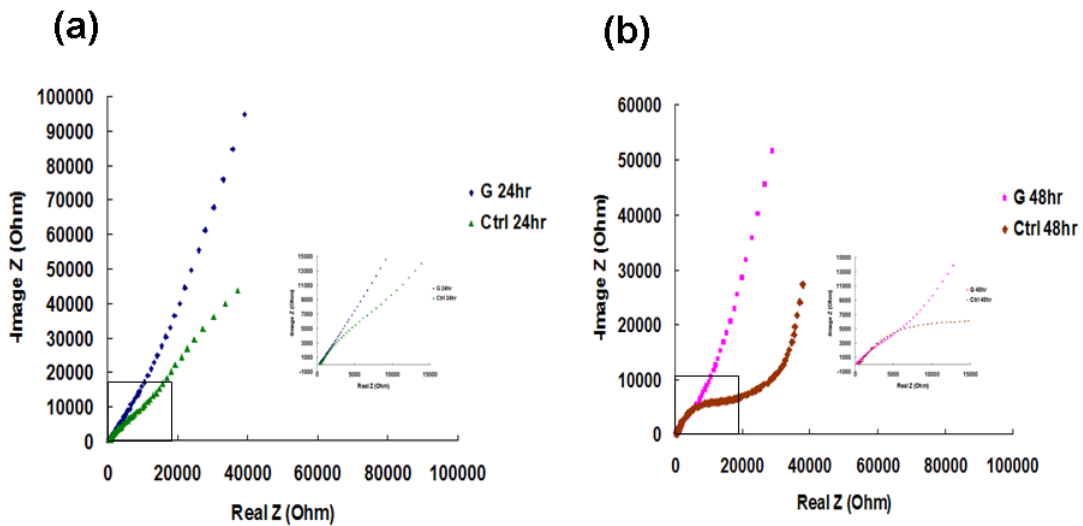
Figure 54. Nyquist loci of different electrodes at the same implanted
time. (a) 24 hour(b) 48hr

Throughout experiments for both control group and the graphene-coated electrodes, systematical change in impedance spectrum is observed (fig. 53 and 54). The R-C arc in Nyquist plot gradually developed and become more pronounced over the duration of the implant. To further clarify the influence of graphene to the development of the R-C behavior, all the impedance spectra were plotted together as the function of time. Figure 55 shows the impedance loci of both control group and the experimental group throughout the entire implanted time. The spectra of control group (blue dot)

exhibit higher increase in the R components than the coated electrodes (red dot) at each

duration of implant. Among all the impedance spectra, the control group shows apparent

R-C arc than the electrode coated with graphene at every implanted time. The less

pronounced R-C effect, the less alteration of charge transfer. As discussed in previous

chapter, the alteration of charge transfer directly associates with the development of

encapsulating tissue. Based on the results of impedance loci, it is believed that the

graphene coating strongly delayed the process of encapsulation. The graphene coating

exhibits biocompatibity which reduces the extensive reaction of immuno-response.
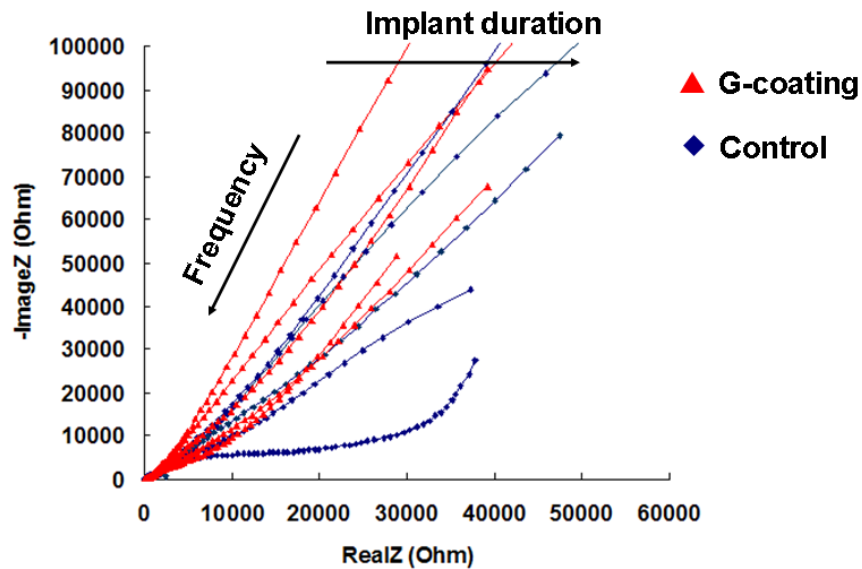
Figure 55. Nyquist plot for two different electrodes. The group of red
dot is the electrodes with graphene coating, where the blue ones are the
control group.

Electrical signal responses of graphene

Figure 56 shows the AFM image of graphene and the adjacent copper wafer. The thickness of the examined graphene is 200nm. The blue and green rectangular are the scanned area of copper and graphene, respectively.
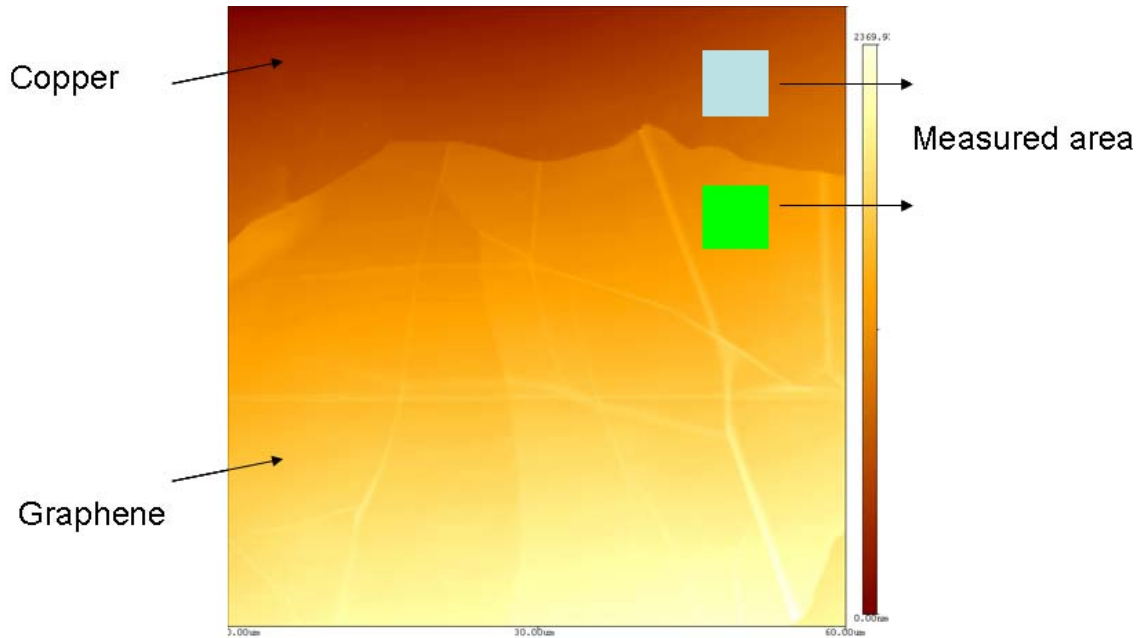
Figure 56. AFM images of graphene on the copper wafer

As describe in chapter 3, a constant potential was applied to the AFM probe during the process of image acquisition while the responding current was obtained by a Pico-meter. The results of responding current of copper and graphene under different potential are shown in figure. 57. The data is the mean value obtained by 150 experiments, and the error bar is the standard deviation. In both case of copper and graphene, the current output shows linear increasing trend corresponding to the increase in applied potential. This linear trend indicates the measured system is stable that follows the Ohm's law. It is noticed that the current output obtained from graphene is 3

orders higher than that from the copper. It has been reported that the vibration of

graphene atom at room temperature results in electrical resistivity of 1 micro ohm-cm

[174], which is 42% less than the copper. Previous spectroscopic study showed that the

native copper oxide immediately forms within an hour while exposed in the ambient

environment at room temperature [175]. The 3 order differences in magnitude of output

current shown in figure 57 thus can be ascribed to the growth of the copper oxide. The

results shown in this figure indicate that the graphene can be used as a protecting layer to

prevent from the oxidation of electrode.
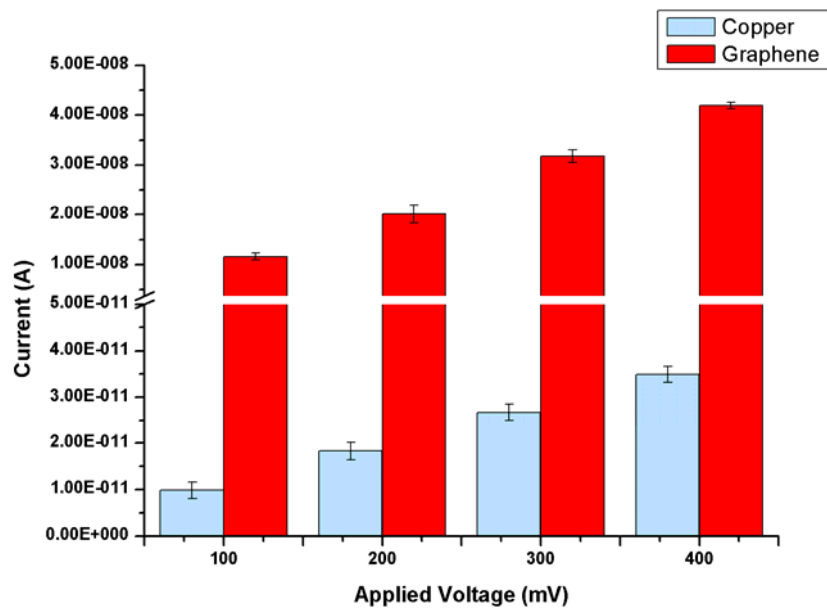
Figure 57. Current responses of graphene and copper.

To further investigate the effect of graphene coating to the metal oxidation, the

electrical potential was applied to the same area shown in fig. 56 on copper and

graphene, respectively. This was done at 1hr, 2hr, 5hr and 9hr while the sample was

continuously exposed to the ambient environment. Figure 58 shows the current responds corresponding to the potential applied to the copper against time. The fitting curves were done using ExpDec1 model (Origin 8). The parameters of the fitting results are summarized in table 10. It is noticed that the current response drops dramatically at the first hour and tend to reach an asymptotic value afterward.
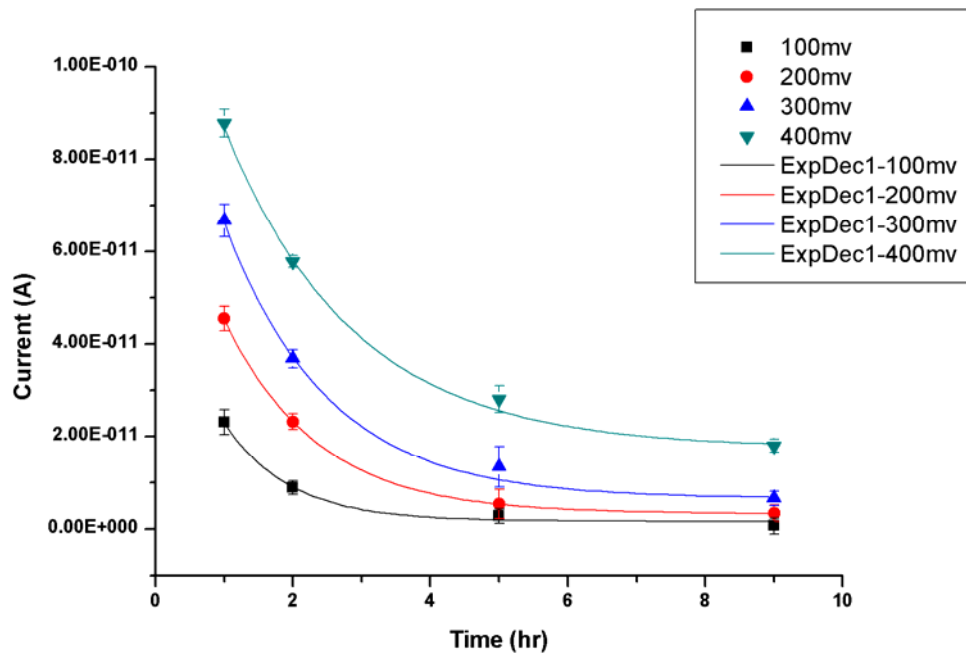
Figure 58. Current response from copper against time.

Table 10. Summary of the fitting results shown in figure 58. The fitting formula used here is expressed as $y = A\exp(\dfrac{-x}{t}) + y_0$.

Input Voltage	A	t	Y_0	R^2
100mv	6.13E-11	0.947	1.58E-12	0.9723
200mv	8.97E-11	1.329	3.22E-12	099782
300mv	1.17E-10	1.485	6.52E-12	0.99562
400mv	1.18E-10	1.869	1.73E-11	0.99556

In a linear DC system, the current response is proportional to the inverse of resistance of the material (Ohm's law). According to the Pouillet's law (eq 14), the electrical resistance of the material is proportional to the distance (length) of where the current travels across. In addition, it has been reported that the growth of the native copper oxide follows the inverse-logarithmic growth rate law (eq 15) [175] In equation 15, d is the thickness of the oxide film, t is the exposure time, and A (0.4040) and B (-0.0271) are constants.

$$R = \rho\frac{l}{A} \tag{14}$$

where R represents resistance, l is traveling distance, ρ is resistivity, and A is the area of material.

$$\frac{1}{d} = A - B\ln t \tag{15}$$

Figure 59 represents the inverse of thickness of native oxide (1/d) as the function of time. The data was obtained using the equation 15 by plugging in the parameter of time from 0hr to 9hr. The fitting curve shown in this figure was generated using

ExpDec1 model (Origin 8). The fitting results are summarized in table 11. The output

current shown in fig. 58 and the inverse of copper oxide thickness shown in fig.59 both

fit the same equation of exponentially decay. This indicates that the current drop is

correlated to the growth of copper oxide. The output current is thus believed to be

proportional to the thickness of copper oxide, which can be expressed in equation 16.
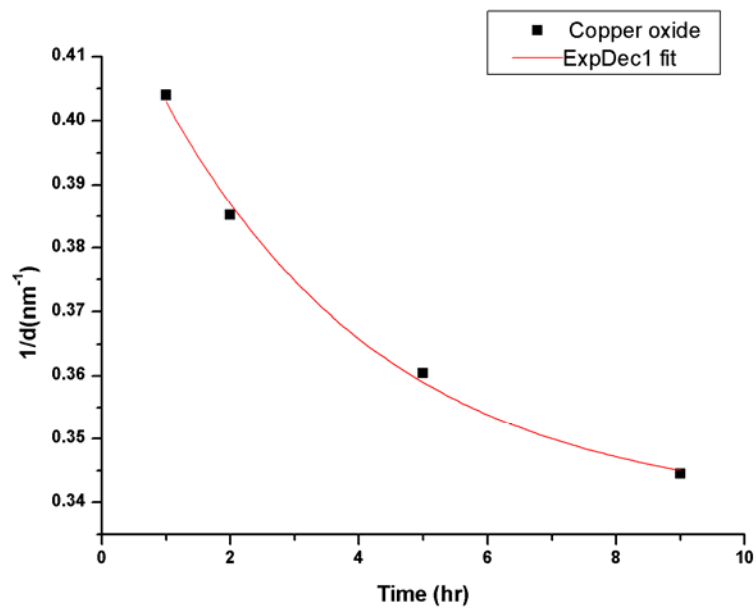
Figure 59. Dependence of the inverse oxide layer thickness..

Table 11. Summary of the fitting results shown in figure 76.

Formula (ExpDec1)	A	t	Y_0	R^2
$y = A\exp(\dfrac{-x}{t}) + y_0$	0.086	3.47	0.3385	0.99113

$$I\alpha\frac{1}{d} = A - B\ln t \qquad (16)$$

Figure 60 shows the current response of the graphene corresponding to different applied potential against exposure time. It is noted that the current drop throughout 9 hours exposure to the ambient environment is ignorable. Compared the results in fig 58 with fig.60, it is observed that the current drop within 9 hours of copper is $87\%\pm7\%$, where there is not significant current drop ($5\%\pm3\%$) of graphene. As discussed in previous chapter, the biological environment chemically interacted with the metal electrode by forming the metal oxide, which resulted in the increase in interfacial impedance of the electrode. The results shown here indicate that the graphene not only served as a stable medium for electrical signal transportation, but also prevented the substrate from being oxidized. This suggests that the graphene has a great advantage for being used in neural implant.
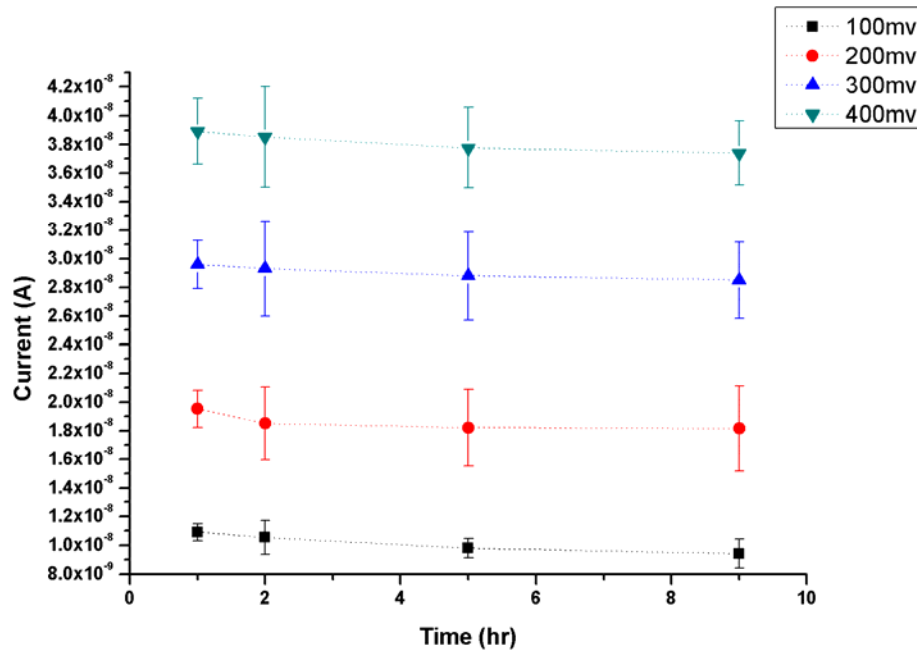
Figure 60. Current response of Graphene against time

Summary

In this chapter, effects of the graphene on bio-interaction were investigated. Graphene was obtained using exfoliating graphite rod and were transferred to the implant. EIS was conducted to monitor and evaluate the interfacial interaction between the implanted electrodes in the neural system of American cockroaches at different implanted time. Electrical response of graphene and its behavior of anti-oxidation were also investigated using AFM measurement.

Relaxation phenomenon found at 10 Hz in Bode plot suggested the formation of encapsulating tissue at the interface. Such relaxation process can be attributed to the

presence of encapsulating tissue. The decrease in phase angle of relaxation phenomenon can be used to describe different level of cellular encapsulation.

The R-C arc shown in the Nyquist plot was used to detect charge transport. Result in the Nyquist loci suggested that the process of alteration in charge transport pathway was slower for the implanted electrode coated with graphene.

Experimental results shown in this chapter suggested that the graphene has great potential in the application of neural implant. It not only provides good electrical conductivity for signal transport, prevent the substrate from oxidation, but also reduce the speed of the accumulation of tissue around the electrode. Such characteristics of graphene can significantly increase the life span of neural implants.

CHAPTER VI

MODELING AND ANALYSIS OF BIO-INTERFACES[*]

This chapter discusses modeling of electrode-bio interface and mechanisms of interaction. First of all, the procedures to establish a theoretical model were discussed. The dynamic process of bio-interaction was also described. A physical and mathematical model is developed in order to describe the interfacial interactions between an implant material and the neuron. Such model can be used to evaluate the electrical behavior of the electrode-bio interface. Information obtained by the model is useful for calibration of electrical signal acquisition and stimulation in neural implant. The model is useful for materials selection and design as electrodes.

Equivalent circuit model of electrode-bio interface

Equivalent circuit is a theoretical circuit of the system, which includes the electrical characteristics of all elements in the circuitry. The equivalent circuit models are usually used to approximate the linear or non-linear behavior of the complex circuit. Each element in the model can be used to represent the physical model in the complex system. This approach is important to evaluate the electrical effect of each element to the system.

---

[*] Part of this chapter is reprinted with permission from "Electrode-immune system interface monitor through neural stimulation in American cockroach (*Periplaneta americana*) by Cheng-Wei Chiu, Jorge M. Gonzalez, Mark Harlow, S. Bradleigh Vinson, Hong Liang, Electrochimica Acta, 68, 81-87, Copyright (2012) by Elsevier.

Modeling procedure

To establish the equivalent circuit model in a complex interface, an educated postulation is necessary. This postulation requires the knowledge of the interfacial constitution and the modeling representation for each component. In this study, the effects of substrate and tissue encapsulation layer are two main components at the interface. In addition, an important component in general metal-electrolyte interface is the double layer. In this section, each component in the modeled circuit and the electrical representation will be discussed.

Circuit model for double layer

A double layer is usually used to describe the charged surface in ionic environment. It is known to exist in all kind of interface between two materials (or phases). The formation of this double layer is due to the electrical polarization of the charge across the interface between two materials. Holmholtz firstly proposed this double layer as a model of charge separation in 1879 [176]. Figure 61 shows the conceptual double layer in metal-electrolyte interface.

Imaginary capacitor plate
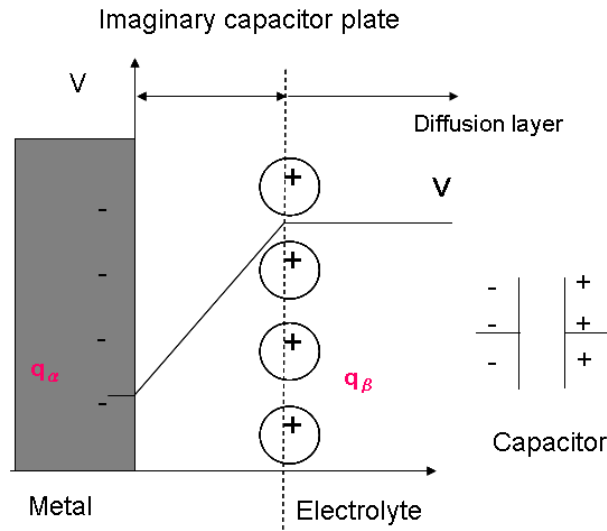
Figure 61. Conceptual diagram of double layer in metal-electrolyte
interface. q_α and q_β represent the excess charge.

In an equilibrium state of a metal-electrolyte system, excess charge presents in

both side of the interface, at which creates an imaginary plate. The magnitudes of the

excess charges are the same and opposite in sign. This imaginary plate can be seen as a

capacitor due to the charge separation, and its capacitance is expressed as equation 17. A

potential gradient (fig 61) in this imaginary plate is produced by this charge separation.

$$C = \frac{q_\alpha}{V} \tag{17}$$

In Helmhotz's theory, a double layer can be divided into Helmholtz inner plane

and Helmholtz outer plane (fig. 62a). In the inner plane, the dipolar water molecules

align their orientation as determined by the excess charge in the metal. The outer plane is

defined by the center of the aligned positive charges. Each plane has different linear

108

potential gradient determined by different mathematical equations (fig.62b), as listed in

equation 18 (outer plane) and 19 (inner plane).

$$V_{out} = \frac{qd}{\varepsilon_r \varepsilon_0} \qquad (18)$$

In this equation, q is the excess charge, d is distance shown in figure 62. ε_r is

the dielectric constant. ε_0 is the permittivity of a vacuum $(8.85 x 10^{-12} Fm^{-1})$

$$V_{in} = \frac{\mu N}{\varepsilon_r \varepsilon_0} \qquad (19)$$

In this equation, N represents the number of water molecules. μ is the dipole

moment of water (the value measured in the vapor phase is $6.2 x 10^{-30} Cm$
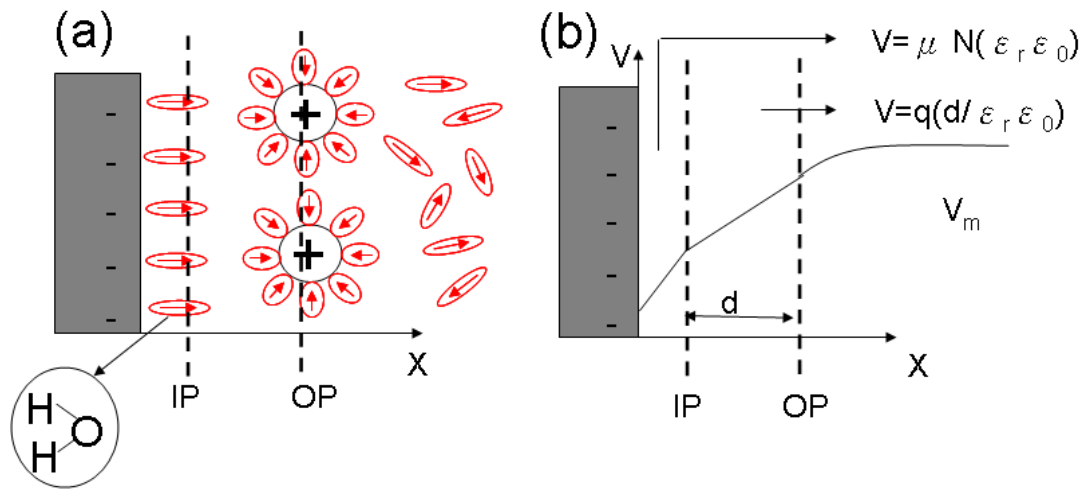
Figure 62. Conceptual diagram of Helmholtz inner and outer place. IP:
inner place. OP: Outer plane.

In the equivalent circuit mode, a double layer resembles a charged capacitor. In

addition, the system generated a sinusoidal potential, which produced a charge flow

passing through the interface during EIS measurement (fig 63). For each material, the

ability hiders the current passage is referred as electrical resistance. Therefore, a resistor

must also be a component in this circuit. Since both capacitance and the resistance affect

the electrical properties, they will be considered connected in parallel in the circuit.

Equivalent circuit model representing the double layer can be expressed in figure 64. In

this figure, R.E represents the resistance of electrolyte. Cd represents the double layer

capacitor, and Rd represents the resistance.
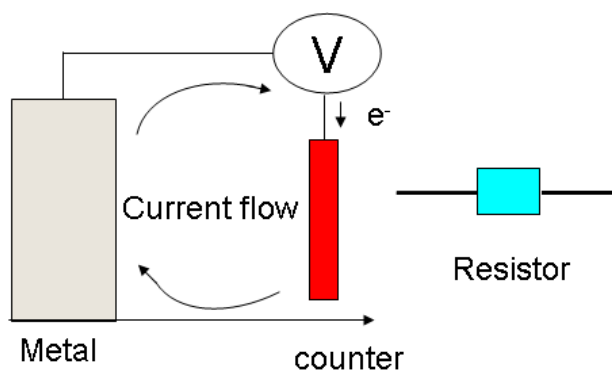
Figure 63. Voltaic cell of EIS experiment. The current generated by the
perturbation ac potential will pass through the interface, which create a
resistance in the interface.
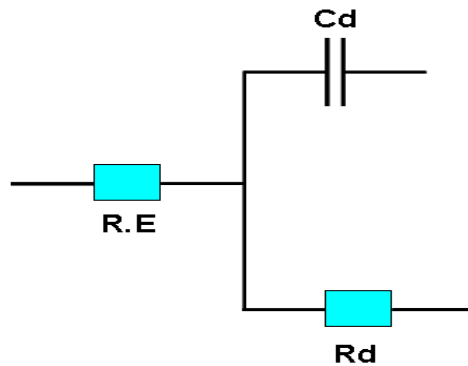
Figure 64. Representation of equivalent circuit model of double layer.

Circuit model for encapsulating tissue

Preliminary simulation result using the model described previously only shaped the high-frequency area of the Nyquist plot. The model is not sufficient to represent the entire system yet. As mentioned at the beginning of this section, the effect of encapsulating tissue should also be taken into consider. In the Nyquist plot shown in EIS result (fig. 38), non-linear spectra and semi-circle arc presents after longer implanted time. This indicates the effect of parallel R-C circuit in this region of the spectrum, which caused the alteration of charge transfer. According to the histological results, bio-interaction of encapsulating tissue contributed to this alteration. Therefore, the initial equivalent circuit model of this component can be expressed in figure 65.
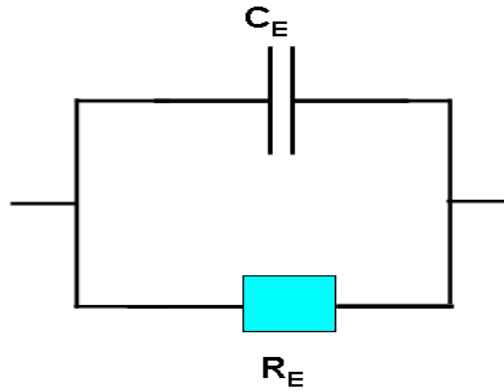
Figure 65. Initial equivalent circuit model of encapsulating tissue.

In the component of encapsulating tissue, the charge transfer is based on the ion diffusion. The impedance created by the diffusion is referred as Warburg impedance [177]. Warburg impedance is commonly used for semi-infinite linear diffusion in the system. The mathematical expression of Warburg impedance shows the dependence of frequency. (eq 20)

$$Z_w = \sigma(\omega)^{-\frac{1}{2}}(1-j) \qquad (20)$$

σ is the Warburg coefficient and ω is the frequency.

The effect of Warburg impedance is particularly higher in the low frequency range, and its phase angle is $\pi/4$. Therefore, Warburg impedance was introduced into the circuit model to represent the diffusional mechanism and shape the linear line at low frequency range of Nyquist plot (fig.38).

112

Moreover, the formation of non-homogeneous tissue layer was expected during the process of encapsulation. The epifluorescence image shown in figure 39 confirms the irregular surface of the encapsulating tissue. The effect of irregular surface can be compensated by a Constant Phase Element (CPE). CPE is a term used to describe the effect of pronounced surface roughness or non-uniform current distribution [178]. Its mathematical term can be expressed in equation 21. When the value of α is close to 1, CPE is equivalent to a perfect capacitor. In the real case, the value of α is between 0 and 1.

$$Z_{CPE} = \frac{1}{A_0 (j\omega)^{\alpha}} \tag{21.}$$

A_0 is the capacitance, ω is the frequency, $0 < \alpha < 1$.

Therefore, CPE was employed to replace the capacitor shown in figure 65. The effect of diffusion and pronounced surface roughness is illustrated in figure 66 a. The final equivalent circuit model representing the encapsulating tissue is shown in figure 66b.
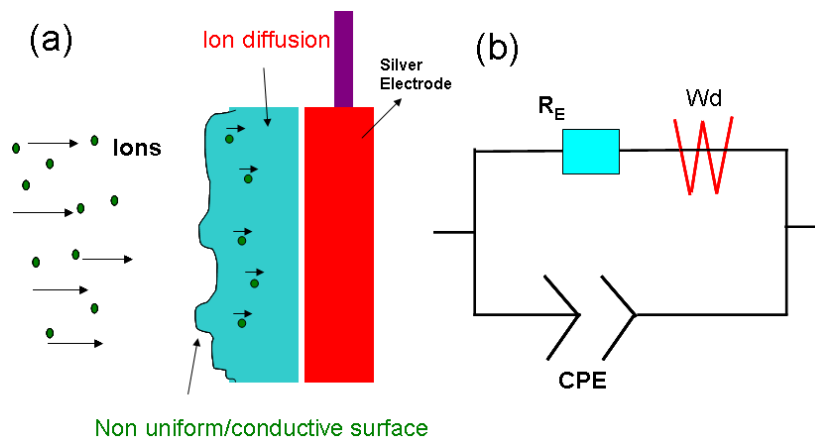
Figure 66. Equivalent circuit model of tissue encapsulation. (a) Illustration of the effect of diffusion and non-uniform surface. (b) the final circuit model representing the tissue encapsulation layer. R_E is the resistor. Wd is the Warburg Impedance. CPE is the constant phase element.

Circuit model for silver oxide

XPS results as shown in figure 39 confirmed the existence of silver oxide on electrode surface due to the chemical reaction between implanted electrode and hemolymph of cockroach.

In the circuit system, capacitor is an energy storage parameter in an electric field which also relates the charge separation across the same. It usually contains the non-conductive region between two conductors. The capacitance C of a capacitor can be expressed in equation 22. The materials used as a capacitor in electronic circuit usually have high dielectric constant.

$$C = \varepsilon_r \varepsilon_0 \frac{A}{d} \tag{22}$$

ε_r is the relative static permittivity (dielectric constant), ε_0 is electric constant ($8.854x10^{-12}\,Fm^{-1}$), d is the distance of the capacitor.

In application of semiconductors, silicon dioxide is widely used as a capacitor in Metal-Oxide-Semiconductor-Field-Effect-Transistor (MOSFET). The dielectric constant of silicon dioxide is around 4.6 where the dielectric constant of silver oxide is 8.8 [179]. In this study, the silver oxide layer located in between the silver electrode and the tissue encapsulating layer (fig. 66a). This is the concept of a capacitor where a material with high dielectric constant resides between two conductors. Representation of silver oxide in the equilibrium circuit model can be thus expressed as capacitor (fig.67).
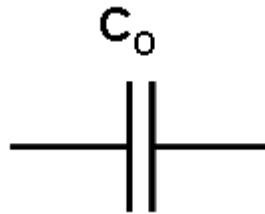
Figure 67. Equivalent circuit model of silver oxide. Co represents a charged capacitor

Model validity and simulation results

Circuit model

We proceed using empirical data to confirm the validity of the equivalent circuit model that was discussed in the previous section. To complete the equivalent circuit, each circuit component can be combined through either parallel or series. Based on the confocal image shown in figure 43, the silver implant is surrounded by the encapsulating tissue. The schematic illustration of measured interface of electrode in EIS cell can thus be shown as figure 68a. As discussed in the previous section (6.1.1.1), double layer exists in all kind of interface between two materials (or phases). In this study, the effect of charge separation is across the interface, which created a double layer capacitance (C_d). During the EIS measurement, the voltaic cell generated a charge transfer passing through the double layer based on the faradaic reaction. This effect is represented by a double layer resistance (R_d). In the modeled circuit, C_d and R_d should be thus combined in parallel.

In addition, the interface is constituted by encapsulating tissue and silver oxide (fig 68b). The circuit models, which represent these components, were described in previous sections. Based on the physical structure of interface shown in figure 68b, the effect of encapsulating tissue and silver oxide should be integrated in a serial combination. Moreover, the effect of double layer resistance (R_d) should also be combined with this serial combination in series. This is due to the charge transfer created by the faradaic reaction passed through the entire interface during the EIS measurement.

116

Finally, the complete circuit model used to represent the interface of electrode-bio system is shown in figure 69. In this model, the double layer capacitance (Cd) is connected in parallel with a serial combination of three electrical components
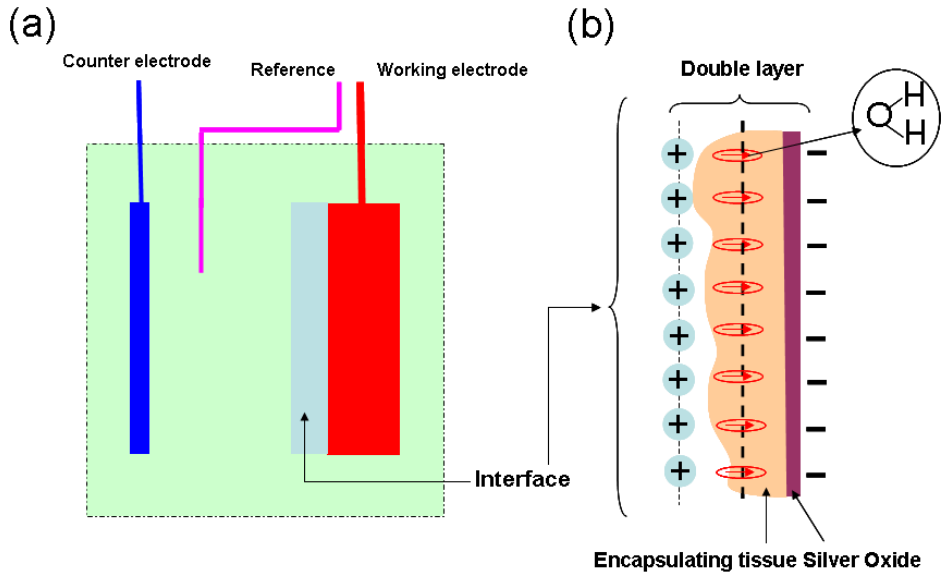
Figure 68. The schematic illustration of measured electrode in EIS cell.
(a) The measured interface in EIS cell. (b) Physical structure of
interface is composed by encapsulating tissue adjacent to silver oxide.
The effect of charge separation is across the interface.
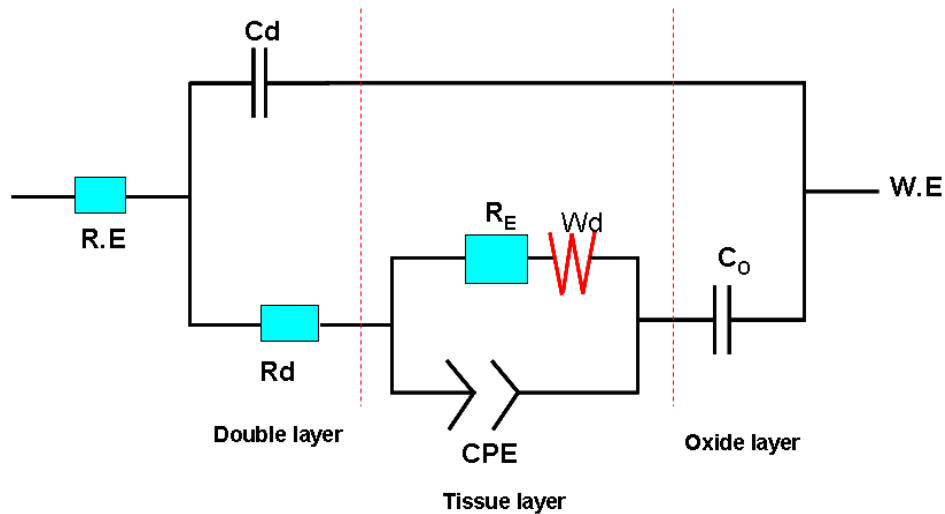
Figure 69. Equivalent circuit model of interface in electrode-bio system interface. Three elements were integrated to complete the circuit. W.E represents the working electrode.

In simulation, experimental data were used as input parameter. The initial value for each element was estimated from the drop, slops and the horizontal region shown in the Bode plot of impedance locus. Figure 70 shows the refined estimation, which was derived using Levenberg-Marguardt curve fitting mode through Gamry EIS 3000 software. In this figure, the measured impedance spectra of 48 hours implanted electrode versus the simulated spectra were plotted. The close match for both Bode plot (fig.70a) and Nyquist lot (fig. 70b) indicate the validity of the equivalent circuit model.
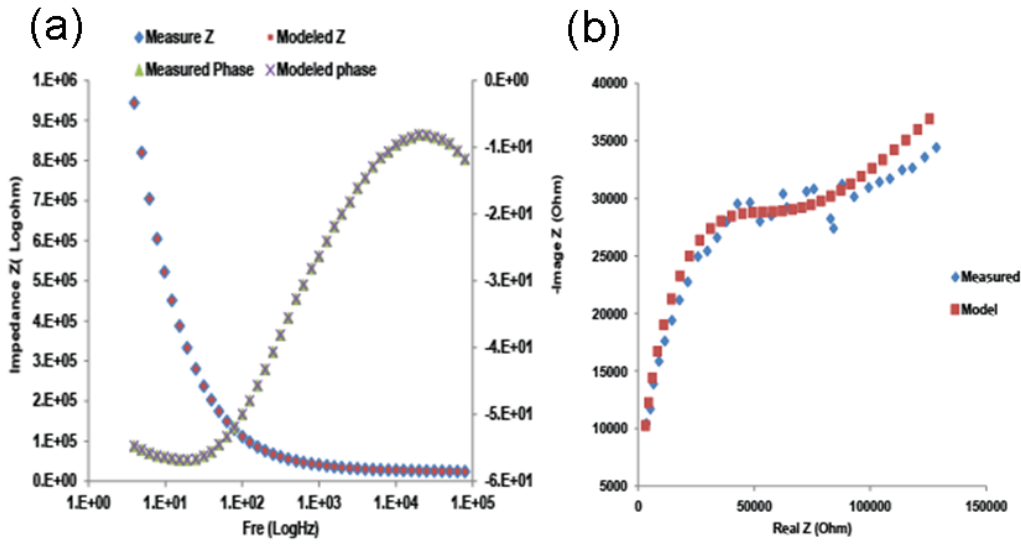
Figure 70. Simulation result of 48 hours imlanted time (a) Bold plot: Impedance magnitude. (b) Nyquist plot: Impedance locus

Validation using graphene electrode

In the interface of graphene electrode, the complex interface should include interfacial double layer, the component of encapsulating tissue, and the substrate. Since the graphene coating did not form a continuous film on the surface, it cannot be detected by the EIS system. Thus the circuit component of graphene can be excluded in the model.

The configurations of the circuitry in this study are essentially the same as were described in the previous subsection. A parallel R-C combination represents the interfacial double layer which is used to describe the charge separation coupled with Faradiac reaction at the contact plane of interface (fig.64). A modified parallel R-C combination represents the encapsulating tissue component (fig 66b). In this modified R-C model, Warburg impedance connected with a resistor in a serial combination. A

constant phase element used to replace the charged capacitor was connected with this serial combination in parallel. Such model can be used to describe the behavior of charge transfer in the tissue component with compensations of ionic diffusion and the effect of pronounced surface roughness.

The major difference of the system circuitry between graphene electrode and the silver electrode is the substrate. As discussed in 6.1.1.3, the substrate was silver and the silver oxide formed by chemical reaction can be represented by a charged capacitor (fig, 67). In the graphene electrode, high purity silver paint (SPI-paint UN#1123) was selected as the substrate. Such paint is the polymer base with high concentration of embedded silver particles. In electrochemical study, polymer is usually considered as a capacitor where the electrons or ions build up on its surface [180-182]. In addition, the silver particles, pores, voids in the polymer coating provided conductive pathway and spaces for charge transport. Therefore, the circuit model representing the substrate of silver paste exhibited a parallel R-C combination (fig.71). In this figure, Cs is the capacitance of the polymer coating where Rs is the resistance to charge transport in the polymer coating. With the same logic to interpret the physical model of the interface (fig.68), the complete equivalent circuit model of the complex interface thus can be shown in fig 72.
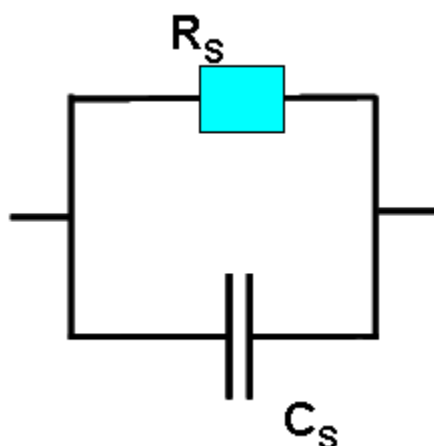
Figure 71. Circuit model used to represent the substrate of silver paste.
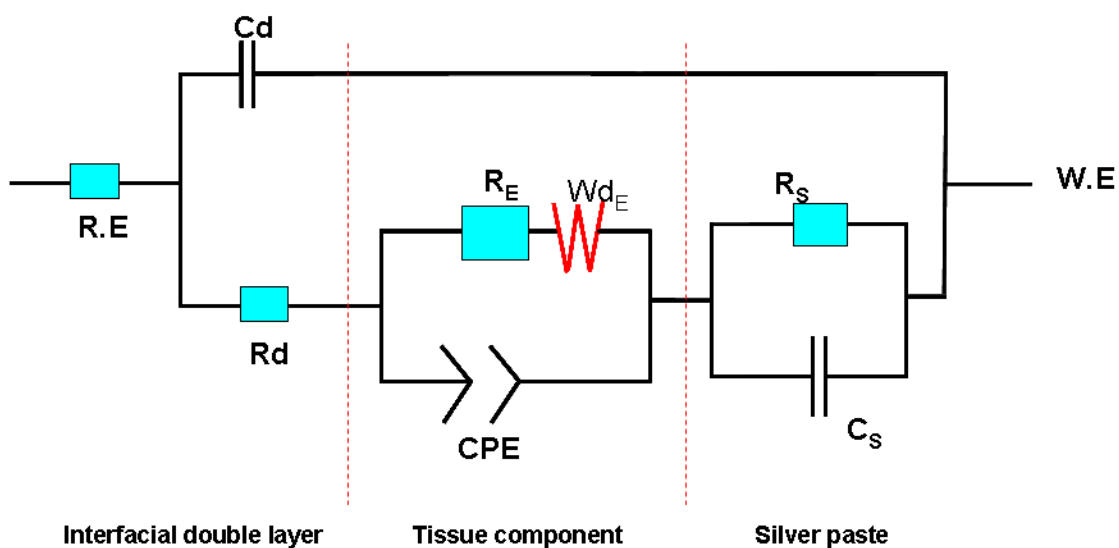
Figure 72. Complete equivalent circuit model. Each column represents
one component at the interface.

The equivalent circuit model used to represent the interface of graphene coated

electrode-bio system is established. The validity of the model will also be confirmed

using the Gamry EIS 3000 software. The results of refined simulation are shown in

figure 73. Figure 73a shows the experimental data of the electrode with graphene coating

for 48 hours implanted time versus simulated data for Bode plot. Figure 73b shows the results of experimental versus simulated data for Nyquist plot. The good-fitting index of 10^{-5} and the close match of spectra shown in figure 73 confirm the validity of physical model proposed in previous section.
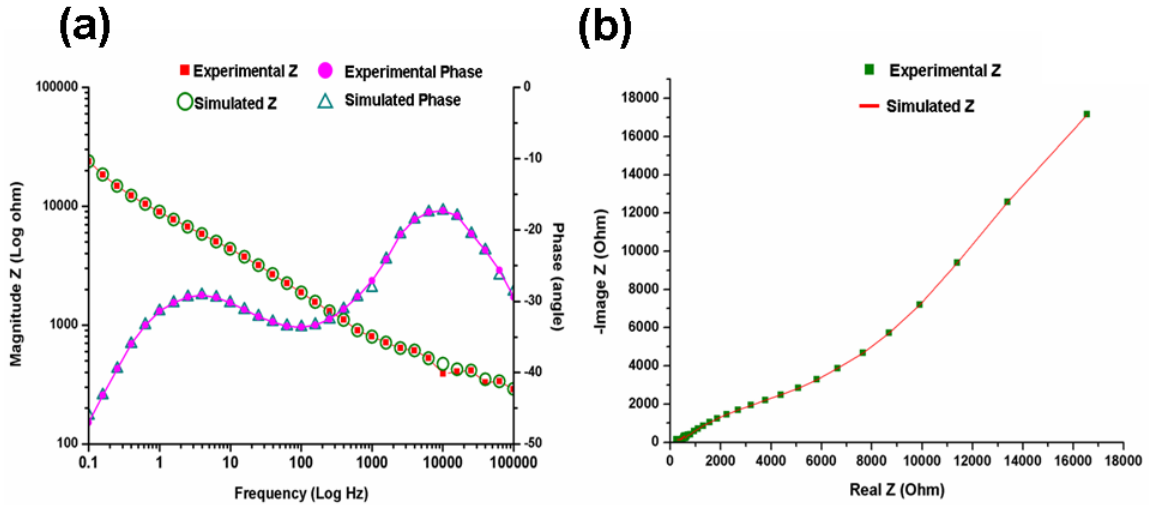
Figure 73. Comparison of the experimental data of electrode coated with graphene in the duration of 48 hours implant and the results of refined simulation. (a) Bode plot (b)Nyquist

To evaluate the effect of graphene on encapsulation, we focused on the result of simulation for tissue component. Figure 74 shows the result of simulation which represents the development of the resistance in the tissue component against the duration of implant. The value of resistance of control group in each implanted time is higher than that of the coated electrode. Exponential fitting method was used to identify the increase rate of the resistance. The mathematical formula of the fitting method can be expressed as

$$Y = Y_0 + A_0 e^{tx} \tag{23}$$

Here Y represents the value of resistance, x represents the implanted duration. Y_0, A_0 and t are constant, where the value of t determines the increasing tendency of Y. The fitting results shows that the value of t in the control group is 4 time higher than the coated group. The parameter t shown in equation 23 can be used to indicate the biocompatibility of the material. Table 12 summarizes the fitting results and the fitting index of R^2. The increasing rate of the resistance for non-coated group is a lot faster than that of the coated group. The result indicates different accumulating rate of the cell onto the surface of electrode with different conditions. With the graphene coated on the surface of the electrode, it hindered the progressive immuno-response of the biological system. This led to slower increasing rate of the resistance, which was caused by the increase in cell density at the interface. Such influence also results in the tardy alteration process of charge transfer, which is confirmed by the less pronounced R-C arc of the coated group shown in Nyquist loci (fig.68).
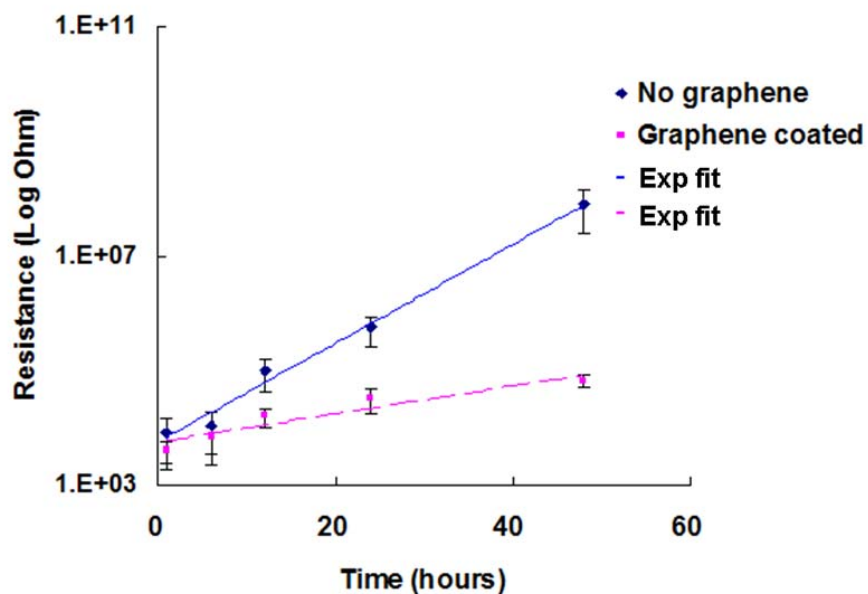
Figure 74. Result of simulation which shows the progress of resistance in tissue component against time. The exponential fitting method was used.

Table 12. Summary of the fitting results of the increase tendency of the resistance in tissue component

	A_0	t	R^2
Control group	5483.8	0.1987	0.99
Coated group	5582.1	0.0564	0.90

Mechanisms of dynamic interactions

In immuno-response, tissue encapsulation is a dynamic procedure. The mechanism of such a process can be investigated by scrutinizing each circuit model. In the equivalent circuit model, the effect of encapsulating tissue is represented by a modified parallel R-C circuit (figure 69). The variation of the effect for each element against time in this model can be used to interpret the dynamic behavior of encapsulating process. Figure 75 shows the simulation results, which was plotted using resistance and capacitance values against time. Here the value of capacitance represents the C_0 of CPE shown in equation 21. The value of resistance in the figure for 2 days is several times higher than that for 10 minutes. A continuous decrease in capacitance against the increase in time is also observed. At 24 hours, a sudden increase in resistance and drop in capacitance is noted. Such results can explain the dynamic mechanism of encapsulating process and its effect to the electrical property of system. As it was mentioned in chap 3, the mathematical expression of impedance magnitude can be

expressed as $|Z| = \sqrt{(\operatorname{Re} Z)^2 + (\operatorname{Im} Z)^2}$ or simplified as $|Z| = \sqrt{R^2 + \left(\dfrac{1}{j\omega C}\right)^2}$ where the

R is resistance and C is capacitance. In figure 75, the sudden increase in resistance and the drop in capacitance will lead to the increase in impedance magnitude. This can explain the abrupt increase in impedance magnitude observed in figure 36b.
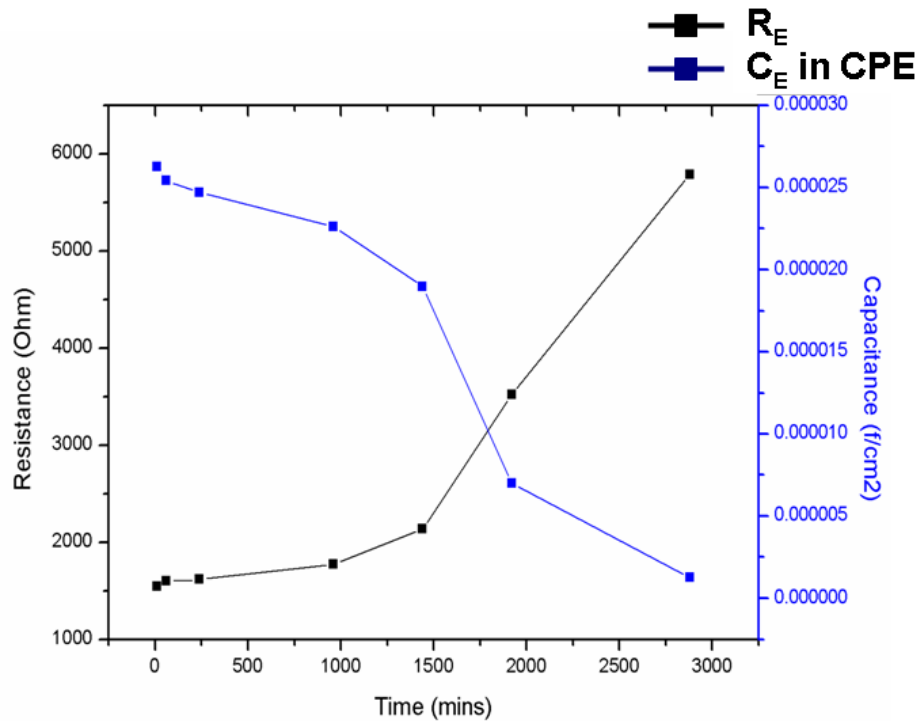
Figure 75. Simulation result of the circuit of encapsulating tissue. The
figure shows the variation of resistance and capacitance against
implaned time.

In the tissue layer, the charge transport pathway can be conducted along two

ways. One is the charge going across the cells. The polarized cell membrane causes the

transport path of charge similar to capacitive impedance behavior. The other is the

charge going between the cells. This gives the resistive impedance behavior. Figure 76

shows the schematic illustration of charge transport in tissue component of interface.

During the encapsulating process, the hemocyte started to coagulate and

encapsulate the surrounding area of electrode. At low cell density, the charge transferred

through sufficient free pathways between the cells. Those low resistance pathways was

gradually reduced due to the high cell density at longer time. The charge carrier was

forced to go across the cell which exhibited capacitive behavior. This phenomenon explains the presence of R-C effect in the impedance loci at 24 hours implanted time, and the dynamic mechanism of the interaction.
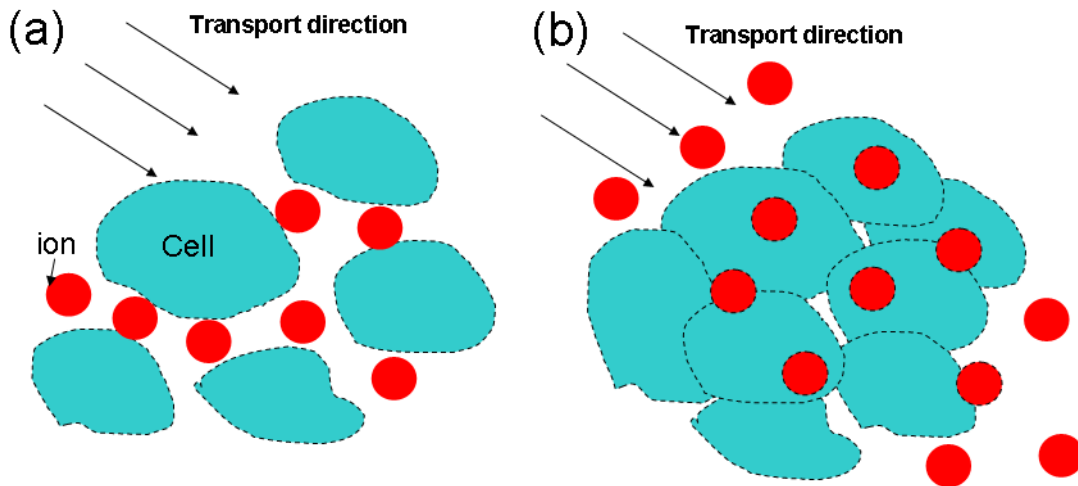
Figure 76. Illustration of charge alteration due to the dynamic tissue interaction. (a) Resistive impedance behavior at low cell density condition. (b) Capacitive impedance behavior at high cell density condition

Mathematical model

In this study, the equivalent circuit model has been proposed and its validity has also been confirmed using simulating algorithm to fit the experimental data. The model shown in section 6.1 and 6.2 are based on the physical structures of the interface. The effect to the system impedance of each component can be calculated and interpreted by such model. However, the mathematical representation for the system impedance is also important to describe the dynamic behavior of entire system. This information is useful

for circuit analysis and design of neural implant. In this section, the circuit model is derived based on the physical structure and the mathematic expression of each component.

Modification of Randal model

In an electrode-electrolytic system, Randle model [183] has been widely used to explain the phenomenon of charge transfer. The model is constructed by a polarization capacitance (Cp) in parallel with a serial combination of resistance (R) and capacitance (C). The schematic illustration of Randle model is shown in figure 77. Such theoretical model describes the electrochemical reaction in equilibrium state of the electrode subjected to an AC perturbation potential.
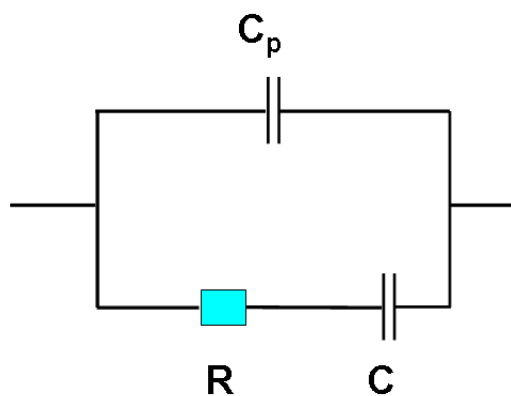
Figure 77. Illustration of Randle model.

The mathematical expression of Randle model can be derived using Faradaic admittance [184]. The admittance (Y) is the inverse of Z which can be expressed as

$$Y(\omega) = \lim \frac{I(\omega)}{V(\omega)} \quad \text{where } |V(\omega)| \sim 0 \tag{24}$$

therefore, the impedance of Randle model can be expressed as

$$Z_{total} = \frac{(Z_r + Z_c)Z_{cp}}{Z_r + Z_c + Z_{cp}} \tag{25}$$

where Zr is the charge resistance, Zc is charge capacitance, and Zcp is the double layer capacitance.

The Randle theory is limited in a clean electrode-electrolyte interface since Randle used a capillary dropping electrode. Other effects in the tissue component should be considered. We used a constant phase element and a Warburg impedance to predict the effect of ionic diffusion and the surface roughness. The equation 25 can be revised as

$$Z(\omega) = \frac{(Z_r + Z_W)Z_{cpe}}{Z_r + Z_W + Z_{cpe}} \tag{26}$$

it yields

$$Z(\omega) = \frac{(R_r + \sigma\omega^{-0.5} - j\sigma\omega^{-0.5})}{1 + A_0(j\omega)^\alpha(R_r + \sigma\omega^{-0.5} - j\sigma\omega^{-0.5})} \tag{27}$$

This complex impedance can be used to represent the general behavior of charge transport in the encapsulating tissue. In neural recording, obtaining the reliable signal is the key to understand the neural behavior. The existence of the encapsulating tissue would cause the additional drop of the output signal. The model presented here can predict the potential drop at the given frequency when the electrical signal passes

through the encapsulating tissue. It can be used as a compensation for signal processing

to obtain the authentic neural signal.

Interfacial model for implanted electrodes

The physical structure of the developed circuit model includes interfacial double

layer, encapsulating compartment, and silver oxide. The resistance in the double layer,

tissue layer and oxide layer are connected in series. The capacitor in the double layer is

coupled with other elements in parallel. The system impedance therefore can be

expressed as.

$$Z_{eq} = Z_{R.E} + \cfrac{1}{\cfrac{1}{Z_{cd}} + \cfrac{1}{Z_{rd} + Z_e + Z_o}} \tag{28}$$

This equation can thus be simplified as

$$Z_{eq} = Z_{R.E} + \frac{Z_{cd}(Z_{rd} + Z_e + Z_o)}{Z_{cd} + Z_{rd} + Z_e + Z_o} \tag{29}$$

In the tissue component, a resistor connects with Warburg impedance in series.

This combination coupled with a Constant Phase Element (CPE) in parallel. The

Impedance Z_e can be expressed as

$$Z_e = \frac{Z_{cpe}(Z_{re} + Z_w)}{Z_{cpe} + Z_{re} + Z_w} \tag{30}$$

130

By applying equation 30 to equation 29, the system impedance can be simplified as

$$Z_{eq} = Z_{R.E} + \frac{Z_{cd}(Z_{rd} + Z_o)(Z_{cpe} + Z_{re} + Z_w) + Z_{cd}Z_{cpe}(Z_{re} + Z_w)}{(Z_{rd} + Z_o + Z_{cd})(Z_{cpe} + Z_{re} + Z_w) + Z_{cpe}(Z_{re} + Z_w)}$$

(31)

Equation 31 can also be expressed as equation 31 using mathematical expression, R, to substitute all the resistances of different element. Therefore, the system impedance can be expressed as

$$Z_{eq} = Z_{R.E} + \frac{Z_{cd}(R_d + Z_o)(Z_{cpe} + R_{re} + Z_w) + Z_{cd}Z_{cpe}(R_{re} + Z_w)}{(R_{rd} + Z_o + Z_{cd})(Z_{cpe} + R_{re} + Z_w) + Z_{cpe}(R_{re} + Z_w)}$$

(32)

In case of neural system, the frequency of signal is usually preset at 1 KHz. At this frequency, the effect of the Warburg impedance is small and can be ignored. It's mainly due to the limited travel distance of reactants at high frequency range [177]. Under the circumstance, the system impedance can be further simplified as

$$Z_{eq} = R_{R.E} + \frac{Z_{cd}(R_d + Z_o)(Z_{cpe} + R_{re}) + Z_{cd}Z_{cpe}(R_{re})}{(R_{rd} + Z_o + Z_{cd})(Z_{cpe} + R_{re}) + Z_{cpe}(R_{re})}$$

(33)

Finalized mathematical model which represents interfacial response of impedance in the electrode-neural system can be expressed in equation 34. This is done by employing the mathematical term of each element to equation 33.

131

$$Z_{eq} = R_{R.E} + \frac{1/j\omega C_{cd}\left[(R_d + 1/j\omega C_o)(A(j\omega)^{-\alpha} + R_{re}) + A(j\omega)^{-\alpha}(R_{re})\right]}{(R_{rd} + 1/j\omega C_o + 1/j\omega C_{cd})(A(j\omega)^{-\alpha} + R_{re}) + A(j\omega)^{-\alpha}(R_{re})} \tag{34}$$

Table 13 presents the symbol for each electrical element used in the model and its representation. Table 14 summaries the mathematical expression for each electrical component used in the model.

Table 13. Terminology of all elements used in mathematical modeling

Symbol	Representation	Symbol	Representation
Z_{eq}	System impedance	Z_{cpe}	CPE impedance
Z_{cd}	Double layer capacitance	Z_{re}	Resistance in encapsulation layer
Z_{rd}	Double layer resistance	Z_{wd}	Warburg impedance
Z_e	Encapsulation impedance	$Z_{R.E}$	Electrolyte resistance
Z_o	Oxide layer impedance		

Table 14. Mathematical expression of each component in circuit model.

Physical component	Mathematical expression
Resistance	R
Capacitance	$1/j\omega C$
CPE	$A_o(j\omega)^{-\alpha}$

General model for implanted electrode

The model described in this study can represent the general phenomenon of charge transfer at the bio-interface. Three major components were delineated using both physical and mathematical model, which are interfacial double layer, encapsulating tissue, and the substrate. Due to the nature of different materials chosen as substrate of implant, the charge transfer at the interface varies accordingly. Here we constructed a general model to describe impedance of bio-electrode interface (fig 78). The component X shown in the figure represents the equilibrium circuit of the substrate.

As mentioned in chapter1, several materials have been used as an electrode for neural implant. Those materials include gold, platinum, silver, iridium oxide, polymer coatings and carbon nano-tube, among many others. Materials with different chemical and electrical properties interact differently with the bio-system. As discussed in chapter 4, chemical reaction is one of the mechanisms affecting the interfacial impedance. Here we categorize most implanting electrodes into chemically active metals and chemically inert materials. For polymer coating materials, the conductive materials embedded in the polymer matrix allow the charge transfer while the polymer matrix creates the charge separation. Such materials can thus be categorized as conductive polymer due to this unique property. Table 15 lists some of the materials used as electrode.

Table 15. Summary of some materials used as electrode
.

Category	Examples of Materials	References
Active metals	Silver, iridium	[117, 178, 185]
Inert materials	Gold, platinum, Carbon nanotube.	[76, 186]
Conductive polymers	Polythiophene, poly-3,4-ethylene dioxyiophene (PEDOT), Polypyrrole,	[123, 187]

The interaction between the substrate and the biological environment determines the circuit of X in fig. 78. For chemically active metals, metal oxide forms at the interface which can be presented as a capacitor. For chemically inert materials, the X component can be excluded from the circuitry. Under such circumstance, the interaction between the implant and the host biological environment is solely limited to the growth of encapsulating tissue. For conductive polymers, the X component (in fig.78) can be represented as a parallel R-C circuit. With the knowledge of material which is chosen to be the substrate of implant, we will be able to utilize this general model to predict the impedance of the interface of bio-electrode system.
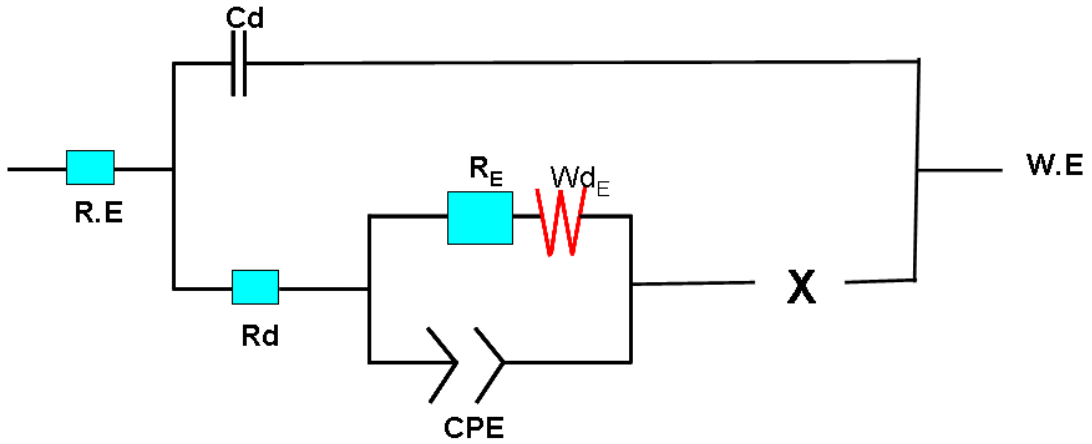
Figure 78. General model of bio-electrode interface

Here we use the Faradaic admittance to construct the mathematical form of the general model. It yields

$$Z_{eq} = Z_{R.E} + \cfrac{1}{\cfrac{1}{Z_{cd}} + \cfrac{1}{Z_{rd} + Z_e + Z_X}} \tag{35}$$

which can be simplified as

$$Z_{eq} = Z_{R.E} + \frac{Z_{cd}(Z_{rd} + Z_e + Z_x)}{Z_{cd} + Z_{rd} + Z_e + Z_x} \tag{36}$$

where Ze is the modified Randal model which can be expressed as

$$Z_e = \frac{(Z_r + Z_W)Z_{cpe}}{Z_r + Z_W + Z_{cpe}}$$

Here we summarize the models for three major categories. For a chemically active metal, it mostly forms metal oxide on the surface in the biological environment. Equation 36 can be expressed as

$$Z_{eq} = Z_{R.E} + \frac{Z_{cd}(Z_{rd} + Z_e + C_{mo})}{Z_{cd} + Z_{rd} + Z_e + C_{mo}} \qquad (37)$$

where C_{mo} represents as a capacitor

For a chemically inert material, the interfacial interaction can be limited to tissue encapsulation. Equation 36 can thus be expressed as

$$Z_{eq} = Z_{R.E} + \frac{Z_{cd}(Z_{rd} + Z_e)}{Z_{cd} + Z_{rd} + Z_e} \qquad (38)$$

For a conductive polymer material, equation 36 can be expressed as

$$Z_{eq} = Z_{R.E} + \frac{Z_{cd}(Z_{rd} + Z_e + Z_{pm})}{Z_{cd} + Z_{rd} + Z_e + Z_{pm}} \qquad (39)$$

where Z_{pm} is expressed as

$$Z_{pm} = \frac{1}{R_{pm}} + j\omega C_{pm} = \frac{R_{pm}}{1 + j\omega R_{pm} C_{pm}}$$

where R_{pm} represents the charge resistance and C_{pm} represents the charge capacitance.

Figure 79 shows the modeling results of Impedance spectra in frequency domain. It is noticed that the impedance magnitude (fig. 79) of chemically inert materials is lower than the other two materials at low frequency range (<50hz). Two relaxation processes are observed in conductive polymer and chemically active material whereas only one relaxation process is found. This indicates that the chemically inert material has only one charge transfer occurring at the interface. The impedance spectra at the high frequency range (>100Hz) for all three models show insignificant variation. This indicates that the substrate only affects the change of impedance at lower frequency range.
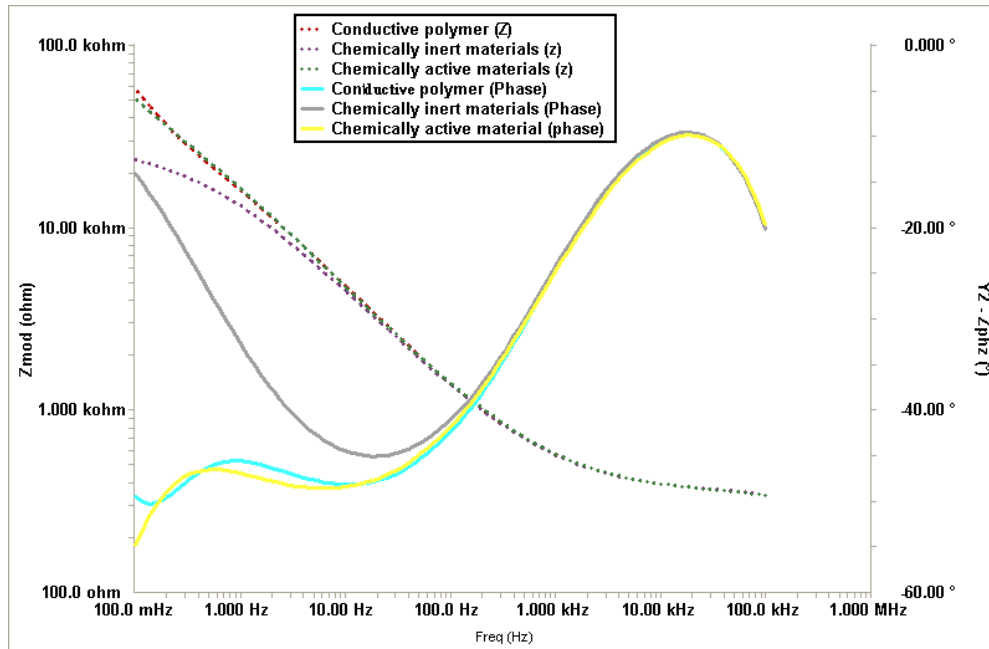
Figure 79. Modeled Impedance spectrum in frequency domain

Figure 80 shows the modeling results of Impedance spectra in Nyquist plot. All three models show an alteration of charge transfer at high frequency range, which is caused by the tissue component. The impedance locus of chemically inert materials shows a complete R-C arc. It shows large variation in Zreal component, which indicates resistive behavior. It also has lower impedance magnitude than the other two materials at low frequency range. This result comes in agreement with the observation in figure 79. The impedance locus of chemically active materials shows more capacitive behavior at low frequency range which is caused by the formation of an oxide layer. In this figure, three different models have identical behavior (phase) at the high frequency range but distinct behaviors at the low frequency range.
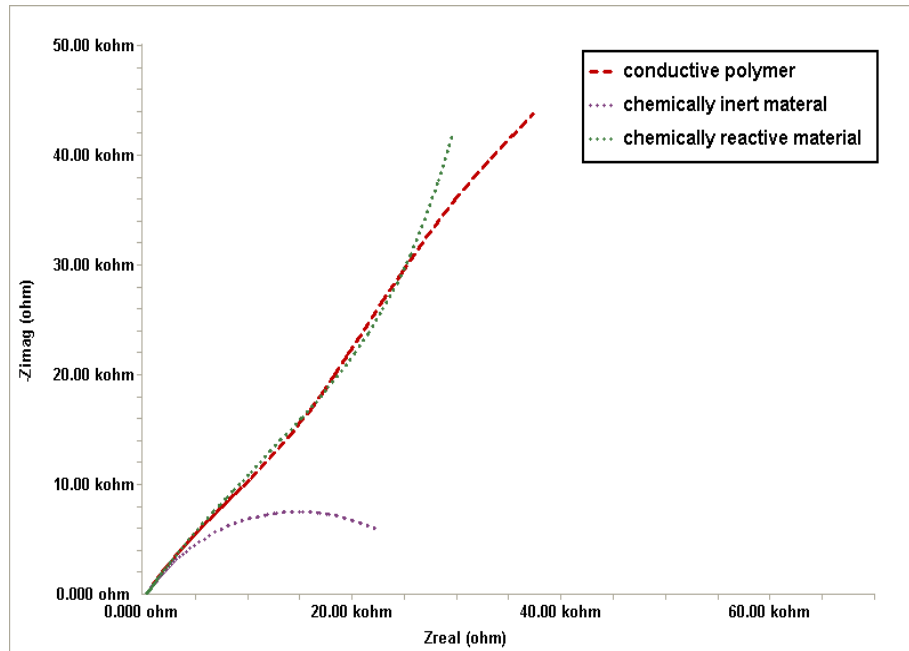
Figure 80. Modeled Impedance spectrum in Nyquist plot

Summary

A circuit representation of the interface in electrode-bio system was established to interpret in-vivo behavior. Dynamic mechanism of biological interaction was also proposed. This explains the direct influence of the cellular development on charge transport. Physical equivalent circuit model was derived using the data obtained by EIS measurements. Mathematical model was generated based on the physical model. The information obtained by the modeling can be helpful for further study in circuit design of neural implant. The model presented in this chapter can also be used to describe general impedimetric behavior of different materials of implants. Such information is useful for material selection and design of implant electrode.

138

CHAPTER VII

CONCLUSIONS AND FUTURE RECOMMENDATIONS[*]

Conclusions

This research investigated interfacial interactions between the implanted electrode and the host neural system of an American cockroach. Experiments were performed to monitor and analyze the variation of the electrical properties at the interface using Electrochemical Impedance Spectroscopy. The effect of immuno-response to the degradation of an electrode was studied. Surface modification of the implanted electrode was also conducted using graphene coating in order to engineer the properties of electrode for better signal acquisition and longer life span of the electrode. Here are the highlight of major results and discoveries:

1. It was found that the biological system reacted with the implanted electrode in two competing mechanisms. The oxygen-rich environment of biological system interacted with the metal electrode, which results in the formation of metal oxide. Immuno-response affected the implant by forming encapsulating tissue around the electrode. Both mechanisms led to the degradation of implanted electrode, i.e. increase of system impedance. It was also shown

---

that the contribution of immuno-response to the increase in impedance for long term implantation is more dominant.

2. It was found that the charge transport pathway at interface was altered due to the accumulation of the encapsulation tissue on the electrode. The dynamic behavior of the encapsulating process and its effect to the charge transport at interface was proposed. The increase of cell density at the interface forced the charge to transfer from resistive pathway to capacitive pathway. The interpretation of such dynamic process was determined through qualitative (histology) and quantitative (EIS) analysis.

3. The electrical representation of the interface was established using equivalent circuit modeling. It was found that three major components constitute the interface, i.e. interfacial double layer, tissue component, and substrate. Physical and mathematical model were created to describe the impedimetric behavior of the interface. Such results are useful to predict the kinetics and dynamics of immuno-response and valuable for further study in circuit design of neural implant.

4. It was found that the graphene prevents the substrate from being oxidized. The results of EIS also showed that the graphene-coated electrodes exhibited slower rate of electrode degradation. The development in relaxation phenomenon and the R-C arc across the implanting duration were used to represent the development of encapsulating tissue. The graphene coating constrained the encapsulating tissue from developing, as evident by the

smaller maximum peak in phase angle and less pronounced R-C arc. The
results obtained by the modeling also suggested slower increase rate in
resistance in the tissue component. Both characteristics of graphene suggest
that such a material has great advantage in the application of neural implant.

This research developed a methodology to analyze the interfacial interactions
between the implanted electrode and host immuno-system. Such approach provided the
insight of how the dynamic process of immuno-response alters the electrical properties
of the interface. The dynamic behavior of immuno-response can be tailored through
surface modification of the implanted electrode. Such approach can extend the
functional longevity of the neural implant.

Future recommendations

To obtain the full insight from the electrode-bio interaction, several variables
need to be future investigated. First of all, different biological substances are responsible
for the immuno-reaction in different biological system. The continuation of this research
should be expanded to investigate other electrode-bio systems. The results presented in
this study focused on the interaction between electrode and the neural system of
American cockroach. The data presented here is limited to the immuno-response of
hemocyte. It would be necessary to understand the degrading rate of the electrode
efficiency caused by other immuno-substances, and the effect of those substances to the
alteration of charge transfer at the interface.

Secondly, silver electrode used in this study is comparatively chemically active. Using chemically inert material might explore other interaction at the interface established by the oxygen-rich environment, e.g., a plane with aligned oxygen molecules due to the electronegativity.

Finally, the life span of graphene-coated electrode should be further improved by developing a uniform and continuous graphene coating on the electrode surface. The predicted behavior of the immuno response will be more solidified and the quantitatively substantial.

REFERENCES

1   Held, M., Schuhmann, W., Jahreis, K., Schmidt, H.L., Microbial biosensor array with transport mutants of Escherichia coli K12 for the simultaneous determination of mono-and disaccharides, Biosensors and Bioelectronics, **17:11–12,** (2002) 1089-1094.

2   Tlili, C., Reybier, K., Géloën, A., Ponsonnet, L., Martelet, C., Ouada, H.B., Lagarde, M., Jaffrezic-Renault, N., Fibroblast Cells: A sensing bioelement for glucose detection by impedance spectroscopy, Analytical Chemistry, **75:14,** (2003) 3340-3344.

3   Vianello, F., Ragusa, S., Cambria, M.T., Rigo, A., A high sensitivity amperometric biosensor using laccase as biorecognition element, Biosensors and Bioelectronics, **21:11,** (2006) 2155-2160.

4   Andle, J.C., Vetelino, J.F., Acoustic wave biosensors, Sensors and Actuators A: Physical, **44:3,** (1994) 167-176.

5   Sethi, R.S., Transducer aspects of biosensors, Biosensors and Bioelectronics, **9:3,** **(**1994) 243-264.

6   Ivnitski, D., Wilkins, E., Tien, H.T., Ottova, A., Electrochemical biosensor based on supported planar lipid bilayers for fast detection of pathogenic bacteria, Electrochemistry Communications, **2:7,** (2000) 457-460.

7   Pal, S., Alocilja, E.C., Downes, F.P., Nanowire labeled direct-charge transfer biosensor for detecting Bacillus species, Biosensors and Bioelectronics, **22:9–10,** (2007) 2329-2336.

8   Lillie, G., Payne, P., Vadgama, P., Electrochemical impedance spectroscopy as a platform for reagentless bioaffinity sensing, Sensors and Actuators B: Chemical, **78:1–3,** **(**2001) 249-256.

9   K'Owino, I.O., Sadik, O.A., Impedance spectroscopy: a powerful tool for rapid biomolecular screening and cell culture monitoring, Electroanalysis, **17:23,** (2005) 2101-2113.

10   Rodriguez, M.C., Kawde, A.-N., Wang, J., Aptamer biosensor for label-free impedance spectroscopy detection of proteins based on recognition-induced switching of the surface charge, Chemical Communications, **34,** (2005) 4267-4269.

11   Varshney, M., Li, Y., Interdigitated array microelectrodes based impedance biosensors for detection of bacterial cells, Biosensors and Bioelectronics, **24:10,** (2009) 2951-2960.

12   Gautier, S.M., Blum, L.J., Coulet, P.R., Fibre-optic biosensor based on luminescence and immobilized enzymes: microdetermination of sorbitol, ethanol and oxaloacetate, Journal of bioluminescence and chemiluminescence, **5:1,** (1990) 57-63.

13   McCurley, M.F., An optical biosensor using a fluorescent, swelling sensing element, Biosensors and Bioelectronics, **9:7,** (1994) 527-533.

14   Potyrailo, R.A., Conrad, R.C., Ellington, A.D., Hieftje, G.M., Adapting selected nucleic acid ligands (Aptamers) to Biosensors, Analytical Chemistry, **70:16,** (1998) 3419-3425.

15   Choudhury, B., Shinar, R., Shinar, J., Glucose biosensors based on organic light-emitting devices structurally integrated with a luminescent sensing element, Journal of Applied Physics, **96:5,** (2004) 2949-2954.

16   Haes, A., Zou, S., Schatz, G., Van Duyne, R., A nanoscale optical biosensor: The long range distance dependence of the localized surface plasmon resonance of noble metal nanoparticles, The Journal of Physical Chemistry B, **108:1,** (2004) 109-116.

17   Haes, A.J., Chang, L., Klein, W.L., Van Duyne, R.P., Detection of a biomarker for alzheimer's disease from synthetic and clinical samples using a nanoscale optical biosensor, Journal of the American Chemical Society, **127:7,** (2005) 2264-2271.

18   Grate, J.W., Frye, G.C., Acoustic wave sensors, Sensors Update, **2:1,** (1996) 37-83.

19   White, R.M., Voltmer, F.W., Direct piezoelectric coupling to surface elastic waves, Applied Physics Letters, **7:12,** (1965) 314-316.

20   Drobe, H., Leidl, A., Rost, M., Ruge, I., Acoustic sensors based on surface-localized HPSWs for measurements in liquids, Sensors and Actuators A: Physical, **37–38,** (1993) 141-148.

21   Calabrese, G.S., Wohltjen, H., Roy, M.K., Surface acoustic wave devices as chemical sensors in liquids: evidence disputing the importance of Rayleigh wave propagation, Analytical Chemistry, **59:6,** (1987) 833-837.

22   Gizeli, E., Stevenson, A.C., Goddard, N.J., Lowe, C.R., A novel Love-plate acoustic sensor utilizing polymer overlayers, Ultrasonics, Ferroelectrics and Frequency Control, IEEE Transactions on, **39:5,** (1992) 657-659.

23   Kovacs, G., Venema, A., Theoretical comparison of sensitivities of acoustic shear wave modes for (bio)chemical sensing in liquids, Applied Physics Letters, **61:6,** (1992) 639-641.

24   Wang, Z., Jen, C.K., Cheeke, J.D.N., Mass sensitivity of two-layer shear horizontal plate wave sensors, Ultrasonics, **32:3,** (1994) 209-215.

25   Länge, K., Rapp, B., Rapp, M., Surface acoustic wave biosensors: a review, Analytical and Bioanalytical Chemistry, **391:5,** (2008) 1509-1519.

26   Ackermann, T.,Book Review: Analytical solution calorimetry. Edited by J. K. Grime, Angewandte Chemie International Edition in English, **25:5,** (1986) 482-483.

27   Flygare, L., Danielsson, B., Advantages of organic solvents in thermometric and optoacoustic enzymic analysis, Annals of the New York Academy of Sciences, **542:1,** (1988) 485-496.

28   Homola, J., Yee, S., Gauglitz, G., Surface plasmon resonance sensors: review, Sensors and Actuators B: Chemical, **54:1-2,** (1999) 3-15.

29   Wood, R.W., On a remarkable case of uneven distribution of light in a diffraction grating spectrum, Proceedings of the Physical Society of London, **18:1,** (1902) 269-275.

30   Liedberg, B., Nylander, C., Lunström, I., Surface plasmon resonance for gas detection and biosensing, Sensors and Actuators, **4:0,** (1983) 299-304.

31   Zhang, L.M., Uttamchandani, D., Optical chemical sensing employing surface plasmon resonance, Electronics Letters, **24:23,** (1988) 1469-1470.

32   Vukusic, P.S., Bryan-Brown, G.P., Sambles, J.R., Surface plasmon resonance on gratings as a novel means for gas sensing, Sensors and Actuators B: Chemical, **8:2,** (1992) 155-160.

33   Moss, S.D., Janata, J., Johnson, C.C., Potassium ion-sensitive field effect transistor, Analytical Chemistry, **47:13,** (1975) 2238-2243.

34   Duroux, P., Emde, C., Bauerfeind, P., Francis, C., Grisel, A., Thybaud, L., Arstrong, D., Depeursinge, C., Blum, A.L., The ion sensitive field effect transistor (ISFET) pH electrode: a new sensor for long term ambulatory pH monitoring, Gut, **32:3,** (1991) 240-245.

35	Esashi, M., Matsuo, T., Integrated micro multi ion sensor using field effect of semiconductor, Biomedical Engineering, IEEE Transactions on, **BME-25:2,** (1978) 184-192.

36	Kharitonov, A.B., Zayats, M., Lichtenstein, A., Katz, E., Willner, I., Enzyme monolayer-functionalized field-effect transistors for biosensor applications, Sensors and Actuators B: Chemical, **70:1–3,** (2000) 222-231.

37	Lenigk, R., Carles, M., Ip, N.Y., Sucher, N.J., Surface Characterization of a Silicon-Chip-Based DNA Microarray, Langmuir, **17:8,** (2001) 2497-2501.

38	Bent, S.F., Organic functionalization of group IV semiconductor surfaces: principles, examples, applications, and prospects, Surface Science, **500:1–3,** (2002) 879-903.

39	Wang, Y., Lieberman, M., Growth of ultrasmooth octadecyltrichlorosilane self-assembled monolayers on SiO2, Langmuir, **19:4,** (2003) 1159-1167.

40	Midwood, K.S., Carolus, M.D., Danahy, M.P., Schwarzbauer, J.E., Schwartz, J., Easy and efficient bonding of biomolecules to an oxide surface of silicon, Langmuir, **20:13,** (2004) 5501-5505.

41	Sethi, R.S., Lowe, C.R., Electrochemical microbiosensors, Microsensors, IEE Colloquium on, **9**, (1990), 1-5

42	Thévenot, D.R., Toth, K., Durst, R.A., Wilson, G.S., Electrochemical biosensors: recommended definitions and classification, Biosensors and Bioelectronics, **16:1–2,** (2001) 121-131.

43	Mioslav, P., Petr, S., Electrochemical biosensors-principles and applications, J. Appl. Biomed, **6:**(2008) 57-64.

44   Göpel, W., Bioelectronics and nanotechnologies, Biosensors and Bioelectronics, **13:6,** (1998) 723-728.

45   Lammers, F., Scheper, T., Thermal biosensors in biotechnology: thermal biosensors, bioactivity, bioaffinitty, in: Bhatia, P, Danielsson, B, Gemeiner, P, Grabley, S, Lammers, F, Mukhopadhyay, A, Ramanathan, K, Saleemuddin, M, Scheper, T, Stefuca, V, Thiericke, R, Xie, B (Eds.), vol. 64, Springer Berlin / Heidelberg, 1999, pp. 35-67.

46   Wallace, G.G., Smyth, M., Zhao, H., Conducting electroactive polymer-based biosensors, TrAC Trends in Analytical Chemistry, **18:4,** (1999) 245-251.

47   Braun, S., Rappoport, S., Zusman, R., Avnir, D., Ottolenghi, M., Biochemically active sol-gel glasses: The trapping of enzymes, Materials Letters, **61:14–15,** (2007) 2843-2846.

48   Wang, J., Sol–gel materials for electrochemical biosensors, Analytica Chimica Acta, **399:1–2,** (1999) 21-27.

49   Ellerby, L., Nishida, C., Nishida, F., Yamanaka, S., Dunn, B., Valentine, J., Zink, J., Encapsulation of proteins in transparent porous silicate glasses prepared by the sol-gel method, Science, **255:5048,** (1992) 1113-1115.

50   Davis, J.J., Coleman, K.S., Azamian, B.R., Bagshaw, C.B., Green, M.L.H., Chemical and biochemical sensing with modified single walled carbon nanotubes, Chemistry – A European Journal, **9:16,** (2003) 3732-3739.

51   Wang, J., Nanomaterial-based electrochemical biosensors, Analyst, **130:4,** (2005) 421-426.

52   Wang, J., Carbon-nanotube aased electrochemical biosensors: A Review, Electroanalysis, **17:1,** (2005) 7-14.

53   Kerman, K., Saito, M., Tamiya, E., Yamamura, S., Takamura, Y., Nanomaterial-based electrochemical biosensors for medical applications, TrAC Trends in Analytical Chemistry, **27:7, (**2008) 585-592.

54   Cai, H., Wang, Y., He, P., Fang, Y., Electrochemical detection of DNA hybridization based on silver-enhanced gold nanoparticle label, Analytica Chimica Acta, **469:2, (**2002) 165-172.

55   Du, P., Li, H., Mei, Z., Liu, S., Electrochemical DNA biosensor for the detection of DNA hybridization with the amplification of Au nanoparticles and CdS nanoparticles, Bioelectrochemistry, **75:1, (**2009) 37-43.

56   Wang, J., Liu, G., Merkoçi, A., Electrochemical coding technology for simultaneous detection of multiple DNA targets, Journal of the American Chemical Society, **125:11, (**2003) 3214-3215.

57   Hue, B., Pelhata, M., Callec, J.J., Chanelet, J., Synaptic transmission in the sixth ganglion of the cockroach: action of 4-aminopyridine, Journal of Experimental Biology, **65:3, (**1976) 517-527.

58   Hall, Z.W., Sanes, J.R., Synaptic structure and development: The neuromuscular junction, Cell, **72, Supplement:0, (**1993) 99-121.

59   Harris-Warrick, R.M., Marder, E., Modulation of Neural Networks for Behavior, Annual Review of Neuroscience, **14:1, (**1991) 39-57.

60   Kyung Hwan, K., Sung June, K., A wavelet-based method for action potential detection from extracellular neural signal recording with low signal-to-noise ratio, Biomedical Engineering, IEEE Transactions on, **50:8, (**2003) 999-1011.

61   Yoshida, T., Mashimo, T., Akagi, M., Iwata, A., Yoshida, M., Uematsu, K., A design of neural signal sensing LSI with multi-input-channels, Ieice Transactions on

Fundamentals of Electronics Communications and Computer Sciences, **E87A:**(2004) 376-383.

62   Holzer, R., Shimoyama, I., 1997, 7-11 th Sep, Locomotion control of a bio-robotic system via electric stimulation, Intelligent Robots and Systems, 1997. IROS '97., Proceedings of the 1997 IEEE/RSJ International Conference, Grenoble, France.

63   Lee, C.J., Oh, S.J., Song, J.K., Kim, S.J., Neural signal recording using microelectrode arrays fabricated on liquid crystal polymer material, Materials Science and Engineering: C, **24:1–2,** (2004) 265-268.

64   Lee, K., Singh, A., He, J., Massia, S., Kim, B., Raupp, G., Polyimide based neural implants with stiffness improvement, Sensors and Actuators B: Chemical, **102:1,** (2004) 67-72.

65   Wolpaw, J.R., Birbaumer, N., McFarland, D.J., Pfurtscheller, G., Vaughan, T.M., Brain–computer interfaces for communication and control, Clinical Neurophysiology, **113:6,** (2002) 767-791.

66   Ficke, R.C., (1992), Digest of Data on Persons with disabilities. An InfoUse Report by US Department of Education, National institute on disability and rehabilitatoin research, pp.207

67   Bethesda, (1993), Research plan for the national center for medical rehabilitation research, National center for medical rehabilitation. NIH publication No. 93-3509, pp.104

68   Murray, C.J.L., Lopez, A.D., Global mortality, disability, and the contribution of risk factors: Global Burden of Disease Study, The Lancet, **349:9063,** (1997) 1436-1442.

69   Abresch, R.T., Han, J.J., Carter, G.T., Rehabilitation management of neuromuscular disease: the role of exercise training, Journal of clinical neuromuscular disease, **11:1,** (2009) 7-21.

70   Damper, R.I., Burnett, J.W., Gray, P.W., Straus, L.P., Symes, R.A., Hand-held text-to-speech device for the non-vocal disabled, Journal of Biomedical Engineering, **9:4,** **(**1987) 332-340.

71   LaCourse, J.R., Hludik, F.C., Jr., An eye movement communication-control system for the disabled, Biomedical Engineering, IEEE Transactions on, **37:12,** (1990) 1215-1220.

72   Kubota, M., Sakakihara, Y., Uchiyama, Y., Nara, A., Nagata, T., Nitta, H., Ishimoto, K., Oka, A., Horio, K., Yanagisawa, M., New ocular movement detector system as a communication tool in ventilator-assisted Werdnig–Hoffmann disease, Developmental Medicine & Child Neurology, **42:01,** (2000) 61-64.

73   Hoffer, J.A., Stein, R.B., Haugland, M.K., Sinkjaer, T., Durfee, W.K., Schwartz, A.B., Loeb, G.E., Kantor, C., Neural signals for command control and feedback in functional neuromuscular stimulation: a review, Journal of rehabilitation research and development, **33:2,** (1996) 145-157.

74   Kilgore, K.L., Peckham, P.H., Keith, M.W., Thrope, G.B., Wuolle, K.S., Bryden, A.M., Hart, R.L., An implanted upper-extremity neuroprosthesis. follow-up of five patients, The Journal of bone and joint surgery. American volume, **79:4,** (1997) 533-541.

75   KA, F., G, P., R, K., RJ, T., EB, M., Walking with a hybrid orthosis system, Journal of Spinal cord, **37:11,** (1999) 800-804.

76   Hamill, O.P., Marty, A., Neher, E., Sakmann, B., Sigworth, F.J., Improved patch-clamp techniques for high-resolution current recording from cells and cell-free membrane patches, Pflügers Archiv European Journal of Physiology, **391:2,** (1981) 85-100.

77   Jackson, M.B., (1998). Current protocals in neuroscience. John Wiley and Sons, Inc.

78   Shain, W., Spataro, L., Dilgen, J., Haverstick, K., Retterer, S., Isaacson, M., Saltzman, M., Turner, J.N., Controlling cellular reactive responses around neural prosthetic devices using peripheral and local intervention strategies, Neural Systems and Rehabilitation Engineering, IEEE Transactions on, **11:2,** (2003) 186-188.

79   Pena, F., Tapia, R., Seizures and neurodegeneration induced by 4-aminopyridine in rat hippocampus in vivo: role of glutamate- and GABA-mediated neurotransmission and of ion channels, Neuroscience, **101:3,** (2000) 547-561.

80   Kobayashi, R., Kanno, S., Lee, S., Fukushima, T., Sakamoto, K., Matsuzaka, Y., Katayama, N., Mushiake, H., Koyanagi, M., Tanaka, T., 2009, April 29th -May 2nd Development of double-sided Si neural probe with microfluidic channels using wafer direct bonding technique, Neural Engineering, 2009. NER '09. 4th International IEEE/EMBS Conference, Antalya, Turkey

81   Seidl, K., Spieth, S., Herwik, S., Steigert, J., Zengerle, R., Paul, O., Ruther, P.,in-Plane silicon probes or simultaneous neural recording and drug delivery, Journal of Micromechanics and Microengineering, **20:10,** (2010) 6.

82   Guo, K., Pei, W., Li, X., Gui, Q., Tang, R., Liu, J., Chen, H., Fabrication and characterization of implantable silicon neural probe with microfluidic channels, SCIENCE CHINA Technological Sciences, **55:1,** (2012) 1-5.

83   Takeuchi, S., Yoshida, Y., Ziegler, D., Mabuchi, K., Suzuki, T., 2004, 25-29th Jan, Parylene flexible neural probe with micro fluidic channel, Micro Electro Mechanical Systems, 2004. 17th IEEE International Conference on. (MEMS), Tokyo

84   Ziegler, D., Suzuki, T., Takeuchi, S., Fabrication of Flexible Neural Probes With Built-In Microfluidic Channels by Thermal Bonding of Parylene, Journal of Microelectromechanical Systems, **15:6,** (2006) 1477-1482.

85   Kovacs, G.T.A., Storment, C.W., Halks-Miller, M., Belczynski, C.R., Jr., Santina, C.C.D., Lewis, E.R., Maluf, N.I., Silicon-substrate microelectrode arrays for parallel recording of neural activity in peripheral and cranial nerves, Biomedical Engineering, IEEE Transactions on, **41:6,** (1994) 567-577.

86   Kovacs, G.T.A., Storment, C.W., Rosen, J.M., Regeneration microelectrode array for peripheral nerve recording and stimulation, Biomedical Engineering, IEEE Transactions on, **39:9,** (1992) 893-902.

87   Vetter, R.J., Williams, J.C., Hetke, J.F., Nunamaker, E.A., Kipke, D.R., Chronic neural recording using silicon-substrate microelectrode arrays implanted in cerebral cortex, Biomedical Engineering, IEEE Transactions on, **51:6,** (2004) 896-904.

88   Singh, A., Lee, K., He, J., Ehteshami, G., Massia, S., Raupp, G., 2003, 17-21 Sept. 2003, Benzocyclobutene (BCB) based intracortical neural implant, Engineering in Medicine and Biology Society, 2003. Proceedings of the 25th Annual International Conference of the IEEE,

89   Benmerah, S., Lacour, S.P., Tarte, E., 2009, 3-6 Sept, Design and fabrication of neural implant with thick microchannels based on flexible polymeric materials, Engineering in Medicine and Biology Society, 2009. EMBC 2009. Annual International Conference of the IEEE, Minneapolis

90   Takeuchi, S., Suzuki, T., Mabuchi, K., Fujita, H., 3D flexible multichannel probe array, Journal of Micromechanics and Microengineering, **14:**(2003) 104-107. DOI:10.1088/0960-1317/14/1/014

91   Hoogerwerf, A.C., Wise, K.D., 1991, 24-27 Jun 1991, A three-dimensional neural recording array, Solid-State Sensors and Actuators, 1991. Digest of Technical Papers, TRANSDUCERS '91., 1991 International Conference on,

92	Hoogerwerf, A.C., Wise, K.D., A three-dimensional microelectrode array for chronic neural recording, Biomedical Engineering, IEEE Transactions on, **41:12, (**1994) 1136-1146.

93	John, J., Li, Y., Zhang, J., Loeb, H.A., Xu, Y., Microfabricaion of 3D neural probes with combined electrical and chemical interfaces, Journal of Micromechanics and Microengineering, **21:105011, (**2011).

94	Wisniewski, N., Moussy, F., Reichert, W.M., Characterization of implantable biosensor membrane biofouling, Fresenius' Journal of Analytical Chemistry, **366:6, (**2000) 611-621.

95	Wang, P., Liu, Q., (2010). Cell-based biosensor: principles and applications. Norwood, MA. Artech House publishers.

96	Lal, R., Integrated biosensors: promises and problems, Bioelectrochemistry and Bioenergetics, **27:2, (**1992) 121-139.

97	Yang, G.-Z., (2006). Body sensor network. London, UK. Springer-Verlag London Limited.

98	Gerritsen, M., Jansen, J.A., Lutterman, J.A., Performance of subcutaneously implanted glucose sensors for continuous monitoring, The Netherlands Journal of Medicine, **54:4, (**1999) 167-179.

99	Linke, B., Kiwit, M., Thomas, K., Krahwinkel, M., Kerner, W., Prevention of the decrease in sensitivity of an amperometric glucose sensor in undiluted human serum, Clin Chem, **45:2, (**1999) 283-285.

100	Remes, A., Williams, D.F., Immune response in biocompatibility, Biomaterials, **13:11, (**1992) 731-743.

101   Voskerician, G., Anderson, J., (2006), Sensor biocompatibility and biofouling in real-time monitoring, in: Wiley Encyclopedia of Biomedical Engineering, Ed. Metin Akay, New York, John Wiley and Sons, Published online, 1-19, URL http://dx.doi.org/10.1002/9780471740360.ebs1370

102   Moussy, F., 2000, 12-14th Oct., Biosensor/tissue interactions, microtechnologies in medicine and biology, 1st Annual International, Conference On. 2000, Lyon, France

103   Reach, G., Feijen, J., Alcock, S., BIOMED concerted action chemical sensors for in vivo monitoring. The biocompatibility issue, Biosensors and Bioelectronics, **9:6,** **(**1994) 111-119.

104   Valdes, T.I., Moussy, F., A ferric chloride pre-treatment to prevent calcification of Nafion membrane used for implantable biosensors, Biosensors and Bioelectronics, **14:6,** (1999) 579-585.

105   Yu, B., Moussy, Y., Moussy, F., Coil-type implantable glucose biosensor with excess enzyme loading, Frontiers in bioscience : a journal and virtual library, **10:1,** **(**2005) 512-520.

106   Guilbault, G.G., Nanjo, M., A phosphate-selective electrode based on immobilized alkaline phosphatase and glucose oxidase, Analytica Chimica Acta, **78:1,** **(**1975) 69-80.

107   Zhang, W., Chang, H., Rechnitz, G.A., Dual-enzyme fiber optic biosensor for pyruvate, Analytica Chimica Acta, **350:1 − 2,** **(**1997) 59-65.

108   Gouda, M.D., Thakur, M.S., Karanth, N.G., A dual enzyme amperometric biosensor for monitoring organophosphorous pesticides, Biotechnology Techniques, **11:9,** **(**1997) 653-655.

109   Stokes, K.B., Polyether polyurethanes: biostable or not?, Journal of biomaterials applications, **3:2,** **(**1988) 228-259.

110   Updike, S.J., Shults, M.C., Rhodes, R.K., Gilligan, B.J., Luebow, J.O., von Heimburg, D., Enzymatic glucose sensors. Improved long-term performance in vitro and in vivo, ASAIO journal (American Society for Artificial Internal Organs : 1992), **40:2,** **(**1994) 157-163.

111   Palleschi, G., Ali Nabi Rahni, M., Lubrano, G.J., Ngwainbi, J.N., Guilbault, G.G., A study of interferences in glucose measurements in blood by hydrogen peroxide based glucose probes, Analytical Biochemistry, **159:1, (**1986) 114-121.

112   Kerner, W., Kiwit, M., Linke, B., Keck, F.S., Zier, H., Pfeiffer, E.F., The function of a hydrogen peroxide-detecting electroenzymatic glucose electrode is markedly impaired in human sub-cutaneous tissue and plasma, Biosensors and Bioelectronics, **8:9–10, (**1993) 473-482.

113   Geise, R.J., Adams, J.M., Barone, N.J., Yacynych, A.M., Electropolymerized films to prevent interferences and electrode fouling in biosensors, Biosensors and Bioelectronics, **6:2, (**1991) 151-160.

114   Treloar, P.H., Christie, I.M., Vadgama, P.M., Engineering the right membranes for electrodes at the biological interface; solvent cast and electropolymerised, Biosensors and Bioelectronics, **10:1–2, (**1995) 195-201.

115   Xindong, L., McCreery, D.B., Carter, R.R., Bullara, L.A., Yuen, T.G.H., Agnew, W.F., Stability of the interface between neural tissue and chronically implanted intracortical microelectrodes, Rehabilitation Engineering, IEEE Transactions on, **7:3, (**1999) 315-326.

116   Szarowski, D.H., Andersen, M.D., Retterer, S., Spence, A.J., Isaacson, M., Craighead, H.G., Turner, J.N., Shain, W., Brain responses to micro-machined silicon devices, Brain Research, **983:1–2, (**2003) 23-35.

117   Johnson, M., Otto, K., Kipke, D., Repeated Voltage Biasing Improves Unit Recordings by Reducing Resistive Tissue Impedances, IEEE Transactions on Neural Systems and Rehabilitation Engineering, **13:2,** (2005) 160-165.

118   Moffett, C., A defense from your Natural defenses, in: sensor-4 (Ed.), The University of Tennessee, Knoxville, 2011.

119   Grill, W., Thomas Mortimer, J., Electrical properties of implant encapsulation tissue, Annals of Biomedical Engineering, **22:1,** (1994) 23-33.

120   Xu, J., Shepherd, R.K., Millard, R.E., Clark, G.M., Chronic electrical stimulation of the auditory nerve at high stimulus rates: a physiological and histopathological study, Hearing Research, **105:1–2,** (1997) 1-29.

121   Williams, J.C., Hippensteel, J.A., Dilgen, J., Shain, W., Kipke, D.R., Complex impedance spectroscopy for monitoring tissue responses to inserted neural implants, Journal of Neual Engineering, **4:**(2007) 410. DOI:10.1088/1741-2560/4/4/007

122   Edell, D.J., Toi, V.V., McNeil, V.M., Clark, L.D., Factors influencing the biocompatibility of insertable silicon microshafts in cerebral cortex, Biomedical Engineering, IEEE Transactions on, **39:6,** (1992) 635-643.

123   Cui, X., Lee, V.A., Raphael, Y., Wiler, J.A., Hetke, J.F., Anderson, D.J., Martin, D.C., Surface modification of neural recording electrodes with conducting polymer/biomolecule blends, Journal of Biomedical Materials Research, **56:2,** (2001) 261-272.

124   Rousche, P., Normann, R., A method for pneumatically inserting an array of penetrating electrodes into cortical tissue, Annals of Biomedical Engineering, **20:4,** (1992) 413-422.

125   Otto, K.J., Johnson, M.D., Kipke, D.R., Voltage pulses change neural interface properties and improve unit recordings with chronically implanted microelectrodes, Biomedical Engineering, IEEE Transactions on, **53:2,** (2006) 333-340.

126   Weiland, J.D., Anderson, D.J., Chronic neural stimulation with thin-film, iridium oxide electrodes, Biomedical Engineering, IEEE Transactions on, **47:7,** (2000) 911-918.

127   Geim, A.K., Novoselov, K.S., The rise of graphene, Nat Mater, **6:3,** (2007) 183-191.

128   Zhou, M., Zhai, Y., Dong, S., Electrochemical sensing and biosensing platform based on chemically reduced graphene oxide, Analytical Chemistry, **81:14,** (2009) 5603-5613.

129   Liu, Y., Yu, D., Zeng, C., Miao, Z., Dai, L., biocompatible graphene oxide-Based glucose biosensors, Langmuir, **26:9,** (2010) 6158-6160.

130   Dong, X., Shi, Y., Huang, W., Chen, P., Li, L.-J., Electrical detection of DNA hybridization with single-base specificity using transistors based on CVD-grown graphene sheets, Advanced Materials, **22:14,** (2010) 1649-1653.

131   Shan, C., Yang, H., Song, J., Han, D., Ivaska, A., Niu, L., Direct electrochemistry of glucose oxidase and biosensing for glucose based on graphene, Analytical Chemistry, **81:6,** (2009) 2378-2382.

132   Geim, A., MacDonald, A., Graphene: exploring carbon flatland, Physics Today, **60:8,** (2007) 35-41.

133   Bell, W.J., Adiyodi, K.G., (1982). The american cockroach. London, New York. Chapman and Hall.

134   Roeder, K.D., Organization of the ascending giant fiber system in the cockroach (Periplaneta Americana), Journal of Experimental Zoology, **108:2,** (1948) 243-261.

135   Ritzmann, R.E., Pollack, A.J., Wind-activated thoracic interneurons of the cockroach: II. Patterns of connection from ventral giant interneurons, Journal of Neurobiology, **19:7, (**1988) 589-611.

136   Ritzmann, R.E., Pollack, A.J., Response of thoracic interneurons to tactile stimulation in the cockroach, Periplaneta americana, Journal of Neurobiology, **25:9, (**1994) 1113-1128.

137   J.E.Treherne, Buchan, P.B., Bennett, R.R., Sodium activity of insect blood: physiological significance and relevance to the design of physiological saline, Journal of Experimental Biology, **62:3, (**1975) 721-732.

138   Weidler, D.J., Sieck, G.C., A study of ion binding in the hemolymph of Periplaneta americana, Comparative Biochemistry and Physiology Part A: Physiology, **56:1, (**1977) 11-14.

139   Hyatt, A.D., Marshall, A.T., Sequestration of haemolymph sodium and potassium by fat body in the water-stressed cockroach Periplaneta americana, Journal of Insect Physiology, **23:11–12, (**1977) 1437-1441.

140   PICHON, Y., TREHERNE, J.E., Extraneuronal potentials and potassium depolarization in Cockroach giant Axons, Journal of Experimental Biology, **53:2, (**1970) 485-493.

141   Van Asperen, K., Van Esch, I., The chemical composition of the hemolymph in Periplaneta americana. With special reference to the mineral constituents, Arch. Neerl. Zool, **11:(**1956) 342-360.

142   Wendt, R.B., Weidler, D.J., Effect of external chloride replacement on action potentials of giant axons in Periplaneta americana, Comparative Biochemistry and Physiology Part A: Physiology, **44:4, (**1973) 1303-1311.

143   Gerischer, H.,Paul Delahay: Double Layer and Electrode Kinetics. Interscience Publishers, a Division of John Wiley & Sons, London-New York 1965. 321 Seiten. Preis: 110/- sh, Berichte der Bunsengesellschaft für physikalische Chemie, **70:7,** (1966) 765-766.

144   Bockris, J.O., Bonciocat, N., F.Gutmann, (1974). An introduction to electrochemical science. London, UK. Wykeham Publications Ltd.

145   Nation, J.L., (2001). Insect Physiology and Biochemistry. Gainesvill, Florida. CRC press.

146   Karazija, R., (1996). Introduction to the theory of x-ray and electronic spectra of free atoms. New York, USA. Springer.

147   Bach, F.-W., (2006). Front Matter. New York, USA. Wiley-VCH Verlag GmbH and Co. KGaA.

148   Sears, F.W., Zemansky, M.W., Young, H.D., (1983). University physics, 6th Ed. Boston, MA. Addision Wesley Publishing Company.

149   Windom, B., Sawyer, W., Hahn, D., A raman spectroscopic study of MoS2 and MoO3;: applications to tribological systems, Tribology Letters, **42:3,** (2011) 301-310.

150   Yin, H., Huang, R., Hobart, K.D., Suo, Z., Kuan, T.S., Inoki, C.K., Shieh, S.R., Duffy, T.S., Kub, F.J., Sturm, J.C., Strain relaxation of SiGe islands on compliant oxide, Journal of Applied Physics, **91:12,** (2002) 9716-9722.

151   Tan, P., Hu, C., Dong, J., Shen, W., Zhang, B., Polarization properties, high-order raman spectra, and frequency asymmetry between Stokes and anti-Stokes scattering of Raman modes in a graphite whisker, Physical Review B, **64:21,** (2001) 214301.

152   Malard, L.M., Pimenta, M.A., Dresselhaus, G., Dresselhaus, M.S., Raman spectroscopy in graphene, Physics Reports, **473:5–6,** (2009) 51-87.

153   Li, X., Cai, W., An, J., Kim, S., Nah, J., Yang, D., Piner, R., Velamakanni, A., Jung, I., Tutuc, E., Banerjee, S.K., Colombo, L., Ruoff, R.S., Large-area synthesis of high-quality and uniform graphene films on copper foils, Science, **324:5932,** (2009) 1312-1314.

154   Crist, B.v., (1999). Handbook of monochromatic XPS spectra, the elements & native Oides. Mountain view, CA. XPS International, LLC.

155   Weaver, J.F., Hoflund, G.B.,Surface Characterization Study of the Thermal Decomposition of AgO, The Journal of Physical Chemistry, **98:34,** (1994) 8519-8524.

156   Bielmann, M., Schwaller, P., Ruffieux, P., Gröning, O., Schlapbach, L., Gröning, P., AgO investigated by photoelectron spectroscopy: evidence for mixed valence, Physical Review B, **65:23,** (2002) 235431.

157   Wolan, J.T., Hoflund, G.B., Surface characterization study of AgF and AgF2 powders using XPS and ISS, Applied Surface Science, **125:3–4,** (1998) 251-258.

158   Gaarenstroom, S.W., Winograd, N., Initial and final state effects in the ESCA spectra of cadmium and silver oxides, Chemical Physics, **67:8,** (1977) 3500-3506.

159   Campbell, C.T., Paffett, M.T., The interactions of O2, CO and CO2 with Ag(110), Surface Science, **143:2–3,** (1984) 517-535.

160   Bigelow, R.W., An XPS study of air corona discharge-induced corrosion products at Cu, Ag and Au ground planes, Applied Surface Science, **32:1–2,** (1988) 122-140.

161   Huber, I., Masler, E.P., Rao, B.R., Cockroaches as models for neurobiology applications in biomedical research, in, vol. 2, CRC press, Inc, Boca Raton, Florida, 1990, pp. 298.

162   Rooij, A.d., The oxidation of silver by atomic Oxygen, ESA Journal, **13:363-382,** **(**1989).

163   Zheludkevich, M.L., Gusakov, A.G., Voropaev, A.G., Vecher, A.A., Kozyrski, E.N., Raspopov, S.A., Oxidation of silver by atomic oxygen, Oxidation of Metals, **61:1,** **(**2004) 39-48.

164   Gillespie, J.P., Kanost, M.R., Trenczek, T., Biological mediators of insect immunity, Annual review of entomology, **42:(**1997) 611-643.

165   Ryan, M., Nicholas, W.L., The reaction of the cockroach Periplaneta americana to the injection of foreign particulate material, Journal of Invertebrate Pathology, **19:3,** **(**1972) 299-307.

166   Pech, L.L., Strand, M.R., Plasmatocytes from the moth pseudoplusia includens induce apoptosis of granular cells, Journal of Insect Physiology, **46:12,** (2000) 1565-1573.

167   Tuinstra, F., Koenig, J.L., Raman spectrum of graphite, The Journal of Chemical Physics, **53:3,** (1970) 1126-1130.

168   R. Kostic, M. Miric, Radic, T., M.Radovic, Gajic, R., Popovic, Z.V., 2009, 31th Aug-3rd Sep, Optical characterization of graphene and highly oriented pyrolytic graphene, Proceedings of 2nd NanoCharm European School on Ellipsometry, Belgrade, Serbia

169   Ferrari, A.C., Meyer, J.C., Scardaci, V., Casiraghi, C., Lazzeri, M., Mauri, F., Piscanec, S., Jiang, D., Novoselov, K.S., Roth, S., Geim, A.K., Raman spectrum of graphene and graphene layers, Physical Review Letters, **97:18,** (2006) 187401.

170   Song, S., Xiao, P., An impedance spectroscopy study of high-temperature oxidation of thermal barrier coatings, Materials Science and Engineering: B, **97:1,** (2003) 46-53.

171   Gnedenkov, S.V., Sinebryukhov, S.L., Electrochemical impedance spectroscopy of oxide layers on the titanium surface, Russian Journal of Electrochemistry, **41:8,** (2005) 858-865.

172   Heung, R., Wang, X., Xiao, P., Characterisation of PSZ/Al2O3 composite coatings using electrochemical impedance spectroscopy, Electrochimica Acta, **51:8–9,** (2006) 1789-1796.

173   Gautier, C., Esnault, C., Cougnon, C., Pilard, J.-F., Casse, N., Chénais, B., Hybridization-induced interfacial changes detected by non-Faradaic impedimetric measurements compared to Faradaic approach, Journal of Electroanalytical Chemistry, **610:2,** (2007) 227-233.

174   Fuhrer, M.S., Physicists show electrons can tavel more than 100 times faster in graphene, in, University of Maryland, College Park, MD, USA, 2008.

175   Platzman, I., Brener, R., Haick, H., Tannenbaum, R., Oxidation of polycrystalline copper thin films at ambient conditions, The Journal of Physical Chemistry C, **112:4,** (2008) 1101-1108.

176   Helmholtz, H., Studien über electrische grenzschichten, Annalen der Physik, **243:7,** (1879) 337-382.

177   Warburg, E., Ueber das verhalten sogenanter unpolarsbarer elektroden gegen wechselstrons., Ann. Phys. Chim, **67:**(1899) 493-499.

178   Aurian-Blajeni, B., Beebe, X., Rauh, R.D., Rose, T.L., Impedance of hydrated iridium oxide electrodes, Electrochimica Acta, **34:6,** (1989) 795-802.

179   Young, K.F., Frederikse, H.P.R., Permittivity (Dielectric constant) of inorganic solids, Journal of Phys. Chem. Ref. Data, **2:**(1973) 313.

180   Mansfeld, F., Electrochemical impedance spectroscopy (EIS) as a new tool for investigating methods of corrosion protection, Electrochimica Acta, **35:10,** (1990) 1533-1544.

181   Loveday, D., Peterson, P., Rodgers, B., Evaluation of organic coating with electrochemical impedance spectroscopy. Part2: Application of EIS to coating, JCT Coatings Tech, **1:10,** (2004) 88-93.

182   Murray, J.N., Electrochemical test methods for evaluating organic coatings on metals: an update. Part II: single test parameter measurements, Progress in Organic Coatings, **31:3,** (1997) 255-264.

183   Randles, J.E.B., Kinetics of rapid electrode reactions, Discuss Faraday Soc., **1:**(1947) 11-19.

184   Epelboin, I., Keddam, M., Faradaic Impedances: diffusion impedance and reaction impedance, J. ELlectrochem. Soc, **117:**(1970) 1052-1056.

185   Chiu, C.-W., González, J.M., Harlow, M., Vinson, S.B., liang, H., Electrode–immune system interface monitor through neural stimulation in American cockroach (Periplaneta americana), Electrochimica Acta, **68:0,** (2012) 81-87.

186   Keefer, E.W., Botterman, B.R., Romero, M.I., Rossi, A.F., Gross, G.W., Carbon nanotube coating improves neuronal recordings, Nat Nano, **3:7,** (2008) 434-439.

187   Green, R.A., Lovell, N.H., Wallace, G.G., Poole-Warren, L.A., Conducting polymers for neural interfaces: challenges in developing an effective long-term implant, Biomaterials, **29:24–25,** (2008) 3393-3399.